Spatial Imaging of Strongly Interacting Rydberg Atoms

by

Nithiwadee Thaicharoen

A dissertation submitted in partial fulfillment
of the requirements for the degree of
Doctor of Philosophy
(Physics)
in the University of Michigan
2017

Doctoral Committee:

Professor Georg A. Raithel, Chair
Professor Steven T. Cundiff
Associate Professor Hui Deng
Professor Luming Duan
Professor Roseanne J. Sension

Nithiwadee Thaicharoen

nithi@umich.edu

ORCID iD: 0000-0003-1980-8213

ACKNOWLEDGEMENTS

I would like to express my sincere gratitude to my advisor, Professor Georg Raithel. Thank you for giving me an opportunity to learn from you. Your enthusiasm for research has been an inspiration for me. I hope that one day I will grow up to be like you! In addition, thank you for bringing me to the sailing club and teaching me how to sail and windsurf. To this day, that is one of my fondest memories. Although it is time for me to fly by myself, I will never forget that you taught me how to fly.

I would like to thank my dissertation committee members: Georg Raithel, Steven Cundiff, Hui Deng, Luming Duan, and Roseanne Sension, for your support and willingness to be on my committee.

I would like to acknowledge Raithel lab members and visitors: David Anderson, Sarah Anderson, Yun-Jhih Chen, Stephen DiIorio, Luís Felipe Gonçalves, Lu Ma, Jamie MacLennan, Stephanie Miller, Kaitlin Moore, Eric Paradis, Andira Ramos, Rachel Sapiro, Andrew Schwarzkopf, Mallory Traxler, Michael Viray, and Jianming Zhao. Thank you to everyone for making Ann Arbor feel like home. I am glad that I am surrounded by people who are good to me. I also appreciate Dave, Stephen, Stephanie, Rachel, Andy, and Michael for proofreading chapters in my thesis.

I would like to thank Andy for teaching me how to run the experiment, driving me back home when it was too late at night and no bus operated, and providing solutions to many experimental problems even after you are graduated. I really appreciate that I met and worked with you.

Many thanks to Stephanie for sharing ideas, for letting me help you eat your cookies, and for being a gym buddy. I would not be able to run a 5k without you! Thank you for your help that always comes to me whenever I need it.

Thank you to Kaitlin for sharing ideas, optical parts, and food. Your work ethic has inspired me to work harder in the lab. I am impressed by how you have a lot of interesting experimental ideas and how you organize your work.

I would like to thank Luís for being my labmate for 6 months. Obrigada (thanks) for sharing sandwiches, singing songs and doing push-ups in the lab together while waiting for a spectral scan, bringing me to the gym, and teaching me how to lift weights!

Many thanks to Dave for always sharing experimental ideas and suggestions. You are a very energetic person, which inspires me to work hard too. Your chocolate fudge and your mom's biscotti are delicious.

I would like to thank Yun-Jhih for giving advice both before I arrived in Ann Arbor and during my job applications. Thank you for getting me started working in the lab with Fortran and MOT coils and for recommending certain varieties of tea.

Thank you to Andira for singing songs together in the sub-basement and for making pineapple upside-down cake for my birthday. It was awesome!

Thank you to Jamie for feeding me chocolate and pastries and for sharing your blue laser.

Many thanks to Lu for several discussions about Rydberg-atom theory.

Thank you to Rachel, who did much of the TIP experiment design and construction.

I would like to thank Chris and Josh from NIST for giving me an opportunity to work on the EIT projects. The week I spent with you in January 2013 was incredibly

productive.

Thank you to former and current Physics department staff: Christina Zigulis, Paul Thurmond, Joseph Sheldon, Christine Betz Bolang, and Elise Bodei for your help throughout my graduate life.

Lastly, I would like to thank my parents for their love and support and for raising me to have a positive attitude, to be happy, and to never give up.

TABLE OF CONTENTS

LIST OF TABLES

Table

LIST OF FIGURES

Figure

ABSTRACT

The strong interactions between Rydberg excitations can result in spatial correlations between the excitations. The ability to control the interaction strength and the correlations between Rydberg atoms is applicable in future technological implementations of quantum computation. In this thesis, I investigates how both the character of the Rydberg-Rydberg interactions and the details of the excitation process affect the nature of the spatial correlations and the evolution of those correlations in time.

I first describes the experimental apparatus and methods used to perform high-magnification Rydberg-atom imaging, as well as three experiments in which these methods play an important role. The obtained Rydberg-atom positions reveal the correlations in the many-body Rydberg-atom system and their time dependence with sub-micron spatial resolution. In the first experiment, atoms are excited to a Rydberg state that experiences a repulsive van der Waals interaction. The Rydberg excitations are prepared with a well-defined initial separation, and the effect of van der Waals forces is observed by tracking the interatomic distance between the Rydberg atoms. The atom trajectories and thereby the interaction coefficient C_6 are extracted from the pair correlation functions of the Rydberg atom positions. In the second experiment, the Rydberg atoms are prepared in a highly dipolar state by using adiabatic state transformation. The atom-pair kinetics that follow from the strong dipole-dipole interactions are observed. The pair correlation results provide the first direct visualization of the electric-dipole interaction and clearly exhibit its anisotropic nature.

In both the first and the second experiment, results of semi-classical simulations of the atom-pair trajectories agree well with the experimental data. In the analysis, I use energy conservation and measurements of the initial positions and the terminal velocities of the atom pairs to extract the C_6 and C_3 interaction coefficients. The final experiment demonstrates the ability to enhance or suppress the degree of spatial correlation in a system of Rydberg excitations, using a rotary-echo excitation process in concert with particular excitation laser detunings. The work in this thesis demonstrates an ability to control long-range interactions between Rydberg atoms, which paves the way towards preparing and studying increasingly complex many-body systems.

CHAPTER I

Introduction

Dipolar and van der Waals interactions between atoms and molecules affect the properties of matter on microscopic and macroscopic scales. Highly excited Rydberg atoms present an ideal platform to study these interactions in pair and few-body quantum systems because Rydberg-atom interactions are generally strong and widely tunable between dipole-dipole, van der Waals and other types. The interaction between individual Rydberg atoms is important in the description and control of interactions in few- and many-body dynamics studies, which have been of considerable interest in recent years. On the quantum level, the distinctions between van der Waals and electric dipole-dipole interactions are in the overall interaction strength, the scaling with the internuclear separation (R^{-6} for the van der Waals and R^{-3} for the electric-dipole interactions), and the isotropic and the anisotropic behaviors. In several previous experiments, internal-state changes due to electric dipole-dipole [1–4] and van der Waals [5, 6] interactions between Rydberg atoms have been studied using spectroscopic measurements of level shifts.

An important consequence of strong interactions is that the energy of a Rydberg state is shifted out of resonance due to the presence of other Rydberg atoms nearby, causing neighboring atoms to be blocked from excitation. The excitation blockade

results in suppression of Rydberg detections [7–11], collective excitations [12, 13], and spatial correlations between Rydberg atoms [14–17]. Evidence for the excitation blockade has been obtained using atom counting statistics, including the Mandel Q-parameter, which is defined as

$$Q = \frac{\langle N^2 \rangle - \langle N \rangle^2}{\langle N \rangle} - 1 \quad , \tag{1.1}$$

where N is a number of detected Rydberg atoms. Values of $Q = 1$, <1, and >1 indicate Poissonian, sub-Poissonian, and super-Poissonian statistics of the Rydberg-atom system, respectively. While non-interacting atom samples follow Poissonian statistics, blockaded Rydberg-atom samples exhibit sub-Poissonian counting statistics [18–23].

The correlations between Rydberg atoms have been enhanced by detuning the excitation laser to match the van der Waals energy level shift [24, 25]. This enhancement leads to facilitated excitations at a well-defined pair separation [22, 26–30]. The counting statistics of this system have been studied using statistical moments up to third order [22] as well as bimodal distributions [21]. In contrast to the excitation blockade, ensembles of correlated Rydberg-atom pairs result in super-Poissonian counting statistics [31, 32]. Another method to control Rydberg-atom correlations is based on a rotary excitation echo [33–36], which occurs when the sign of the Rabi frequency is flipped in the middle of the excitation pulse.

The ability to control many-body interactions in Rydberg-atom systems allows for the study of quantum phase transitions of Rydberg atoms [37]. To understand the underlying mechanisms, several calculations have been performed to simulate the initialization of the Rydberg-atom sample using rate equations [30, 38], a hybrid model [39], a mean-field approximation [8], and the exact Hamiltonian [40]. The study of phase transitions by implementing an adiabatic frequency sweep has led to an observation of crystalline phases of Rydberg excitations [16, 41–44]. In addition,

number statistics of the Rydberg atoms [12, 30] and thermodynamic properties [45] have been used to explain the steady state of Rydberg-atom systems.

The exaggerated properties of Rydberg atoms are useful for a variety of applications. The strong, long-range interactions, as well as the collective properties of Rydberg atoms are beneficial for implementing quantum information processing, including quantum entanglement [46], quantum gate [7, 47–49], and quantum memory [50]. The correlations between Rydberg atoms have been used to realize non-classical light sources, such as single-photon as well as correlated-photon sources [51]. Furthermore, the large polarizabilities of Rydberg atoms make them good tools for electric-field sensing [52–55].

1.1 Spatial detection of Rydberg atoms

In addition to energy level shifts, interactions between Rydberg atoms can result in spatial correlation between excitations. When the excitation lasers are tuned to match a Rydberg transition frequency, atoms are expected to have a separation larger than the blockade radius, due to the blockade effect. In contrast, when the laser frequency is tuned to match an interaction-induced energy level shift, atoms are excited at a well-defined separation. Many experiments have been performed by having two atoms separated by a controlled distance using double optical dipole traps [4, 6, 47, 56, 57], to ensure that atoms are in certain desired excitation regions. Optical lattices are also utilized to provide spatial constraint to Rydberg-atom positions [50, 58–60].

However, not many experiments have high enough resolution to detect Rydberg-atom positions, which is important to study Rydberg-atom kinetics and internal dynamics resulting from interatomic interactions. Fluorescence imaging has been utilized to observe the spatial distribution of Rydberg excitations in two-dimensional

optical lattices [16, 43]. Spatially-resolved ionization using a focused scanning electron beam has also been used to detect Rydberg-atom correlations with high spatial resolution [61, 62]. Another area of somewhat related work is to perform direct Rydberg-wavefunction imaging. There, the objective is to map electronic Rydberg wavefunctions [63] (not center-of-mass Rydberg-atom positions).

In my group, a modified field ion microscope [64–66] is employed to measure the Rydberg atom positions. The experimental apparatus and methods achieve high-magnification Rydberg-atom imaging with sub-micron resolution. The center-of-mass positions of individual Rydberg atoms are detected and the spatial pair correlation functions [24] are extracted to study interactions between Rydberg atoms. The apparatus is less complicated than other high-resolution experiments; yet it is very powerful. It is the first apparatus that revealed blockade radii in Rydberg-atom systems [15] by a direct spatial imaging.

1.2 Thesis framework

The thesis starts with an introduction to Rydberg atoms and relevant backgrounds, including long-range interactions and collective excitations, in Chapter II. Next, the experimental setup for Rydberg excitation and detection is described in Chapter III. The image processing as well as pair-correlation calculations are also provided in this chapter.

Chapters IV-VI explain the experiments that have been performed on this setup. Specifically in Chapter IV, pairs of Rydberg atoms are prepared with a well-defined initial separation by detuning an excitation laser and utilizing the R^{-6} dependence of the van der Waals interaction. After preparation, the atoms are subject to repulsive van der Waals forces. The effect of the forces is observed by tracking the interatomic

distance between the Rydberg atoms, probing them after they have been allowed to move for selected wait times. The atom trajectories and thereby the van der Waals interaction coefficient C_6 are extracted from the pair correlation functions of the Rydberg atom positions. This experiment also shows that van-der-Waals-induced motion causes dephasing in coherently shared Rydberg excitations (superatoms) [67, 68].

Chapter V explains a study of anisotropic electric-dipole interactions between Rydberg atoms. Rydberg atoms are prepared with a well-defined initial separation in a weak-interaction regime to generate samples with high density. Then, the Rydberg atoms are adiabatically transferred to highly dipolar states by application of an electric-field ramp, where their dipole moments are fixed to the direction of the electric field. In this chapter, I provide the first direct visualization of the electric-dipole interaction, where the pair correlation functions exhibit anisotropic patterns that follows from the anisotropy of the electric-dipole force.

In Chapter VI, I study the correlation between Rydberg atoms when the excitation laser follows a rotary-echo sequence according to Reference [36]. I observe that this method can substantially enhance spatial correlations between the Rydberg excitations, and it strongly affects the counting statistics of Rydberg excitations in the samples. In addition, the rotary echo gives rise to strong spatial correlations when the excitation lasers are on-resonant, while in certain off-resonant cases the echo causes destruction of spatial correlations.

Finally, Chapter VII concludes this thesis and possible future experiments based on the imaging technique are described.

1.3 List of publications

The works explained in or closely related to this thesis are published in the following articles:

Control of spatial correlations between Rydberg excitations using rotary echo
N. Thaicharoen, A. Schwarzkopf, and G. Raithel
Phys. Rev. Lett. **118**, 133401 (2017)

Motion of Rydberg atoms with strong permanent-electric-dipole interactions
L.F. Gonçalves, N. Thaicharoen, G. Raithel
J. Phys. B: At. Mol. Opt. Phys. **49** 154005 (2016)

Atom-pair kinetics with strong electric-dipole interactions
N. Thaicharoen, L.F. Gonçalves, G. Raithel
Phys. Rev. Lett. **116**, 213002 (2016)

Measurement of van-der-Waals interaction by atom trajectory imaging
N. Thaicharoen, A. Schwarzkopf, and G. Raithel
Phys. Rev. A **92**, 040701 (Rapid Communication) (2015)
Editors' Suggestion

Spatial correlations between Rydberg atoms in an optical dipole trap
A. Schwarzkopf, D. A. Anderson, N. Thaicharoen, and G. Raithel
Phys. Rev. A **88**, 061406 (Rapid Communication) (2013)
Editors' Suggestion

In addition, I have also worked on Rydberg electromagnetically induced transparency (EIT) RF-electric field sensing. While this work is not directly related to this thesis, it has resulted in a number of peer-reviewed publications [54, 69–72].

CHAPTER II

Background Theory

2.1 Properties of Rydberg atoms

Rydberg atoms are atoms in highly excited states with large principal quantum number n. A valence electron orbital radius of a Rydberg atom is 100-100,000 larger than a ground state atom, leading to a large electric dipole moment and a strong polarizability. This makes Rydberg atoms very sensitive to external electric fields and can lead to strong interatomic interactions.

2.1.1 Quantum defect theory

Alkali Rydberg atoms have one valence Rydberg electron and a hydrogen-like structure. Instead of having a core that contains one proton as in hydrogen, the alkali atoms have inner-shell electrons orbiting around a larger ion core. If a Rydberg electron is in a low angular momentum state ($\ell \leqslant 2$), the Rydberg electron wavefunction overlaps with the core and the distribution of inner-shell electrons becomes significant. Due to core penetration, the Rydberg electron experiences a potential well that is deeper than $-1/r$ because of the decreased shielding of the nuclear charge. For Rydberg states with high orbital angular momentum ($\ell > 2$) , the overlap of Rydberg electron wavefunction with the core is small and the electron spends most of its time far from the core, leading to an interaction that mostly resembles the Coulomb

interaction from a proton core in hydrogen. However, the outer electron slightly polarizes the electron-ion core. This core polarization also affects the Rydberg electron energy [73, 74].

The core penetration has a stronger effect on the Rydberg energy than the core polarization, and both contribute to an increase of the Rydberg atom binding energy, given by [75]

$$W = \frac{-R_{\mathrm{y}}}{(n^*)^2} \quad . \tag{2.1}$$

Here, $R_{\mathrm{y}} = R_\infty/(1 + m_e/m_{\mathrm{atom}})$ is the Rydberg constant for a finite nuclear mass [81], where R_∞ is the Rydberg constant [82] and $n^* = n - \delta_{n,\ell}$ is the effective principal quantum number, where $\delta_{n,\ell}$ is the $n-$ and $\ell-$dependent quantum defect defined by the Ritz expansion [75, 83],

$$\delta_{n,\ell} = \delta_0 + \frac{\delta_2}{(n-\delta_0)^2} + \frac{\delta_4}{(n-\delta_0)^4} + ... \quad , \tag{2.2}$$

where the parameters $\delta_0, \delta_2, \delta_4, ...$ are empirically obtained from experiments and depend on the atomic species. The quantum defects for rubidium Rydberg atoms are provided in References [84, 85] for nS, nP, and nD states, as well as in Reference [86]

Table 2.1: Properties of Rydberg atoms and scaling with n^* [75–77].

Property	Scaling	Expression	References
Orbital radius, $\langle r \rangle$	$(n^*)^2$	$[3(n^*)^2 - \ell(\ell+1)]/2$	
Dipole moment matrix element, μ	$(n^*)^2$	$\langle n^{*\prime}\ell' = \ell \pm 1 \vert er \vert n^*\ell\rangle$	
Binding energy, E_{n*}	$(n^*)^{-2}$	$-R_{\mathrm{y}}/(n^*)^2$	
Energy level spacing, ΔE	$(n^*)^{-3}$	$E_{n*+1} - E_{n*}$	
Polarizability, α	$(n^*)^7$	$p/F \propto \mu^2/\Delta E$	
Radiative lifetime (0 K), $\tau_{n\ell}$	$(n^*)^{3 \text{ to } 5}$	$\tau_0(n^*)^{\alpha_\ell}$	[78]
BBR lifetime (300K), $\tau^{bb}_{n\ell}$	$(n^*)^2$	$\frac{3\hbar(n^*)^2}{4\alpha^3 k_B T}$	[79, 80]

Note: p is a dipole moment and F is an electric field strength.

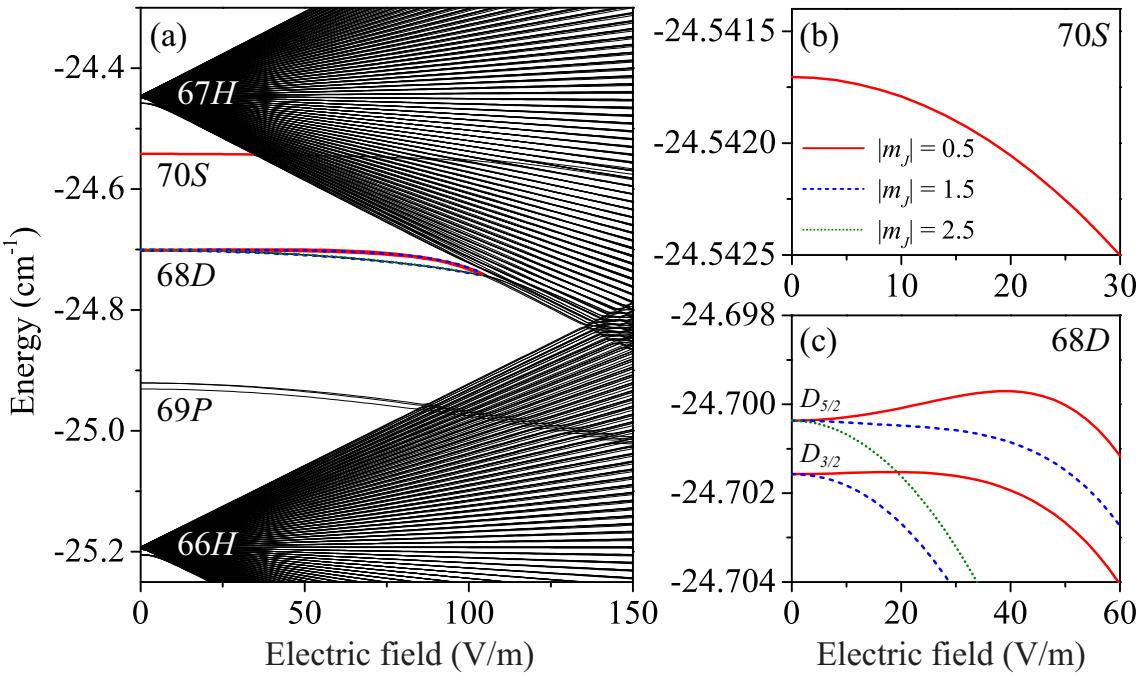

Figure 2.1: (a) Stark map of ^{85}Rb in the range between a 66H state and a 67H state. The thick colored lines for 70S and 68D states are shown in (b) and (c), respectively.

for nF states. Some general properties of Rydberg atoms and their scaling with n^* are shown in Table 2.1.

2.1.2 Rydberg atoms in electric fields

Rydberg atoms are sensitive to external electric fields due to their high polarizabilities. The presence of the electric field allows one to observe energy level shift of different states in Rydberg atoms in a similar way of the splitting in a hydrogen atom. Figure 2.1 shows a calculated Stark map for ^{85}Rb in the vicinity of 68D state. The energy shifts of Rydberg atoms due to the Stark effect have been calculated using diagonalization of the energy matrix [87]. Due to their large quantum defects, low-ℓ Rydberg states in rubidium ($\ell = 0, 1, 2$) are non-degenerate and separated from the hydrogenic manifold. At low electric field, the level energies quadratically shift as $(\alpha E^2)/2$, where α is the DC electric polarizability of the Rydberg state. For $\ell \geqslant 4$,

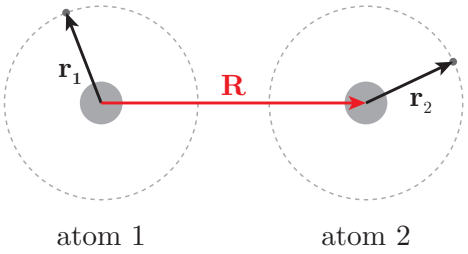

Figure 2.2: Two atoms whose center-of-mass positions are separated by **R**. The position vector of the the valence electron with respect to the ion core is represented by $\mathbf{r}_{1,2}$. The direction electric dipole $\mathbf{p}_{1,2}$ follows the direction of $\mathbf{r}_{1,2}$

the level energies shift linearly, largely resembling the hydrogen Stark spectrum.

Stark maps like the ones shown in Figure 2.1 are used to measure the electric field and calibrate voltages on electrodes that produce the electric field in the experiments. More details about electric-field measurement and calibration are discussed in Section 3.5.

2.2 Rydberg-Rydberg interactions

As seen in Section 2.1.2, Rydberg atoms are sensitive to externally-applied electric fields. This also applies when the electric field is generated by the charge distribution of other Rydberg atoms. This can lead to strong long range interactions between Rydberg atoms, compared to the relatively weak interaction between ground state atoms. For the interactions that are relevant to this thesis, the separation between atoms is much larger than the size of interacting Rydberg atoms (Le Roy radius) and the electron wave functions of the individual atoms do not overlap. The Le Roy radius, R_{LR}, is defined as [88]

$$R_{\mathrm{LR}} = 2\left(\langle r_1^2\rangle^{1/2} + \langle r_2^2\rangle^{1/2}\right) \quad , \tag{2.3}$$

where $\langle r_i^2\rangle$ is an expectation value of square of radius of the outermost electrons of atom i (atomic radius).

Consider a classical model that describes a Rydberg atom as an ion core with a

single valence electron orbiting around the core (see Figure 2.2). The Hamiltonian of two interacting Rydberg atoms with a separation between ion cores, $\mathbf{R}$, is

$$\hat{H}_{\mathrm{dd}} = \hat{H}_1 + \hat{H}_2 + \hat{V}(\mathbf{R}) - \hat{V}(\mathbf{R} - \mathbf{r}_1) - \hat{V}(\mathbf{R} - \mathbf{r}_2) + \hat{V}(\mathbf{R} - (\mathbf{r}_1 - \mathbf{r}_2)) \quad , \tag{2.4}$$

where $\hat{H}_{1,2}$ is the Hamiltonian of an isolated atom, $\mathbf{r}_{1,2}$ is the position vector of the the valence electron with respect to the ion core, and $\hat{V}(r) = 1/(4\pi\epsilon_0 r)$ is the Coulomb potential.

2.2.1 First- and second-order interactions

By applying a multipole expansion [89] to Equation 2.4 and assuming $|\mathbf{R}| \gg |\mathbf{r}|_{\mathbf{1,2}}$, the first relevant term is the dipole-dipole interaction given by

$$\hat{V}_{\mathrm{dd}} = \frac{e^2}{4\pi\epsilon_0} \frac{\mathbf{r}_1 \cdot \mathbf{r}_2 - 3(\hat{\mathbf{n}} \cdot \mathbf{r}_1)(\hat{\mathbf{n}} \cdot \mathbf{r}_2)}{|\mathbf{R}|^3} \tag{2.5}$$

where $\hat{\mathbf{n}}$ is a unit vector pointing along the internuclear coordinate $\mathbf{R}$.

The dipole-dipole interaction leads to an energy-level shift of the initial Rydberg state. One can calculate the energy shift caused by this interaction using perturbation theory, as explained in Reference [90]. Consider atoms in a Rydberg state $|A\rangle$. The presence of an external electric field induces a permanent electric dipole moment along the same direction as the field. The interaction between two Rydberg atoms that are in an initial two-body state, $|A\rangle \otimes |A\rangle$, is given to first-order by,

$$\Delta W^{(1)} = \langle A| \otimes \langle A|\hat{V}_{\mathrm{dd}}|A\rangle \otimes |A\rangle \quad . \tag{2.6}$$

A dipole dispersion coefficient is $C_3 = p_1 p_2/(4\pi\epsilon_0)$, where $p_{1,2}$ is the dipole moment of atom 1 and 2. The dipole-dipole interaction is expressed as C_3/R^3 and the interaction strength scales as $(n^*)^4/R^3$.

When there is no electric field, the first-order shift vanishes. The energy shift is then obtained in second-order,

$$\Delta W^{(2)} = -\sum_{B,C;\Delta\neq 0} \frac{|\langle C|\otimes\langle B|\hat{V}_{\rm dd}|A\rangle\otimes|A\rangle|^2}{\Delta} \quad , \tag{2.7}$$

where Δ is the energy difference between a virtual two-body state, $|B\rangle\otimes|C\rangle$, and the initial state, $|A\rangle\otimes|A\rangle$, and is sometimes called Förster defect [77]. A van der Waals dispersion coefficient is $C_6 = -(C_3)^2/\Delta$ and the sign of the van der Waals interaction is determined by the sign of Δ. The van der Waals interaction is then expressed as C_6/R^6 and scales as $(n^*)^{11}/R^6$.

For ground state atoms, the Förster defect is positive because all virtual states have higher energies. For rubidium, the van der Waals interactions are attractive for atoms in the ground state, repulsive for atoms in Rydberg S states, and mostly attractive for atoms in Rydberg P and D states [90].

2.2.2 Higher-order interactions

In order to obtain higher precision in the energy determination, ones need to include higher order interactions in the calculation. Letting the center-of-mass of two atoms be located along the z axis (so that the internuclear axis aligns along the z axis), the multipole expansion of the interaction terms in Equation 2.4 is given by (atomic unit) [91]

$$\hat{V} = \sum_{L_{1,2}=1}^{\infty} \sum_{M=-L_<}^{+L_<} \frac{(-1)^{L_2} f_{L_1 L_2 M}}{R^{L_1+L_2+1}} \hat{Q}_{L_1 M}(\mathbf{r}_1)\hat{Q}_{L_2 -M}(\mathbf{r}_2) \quad . \tag{2.8}$$

$\hat{Q}$ is a multipole operator for each atom, defined as

$$\hat{Q}_{LM}(\mathbf{r}) = \left(\frac{4\pi}{2L+1}\right)^{1/2} r^L Y_{LM}(\hat{\mathbf{r}}) \quad , \tag{2.9}$$

where r^L is a radial matrix element, Y_{LM} is a spherical harmonic, and L is a quantum number that characterize the type of interaction (e.g., $L = 1$ and 2 represents dipole

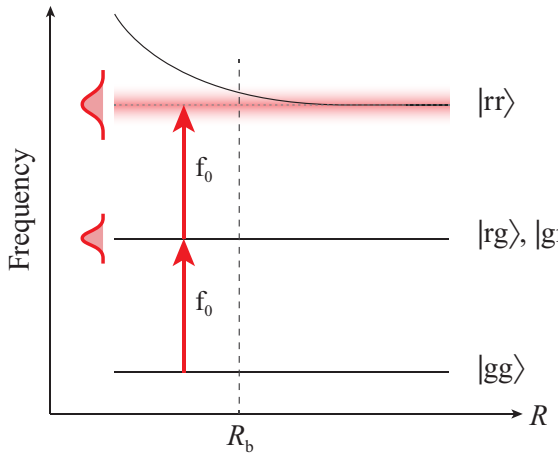

Figure 2.3: Energy level for two atoms as a function of interatomic separation, R. The frequency to excite one Rydberg atom without interactions is f_0. The energy shift due to Rydberg-Rydberg interactions blocks an excitation to the $|rr\rangle$ state at a separation $R < R_\mathrm{b}$.

and quadrupole interactions, respectively). f is a constant given by

$$f_{L_1 L_2 M} = \frac{(L_1 + L_2)!}{[(L_1 + M)!(L_1 - M)!(L_2 + M)!(L_2 - M)!]^{1/2}} \quad . \tag{2.10}$$

By using Equation 2.8, the interaction coefficient up to C_{10} has been calculated [92]. The observation of the direct excitation to molecular states originating from the dipole-quadrupole interaction has been reported in Reference [93].

2.2.3 Rydberg blockade

The dipole-dipole or van der Waals interaction cause the energy of a Rydberg state to be shifted out of resonance with respect to the excitation laser by a neighboring Rydberg atom, as seen in Figure 2.3. If the energy shift is larger than the excitation bandwidth, the excitation to the Rydberg state of this second atom is "blocked". This is called excitation blockade or dipole blockade and has been observed in several experiments [1, 8–10, 12, 18, 94–96].

The distance where the excitation bandwidth equals to the van der Waals energy shift is defined as the blockade radius R_b which is

$$R_\mathrm{b} = \left(\frac{C_6}{\hbar \delta_{\nu \mathrm{L}}} \right)^{1/6} \quad , \tag{2.11}$$

where $\delta_{\nu \mathrm{L}}$ is a laser linewidth, which dominates the excitation bandwidth in the experiments described in this thesis.

2.2.4 Excitation enhancement and long-range correlations

According to Figure 2.3, atom pairs with a specific interatomic separation can be excited if the excitation laser frequency is tuned to the appropriate frequency or if the energy levels of the Rydberg atoms are modified (e.g., by AC Stark shift due to far off-resonant light field [15]) to match the energy shift due to the interaction. The method of tuning the excitation laser frequency is used to initialize Rydberg atoms throughout this thesis. Using this method, one can selectively excite atoms that are subject to specific van der Waals interaction, which relates to the separations between atoms. The spatial correlation between atoms that are located at this well-defined separation is enhanced through this pair excitation.

In addition to the pair-correlation enhancement, long-range correlations can build up due to off-resonant excitation, leading to Rydberg aggregate formation [22, 27, 29].

2.3 Collective excitation

In a fully blockaded system that contains a sample of N atoms located inside a blockade radius, only one atom is excited to a Rydberg state while all other atoms remain in the ground state. The combination of a single Rydberg atom and ground state atoms is sometimes called "superatom". The state used to explain the system is fully symmetric, where the excitation is coherently shared between all atoms,

$$|W\rangle = \frac{1}{\sqrt{N}} \sum_{i=1}^{N} |g_1, g_2, g_3, ..., r_i, ..., g_N\rangle \quad . \tag{2.12}$$

The collective Rabi frequency is obtained from

$$\begin{aligned}\Omega_{\text{collective}} &= \langle g_1, g_2, g_3, ..., g_N|\hat{H}|W\rangle \\ &= \langle g_1, g_2, g_3, ..., g_N|\hat{H}\frac{1}{\sqrt{N}}\sum_{i=1}^{N}|g_1, g_2, g_3, ..., r_i, ..., g_N\rangle \\ &= \sqrt{N}\Omega_{\text{single}}\end{aligned} \tag{2.13}$$

The decoherence of Rydberg atoms can come from decay, interaction between Rydberg atoms, and atomic motion during excitation. It has been predicted in Reference [67] that the dipole-dipole interaction is acting on individual atoms, not superatoms. This behavior is observed and explained in Chapters IV and V.

CHAPTER III

Experimental Setup

In this chapter, I present experimental details including Rydberg-atom preparation and detection, magnification calibration, and electric field control. Using a typical set of experimental ion images, I describe the image processing and pair correlation analysis.

3.1 Experimental setup

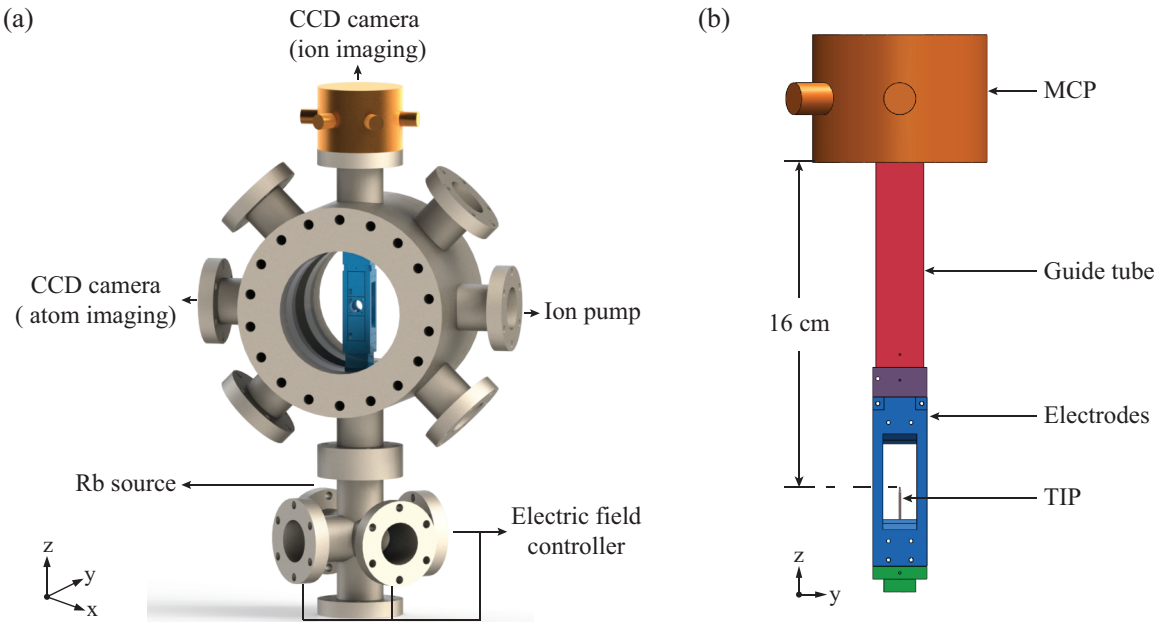

Figure 3.1: Experimental setup. (a) Experimental chamber. (b) Electrode package inside the chamber and ion detection assembly.

The experimental setup is illustrated in Figure 3.1(a). The experimental chamber maintains a pressure of 1.1×10^{-8} Torr with the use of an ion pump. The rubidium source is a small reservoir containing a rubidium ampoule. I control the amount of rubidium vapor by adjusting an input voltage to heat tape that wraps around the reservoir and leave the voltage on while the experiment is running. I use two CCD cameras for atom imaging and ion imaging.

The electrode package and ion detection assembly inside the chamber are illustrated in Figure 3.1(b). I apply DC voltages to electrode plates and a beryllium-copper needle (Signatone SE-BCB) to control the electric field in three orthogonal directions. The electrode package and the needle connect to external electric field controllers through two 9-pin D-type feedthroughs and a MHV feedthrough. The needle is also called tip imaging probe (TIP) because it plays the role of an ionization electrode. This configuration is similar to a field-ion microscope in which a radially divergent electric field is produced when the TIP is switched to a high voltage. Ions travel along the divergent field lines and produce magnified ion images. The guide tube is grounded and used to extend a time it takes for ions (time of flight) to travel to the microchannel-plate assembly (MCP) to obtain high magnification.

3.2 Experimental timing sequence

Atoms are prepared in a magneto-optical trap (MOT) before excitation into a Rydberg state and subsequent detection. In general, the experimental cycle is 20 Hz for shadow imaging and 60 Hz for fluorescence and Rydberg atom imaging (the frequency is limited by the speed of the cameras). The experimental timing used in different experiments is described in the corresponding chapters.

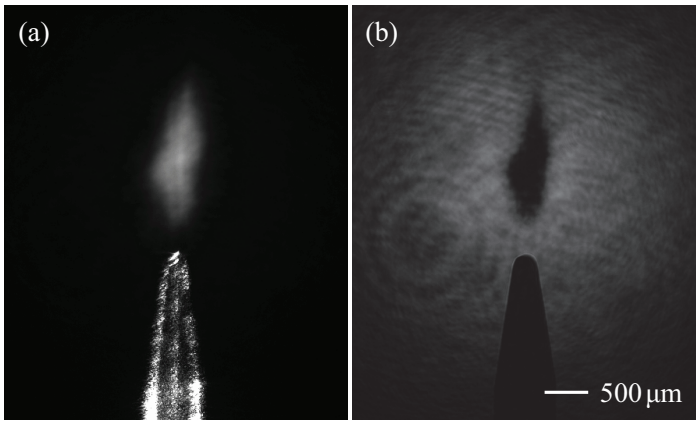

Figure 3.2: (a) Fluorescence and (b) shadow images of the MOT above the TIP.

3.2.1 Magneto-optical trap

^{85}Rb atoms in the $5S_{1/2}$ state are trapped and cooled to ~ 100 μK in a magneto-optical trap (MOT) [97, 98] at a density of $\gtrsim 10^{10}$ cm^{-3} for 17 ms. The MOT is located at $100-500$ μm above the TIP. The MOT laser ($5S_{1/2}, F=3 \rightarrow 5P_{3/2}, F'=4$) has a power of 60 mW and the repumper laser ($5S_{1/2}, F=2 \rightarrow 5P_{3/2}, F'=3$) has a power of 5-10 mW before they are split into 6 beams with a full width at half maximum (FWHM) of the beam diameter $\approx$ 1 cm. I use a PixelFly CCD camera to image the MOT. Fluorescence and shadow images of the MOT are shown in Figure 3.2(a) and (b), respectively. The MOT and repumper lasers are turned off for 80 μs during Rydberg excitation and detection.

3.2.2 Rydberg excitation

The preparation and detection of Rydberg atoms are illustrated in Figure 3.3(a). To excite the atoms to a Rydberg state, I perform a two-photon Rydberg excitation by simultaneously applying 780- and 480-nm laser pulses with 5 μs duration. The 780-nm laser is locked on the left side of the ^{87}Rb ($5S_{1/2}, F=2 \rightarrow 5P_{3/2},\ F'=2$ and $F'=3$ crossover) line, which provides $\approx$1 GHz red-detuned from the $5P_{3/2}, F'=4$ intermediate state. The 780-nm beam propagates along the x-direction and has a

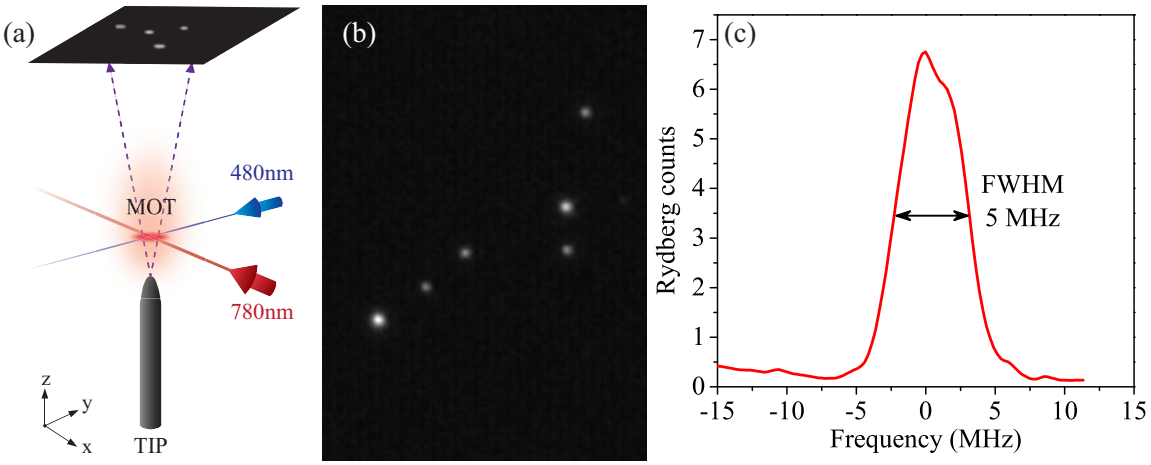

Figure 3.3: Preparation and detection of Rydberg atoms. (a) Excitation beams alignment. (b) Ion image. (c) Rydberg spectrum of the $70S_{1/2}$ state, averaged over 100 datasets.

Gaussian beam parameter of $w_0 \approx 70$ μm. The 480-nm beam propagates in the xy plane, forming an angle of approximately 70° with the 780 nm beam, and has $w_0 \approx 8$ μm.

3.2.3 Rydberg detection

3.2.3.1 Ion imaging

After excitation, Rydberg atoms are ionized by the application of 1,600 V to the TIP. Ions are accelerated by the TIP's electric field towards the MCP within 2-6 μs. Every detected ion results in a blip produced by the MCP-phosphor detector assembly. I capture the ion images [Fig. 3.3(b)] using a CCD camera (CV-M50IR from JAI) with an exposure time of 1 ms, together with a frame grabber (PCI-1409 from National Instruments).

The MCP (Beam Imaging Solutions BOS-18 with P-47 phosphor screen) has a Chevron configuration which yields a gain of about 10^6. The required detection kinetic energy is $\gtrsim 500$ eV for an ion and ~ 50 eV for an electron. The MCP power supply is home-built using parts from Ultravolt. The supply voltages to the MCP for different experimental purposes are shown in Table 3.1.

A combination of the TIP voltage and the MCP front voltage have to be carefully selected because the ion impact energy have to be $\gtrsim$ 500 eV. At the same time, the ion image magnification and the field of view need to satisfy the experimental requirement. High voltage applied to the phosphor screen is important for obtaining high visibility images. This value is also utilized for Rydberg spectroscopy with a Rydberg signal less than 20 counts/shot. For Rydberg spectroscopy with a higher number of counts, the applied voltage must be decreased in order to avoid saturating the phosphor screen.

For instance, if the ionization voltage is small (e.g., using a high-voltage amplifier which provides up to 400 V for state-selective field ionization), then I need to increase the magnitude of the front plate voltage to approximately -500 V to provide a sufficient impact energy of the ions. This, in turn, will reduce the spatial resolution due to the ion-lensing effect (the ion beam is refocused before detection). Conversely, if a high TIP voltage is employed (1,600 V), the ions already acquire a kinetic energy > 600 eV in the immediate vicinity of the TIP. In that case, I use a MCP front voltage of only -200 V, allowing for much larger magnification (but a reduced field of view). It is noted that the MCP back voltage and the phosphor screen voltage are always referenced relative to the MCP front voltage.

The initial design phase of the experiment is has to be decided whether ions or

Table 3.1: High-voltage supply to the MCP assembly

MCP part	Imaging	Spectroscopy (high count rate)	Power supply from Ultravolt
Front plate	-200 V	-200 V	-2kV: 2A12-N4-F-E
Middle plate	-	-	-
Back plate	1,500 V	1,500 V	2kV: 2A12-P4-F-E
Phosphor screen	4,950 V	3,650 V	6kV: 6A12-P4-F-E

Note: The middle plate has no electrical connection.

electrons are to be detected. The reason to detect ions instead of electrons is because ions represent the center-of-mass of position of atoms. Due to spatial extend of the Rydberg-electron wavefunction, electron detection would incur an additional position spread due to the wavefunction size, which exceeds the spatial resolution of the apparatus in some of the described experiment. Finally, it must be suspected that electron detections would result in a prohibitive number of photoelectrons from the surface of the TIP. Electron detections are generally used in experiments that have a short time of flight from the excitation region to the detection assembly and do not require knowing the spatial position of the impacted electrons (for example, Rydberg spectroscopy). However, the electron imaging is useful to probe Rydberg-atom wavefunctions.

I take 10,000 images in each data set. Using a peak-detection algorithm [24], the images are processed into a data structure in which each record contains the total number of detected ions and the ion impact positions in an individual image. The 5,000 records with the highest ion numbers are processed into a sample-averaged pair correlation image.

3.2.3.2 Atom counting

In addition to ion imaging, I also count number of Rydberg atoms in each experimental cycle. Every time an ion hits the MCP and produces a blip on the phosphor screen, it also sends a negative pulse to the phosphor screen connector (same connector that I use to provide the high voltage supply to the phosphor screen). I use a homemade high-pass filter to extract this pulse and send it to a fast preamplifier (Ortec VT120A) to amplify the ion signal. The signal is then sent to a two-channel gated photon counter (Stanford Research Systems SR400). If the signal strength is higher than the discriminator level (set to -0.100 V to prevent counting unwanted

signals that come from impedance mismatch and reflections in the transmission line), it will be considered as one Rydberg count. I start counting atoms 2 μs after the application of the field ionization pulse, with a gate time of 20 μs. An example of a Rydberg spectrum of ^{85}Rb $70S_{1/2}$ state obtained from averaging 100 datasets of the number of Rydberg atoms as a function of the frequency of the 480-nm laser is shown in Figure 3.3(c). The FWHM of the spectrum is 5 MHz, which is narrow for a state with high principal quantum number $n = 70$, indicating the ability to control the electric field in the excitation region (see Section 3.5). The width of the spectrum comes from residual laser linewidth effects (1-2 MHz) as well as van der Waals interactions between Rydberg atoms. The peak position indicates the on-resonant excitation $5S_{1/5} \rightarrow 70S_{1/2}$. The shoulder to the right of the spectrum reveals excitations where the laser detunings match repulsive van der Waals interactions (see Section 2.2).

3.3 Ionization electric field from the TIP

The TIP has a round top with a diameter of 125 μm. Once I apply a voltage to the TIP, it generates a radially divergent electric field. Ionization using the TIP leads to magnified ion images of the center-of-mass positions of the parent Rydberg atoms at the time of ionization. A simulation of the voltage and the electric field magnitude near the TIP surface when the TIP is set to 1,000 V [99] is shown in Figure 3.4.

The vertical position of the excitation region above the TIP affects the magnification of ion images. When the excitation region is closer to the TIP surface, ion trajectories becomes more divergent, resulting in higher magnification. However, it is difficult to have cold atoms closer than 100 μm to the TIP surface, as seen in Figure 3.2. The scattered light from the TIP surface prevents atoms from being trapped in the MOT very close to the TIP. It is possible to observe shadow images of a thin

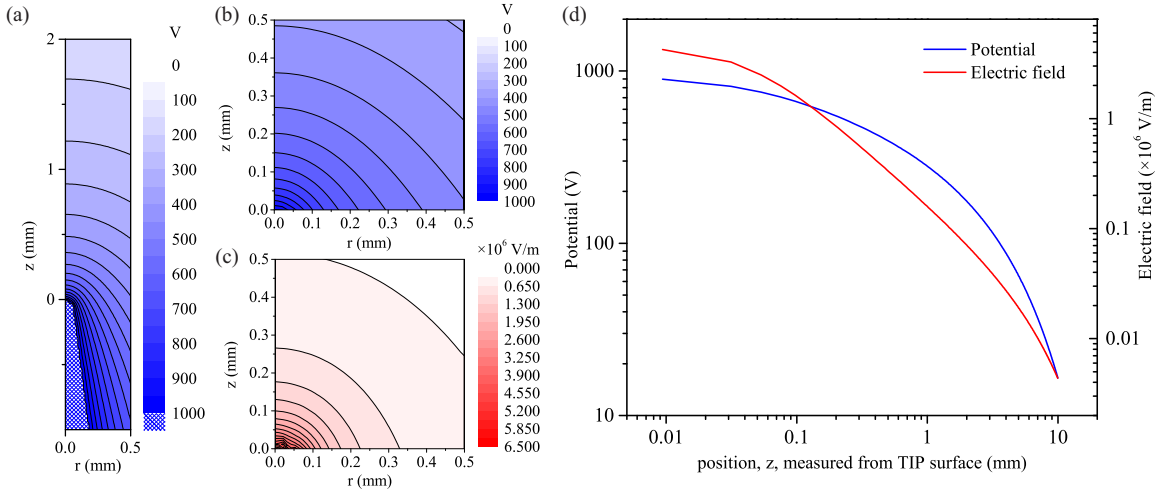

Figure 3.4: Simulation of (a,b) the potential and (c) the electric field magnitude near the TIP surface with 1000 V applied to the TIP. (d) Plot of the potential and the electric field magnitude near the TIP surface. The TIP surface is at z= 0 in these plots. Modified with permission from [99].

shell of atoms with a crescent shape locate at $\sim$ 50 μm above the TIP surface when a high voltage is applied to the TIP. The crescent reflects the Stark shift of the MOT transition close to the TIP, where the electric field is strong. In general, the trapping region is about 100-500 μm above the TIP, where the plots in Figures 3.4 and 3.6 can be used.

The electric field and voltage values at the excitation regions for the experiments in the following chapters are shown in Table 3.2. Note that the ionization electric field for a Rydberg atom with $n = 30$ is 616 V/cm and with $n = 100$ is 4 V/cm, where n is the principal quantum number. That means the application of this high voltage ionizes all Rydberg atoms in the excitation region.

3.4 Magnification calibration

I select the magnification of the ion images by considering the separation between atom pairs and make it match the field of view of the MCP. If the magnification is too high, the separation between atoms may be bigger than the field of view,

Table 3.2: Potentials and electric fields at different excitation positions above the TIP.

Position above TIP	Potential	Electric field	Magnification	Values used in
Simulation (1000 V at the TIP surface)				
473 μm	403 V	3,549 V/cm		
330 μm	464 V	5,153 V/cm		
Experiment (1,600 V at the TIP surface, scaled from simulation values)				
473 μm	645 V	5,679 V/cm	155	Chapter IV, VI
330 μm	742 V	8,245 V/cm	204	Chapter V

or the number of atoms in an image may be too small for further analysis. If the magnification is too low, the image resolution will be too low and atom positions inside the Rydberg blockade radius are indistinguishable.

The magnification of the image is determined by the position of the 480-nm beam above the TIP. To align this beam, I overlap it with an optical dipole trap (ODT) created by focusing a 1064-nm laser down to $w_0 = 23$ μm. I first align the ODT beam to be centered at the TIP point (this can be observed as a straight vertical scattering at the back of the TIP, which indicates that the beam hits the top surface of the TIP). During this process, I turn the power of the laser down to 200 mW to avoid damaging the TIP. Next, I move the beam up vertically and turn the ODT laser power to 4 W. The position of the ODT can be observed using a shadow image shown in Figure 3.5(a) (the shadow imaging camera has a calibration factor of 8.93 μm/pixel). Note that in order to observe the shadow image of the ODT I need to detune the 780-nm laser to match the frequency shift of the ODT potential (about 30-40 MHz). I use the same method to bring the 480-nm beam to the surface of the TIP. (I adjust the beam power to about 5-10 mW to avoid saturating the MCP with counts.) At the touch position, ions that are scattered out of the TIP provide uniform blips all over the MCP. When I move the 480-nm beam up to spatially overlap with the ODT beam, a region of substantially enhanced count rate appears on the MCP.

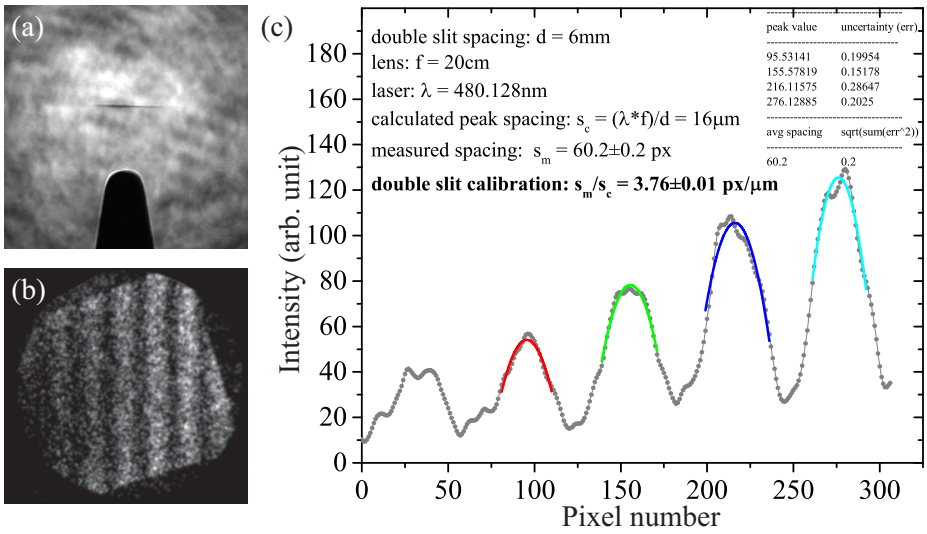

Figure 3.5: Magnification calibration method. (a) Shadow images of the ODT located at 473 μm above the TIP. (b) Interference pattern of the excitation beam obtained from summing ion images. (c) Histogram of (b). Local parabolic fits are used to detect the maxima of the pattern.

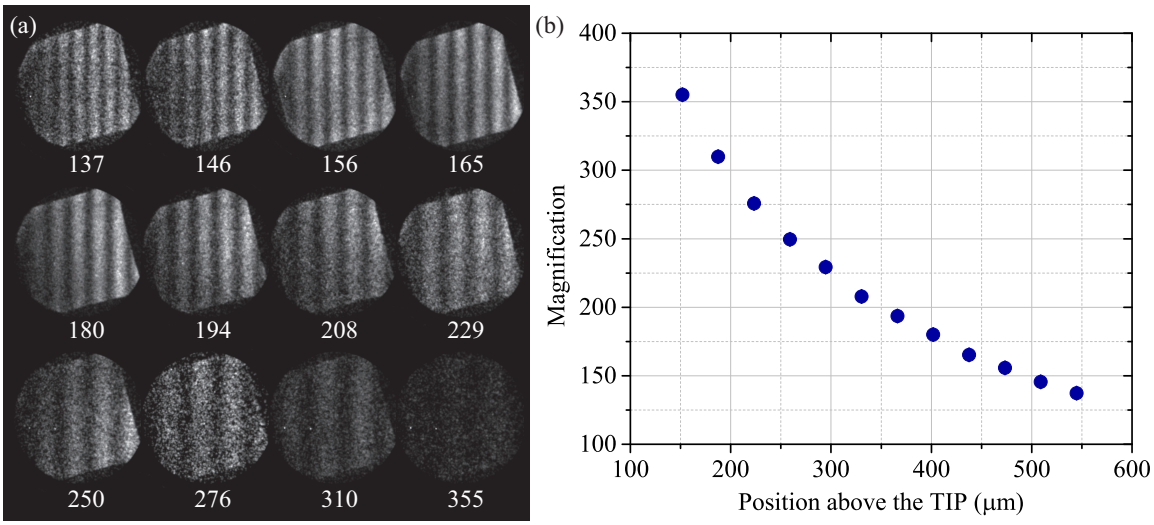

Figure 3.6: Interference patterns and magnification calibration results when the excitation beam is located at different positions above the TIP. (a) Ion images present interference patterns of the excitation beam at different magnification values. (b) Excitation beam positions corresponding to the magnification values in (a).

To obtain the magnification factor of the system, I put a double slit in the 480 nm beam path before focusing it down into the chamber. The separation between interference fringe maxima Δy is

$$\Delta y \approx \frac{\lambda D}{d}, \tag{3.1}$$

where λ is a wavelength of the laser, D is the focal length of the 480-nm beam focusing lens, and d is the center-to-center separation between the slits. With the ^{85}Rb $68D_{5/2}$ state and the slit used, $\lambda = 480.128$ nm, $D = 20$ cm, and $d = 6$ mm, I obtain $\Delta y = 16$ μm. The role of the lens is to bring the interference fringes which are initially located at infinity into the focal plane of the lens.

The interference pattern of the excitation beam is projected onto the excitation region and atoms are then excited to the Rydberg state following this pattern. I take 1,000-10,000 ion images and sum them in order to see this pattern [Figure 3.5(b)] and then plot the intensity as a function of position. I use local parabolic fits shown in Figure 3.5(c) to extract the peak positions and consequently the separation between adjacent maxima. From the example in Figure 3.5, the average separation between adjacent maxima is about 60 pixels, which corresponds to $\Delta y = 16$ μm. The magnification calibration factor becomes 3.7 pixels/μm (distance measured in object plane). The CCD camera for ion imaging has a calibration factor of 40.5 μm/pixel (distance measured in image plane) so the magnification of the ion images is $3.7 \times 40.5 = 150$ with an uncertainty of 2%. Note that the uncertainty also depends on the visibility of the interference pattern.

The magnification for different positions of the excitation volume above the TIP is shown in Figure 3.6. Over the experimentally accessible parameter, the largest magnification is ≈ 350.

3.5 Electric field control

To avoid having atomic energy level shifts due to Stark effect, the electric field at the excitation region is tuned to zero (with $\leqslant 20$ mV/cm uncertainties). I control the electric field in each axis by applying voltages to the corresponding electrodes,

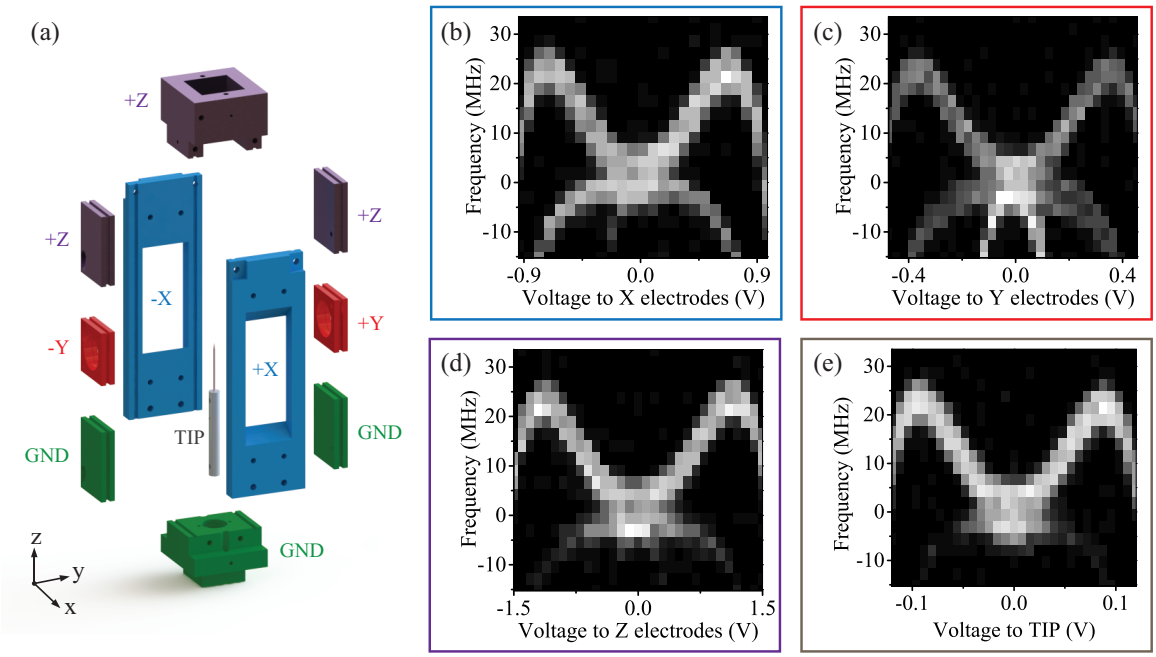

Figure 3.7: Electrode package and Stark map of the 68D state. (a) Blow up diagram of the electrode package. (b-e) Stark maps correspond to scanning applied voltages to X, Y, Z, and TIP electrodes.

as shown in Figure 3.7(a). I use Stark spectra of $nD_{5/2}$ states at high n to determine the field zero parameters; the zero position is where the states with different total angular momentum quantum numbers are degenerate. The Stark spectra of the $68D_{5/2}$ obtained by scanning the voltage of the electrodes along x, y, z axes and the TIP are presented in Figure 3.7(b-e).

The DC voltages used for controlling the electrode package are generated using a USB-3114 digital to analog converter from Measurement Computing. Low-pass filters are employed to eliminate voltage spikes or high frequency noise that might couple into the electrodes. For the TIP, which also serves as an ionization electrode, I connect the high-voltage source (SRS PS325) to a pulse generator (DEI PVX-4140). The high-voltage part (for ionization) is then combined to the low-voltage part (for electric field control) using a clamp switch. The clamp switch allows application of a high-voltage pulse to an electrode while maintaining a low noise during the off-time of the pulse.

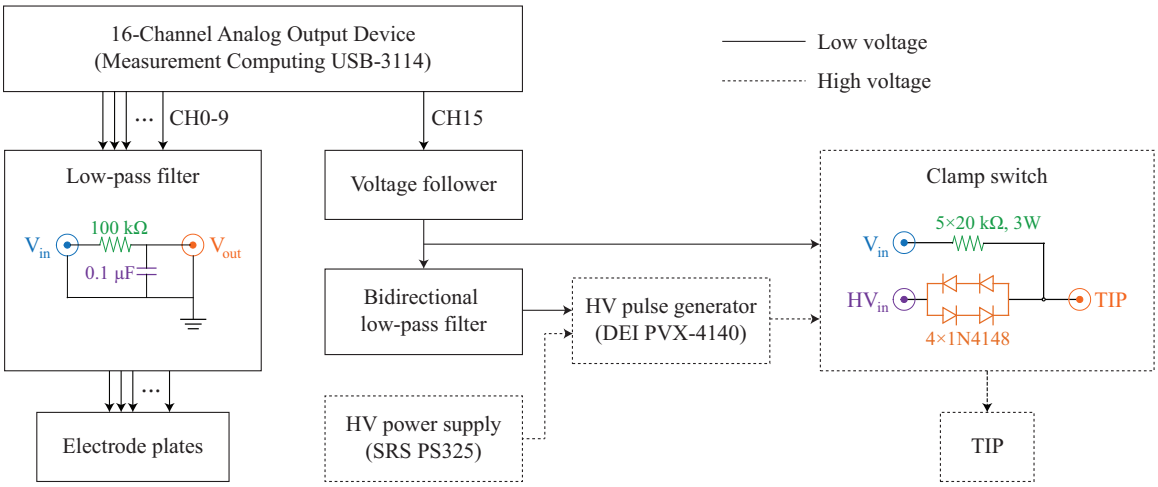

Figure 3.8: Diagram of voltage sources and filters used to control the electric field inside the chamber.

The schematic of the voltage source is shown in Figure 3.8.

3.6 Spatial pair correlation calculation

The pair correlation function has been used to study the spatial correlation between atoms. This method works under the condition that the magnification is high enough so that the interatomic separation can be resolved. During the excitation pulse, Rydberg atoms tend to be excited at a position where the excitation laser detuning matches the energy shift from interatomic interactions, which eventually shows up in the pair correlation image. Depending on the nature of the underlying interactions, the initial correlations in the atom sample can be either isotropic (for instance, van der Waals interaction between S-type Rydberg atoms) or anisotropic (for instance, permanent dipole-dipole interactions).

In the analysis, I apply a background noise elimination and a peak-detection algorithm [99] to extract the position of atoms from the image. Then, I calculate a normalized pair correlation image and an angular integral of the pair correlation function.

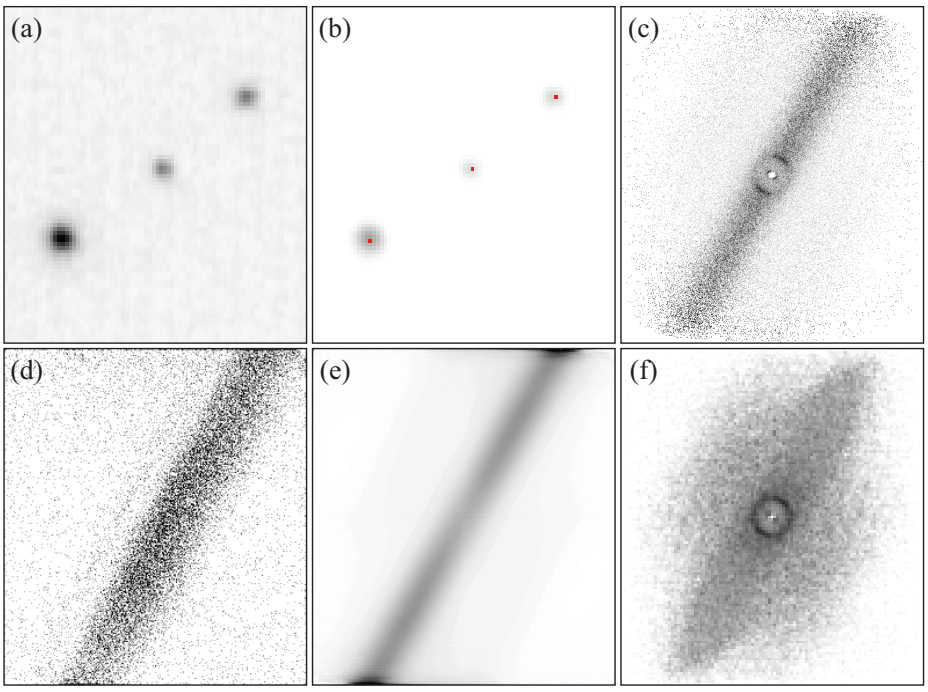

Figure 3.9: Procedures to obtain a normalized pair correlation image for the $70S_{1/2}$ state excited using laser detuning of +4 MHz. (a) An original image obtained from the experiment. (b) Preprocessed image. The red dots indicate the position of ions obtained from the peak detection algorithm. (c) Sum of pair correlation function. (d) Spatial distribution of atoms summed over 5000 ion images. (e) Pair correlation image of (d). (f) Normalized pair correlation image with the coarse-graining operation. The linear grayscale ranges from 0 (white) to 2 (black), where values of 1, < 1, and > 1 indicate no correlation, anticorrelation, and positive correlation, respectively.

An original image obtained from the CCD camera is shown in Figure 3.9(a). I perform image preprocessing with background removal to increase the visibility of the blips and the average filter to remove the intensity spikes that might cause multiple counting of atoms. In the peak detection algorithm, I determine an ion position by using the centroid of the blip in binary images of the preprocessed images. The resulting peak positions on top of the preprocessed image are shown in Figure 3.9(b). I typically extract the number of blips for 10,000 images and calculate the pair correlation of the 5,000 images with the highest number of blips.

The pair correlation image is calculated as follows

1) Sum of pair correlation

A pair correlation image is a two-dimensional histogram of the separation vector

$\vec{R}^{\alpha}_{\mathrm{i,j}} = (\vec{X}^{\alpha}_{\mathrm{i}} - \vec{X}^{\alpha}_{\mathrm{j}})$ between any two atoms i and j located at $\vec{X}^{\alpha}_{\mathrm{i}} = (x_{\mathrm{i}}, y_{\mathrm{i}})^{\alpha}$ and $\vec{X}^{\alpha}_{\mathrm{j}} = (x_{\mathrm{j}}, y_{\mathrm{j}})^{\alpha}$ in the same image α. For the image size $N \times M$, the pair correlation image has a size of $(2N-1)\times(2M-1)$. The pair correlation value at a pixel coordinate (n, m) in the pair correlation image is the number of occurrences that $\vec{R}_{i,j}$ resides within the pixel (n, m),

$$A^{\alpha}_{\mathrm{n,m}} = f(n, m, N, M) \sum_{\mathrm{i}\neq\mathrm{j}} \delta^{(2)}(\vec{R}^{\alpha}_{\mathrm{i,j}} - (n, m)) \quad , \tag{3.2}$$

where the spatial normalizing factor,

$$f(n, m, N, M) = \frac{NM}{(N - |n|)(M - |m|)} \quad , \tag{3.3}$$

is used in order to avoid finite-array effects; pixels located further from the center of the pair correlation image have a small overlapping factor in the correlation calculation. The individual pair correlation images are added to construct an average pair correlation image, A', shown in Figure 3.9(c). The A' is calculated from

$$A'_{\mathrm{n,m}} = \sum_{\alpha} A^{\alpha}_{\mathrm{n,m}} \tag{3.4}$$

2) Background elimination and coarse-graining operation

The sum of pair correlations, $A'_{n,m}$, has a general footprint given by the 480-nm beam shape in the excitation volume. It is desirable to normalize the pair correlation image such that any long-range dependence on position is eliminated, so that uncorrelated atoms produce a long-range pair correlation value of one. This normalization will help increase the visibility of the enhanced pair correlation. I start to calculate the background by combining atom positions (index k) for all images (index α). The value at pixel coordinate (i, j) in the summed image is

$$B_{\mathrm{i,j}} = \sum_{\alpha} \sum_{k} \delta^{(2)}(\vec{X}^{\alpha}_{\mathrm{k}} - (i, j)) \quad . \tag{3.5}$$

with an atom counter k. The resulting spatial distribution of atoms over 5,000 ion images is shown in Figure 3.9(d). Then, I calculate the pair correlation image of this sum shown in Figure 3.9(e),

$$B'_{\mathrm{n,m}} = f(n, m, N, M) \sum_{\mathrm{i,j}} B_{\mathrm{i,j}}\, B_{\mathrm{i-n,j-m}} \quad . \tag{3.6}$$

The spatial normalizing factor in Eq. 3.3 is also applied to this pair correlation image, $B'_{\mathrm{n,m}}$. $B'_{\mathrm{n,m}}$ represents the pair correlation function of the sum of all images. In contrast, A' represents the sum of all individual pair correlation functions. The normalized pair correlation image is obtained from dividing the average pair correlation image, A', with the pair correlation image, B', and number of pictures, $N_{\mathrm{p}} = 5,000$.

$$C_{\mathrm{n,m}} = A'_{\mathrm{n,m}}/(N_{\mathrm{p}} B'_{\mathrm{n,m}}) \quad . \tag{3.7}$$

Next, I apply a coarse-graining (and binning) operation to the image in order to reduce fluctuation within the image. The binning size varies between 2×2 and 5×5, depending on the experimental requirements. The resulting normalized pair correlation image with coarse graining is shown in Figure 3.9(f).

The center of the pair correlation image indicates the origin of the separation vector. A strong correlation enhancement ring (dark ring with a radius of about 10 μm) indicates that atoms are excited under isotropic interactions and are consequently located at a well-defined separation. A white region near the center that has approximately the same diameter as the blip indicates that the peak detection algorithm cannot separate two blips with separation less than the blip diameter. The lighter region inside the ring indicates the blockade radius.

An enhancement occurs at a specific radius and can be changed based on the interaction potentials. More details about Rydberg atoms under the isotropic van der Waals interactions and the anisotropic dipole-dipole interactions are described in

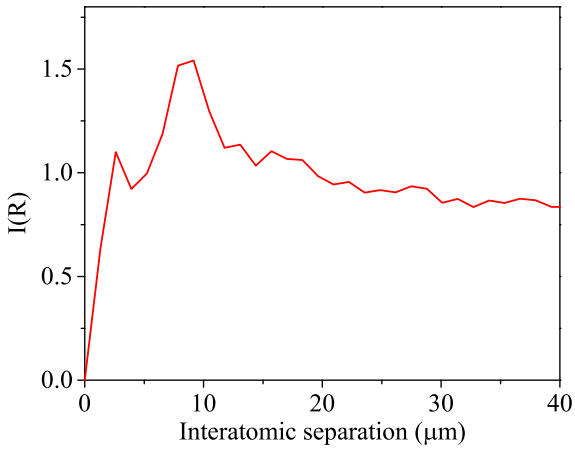

Figure 3.10: Angular integral of Figure 3.9(f).

Chapter IV and Chapter V, respectively.

Because the pair correlation image is obtained from the 2-dimensional projection of Rydberg atoms in the 3-dimensional excitation volume, there are cases when detected ions appear to be close to each other in the image plane. This would reduce the visibility of the pair correlation enhancement but does not significantly change the radius of the enhancement ring, as observed in a simulation (see Chapter IV).

3.6.1 Angular integral

To quantitatively explain the spatial correlation between atoms, I integrate the pair correlation value over the angle around the center of the pair correlation image. While the actually applied azimuthal averaging procedure is an operation in a discretize position space, it can be visualized by the following integral:

$$I(R) = \frac{\oint A'(R,\phi)d\phi}{N_{\mathrm{p}} \oint B'(R,\phi)d\phi} \quad . \tag{3.8}$$

I apply the coarse-graining operation by binning the angular average using a bin size of 5 pixels in order to smooth out the fluctuation caused by pixelation of the images. An $I(R)$ that corresponds to Figure 3.9(f) is shown in Figure 3.10. The enhancement

peak in the $I(R)$ represents the most probable separation, R_{p}, between two atoms. This R_{p} corresponds to the radius of the enhancement ring in the pair correlation image. The values of R_{p} are obtained from local parabolic fits centered approximately at the peak positions of the $I(R)$.

The pair correlation function between Rydberg atoms versus the interatomic separation has been calculated in [14]. The correlation function is zero for small separations due to the blockade and approaches an asymptotic value of 1 at large distances where the atoms are uncorrelated. It is shown in the calculation that, when the detuning has the same sign as the van der Waals shift, atom pairs are preferentially excited at separations that give a two-photon resonance and the enhancement peak then appears in the pair correlation function.

The pair-correlation signal at the distance $R < R_{\mathrm{p}}$ mostly comes from the projection of 3-dimensional sample onto the 2-dimensional observation plane. Sometimes there is a small peak (at about 3 μm in Figure 3.10) that is identified to be an artifact caused by ion feedback from the TIP. Field electrons that impact on the TIP release a secondary ion that reaches the MCP close to the primary (Rb^{+}) ion.

CHAPTER IV

Measurement of van der Waals interaction by atom trajectory imaging

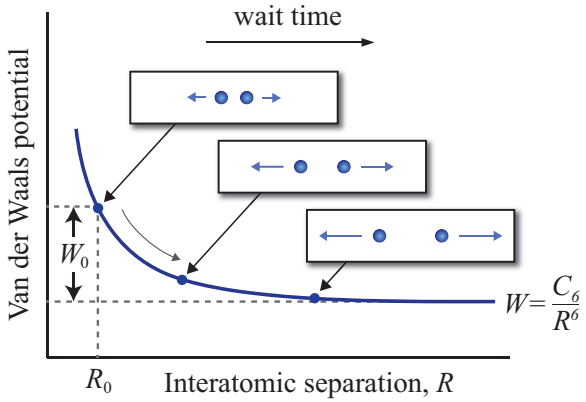

Figure 4.1: Van der Waals potential versus separation between two Rydberg atoms. The Rydberg atoms (blue circles) at the initial separation, R_0, repel each other due to the repulsive van der Waals force. The trajectory of the atoms can be observed by imaging the atom positions at various wait times. The (final) kinetic-energy release equals the initial van der Waals potential, W_0.

The van der Waals interaction between individual Rydberg atoms is important in the description and control of interactions in few- and many-body dynamics studies, which have been of considerable interest in recent years. In this chapter, I describe the use of the Rydberg-atom imaging technique to probe the van der Waals interactions between Rydberg atoms.

Figure 4.1 illustrates rubidium Rydberg atoms in S states that are subject to isotropic repulsive van der Waals interactions, $W = C_6/R^6$, where C_6 is the van der Waals interaction coefficient and R is the interatomic separation. Two Rydberg atoms

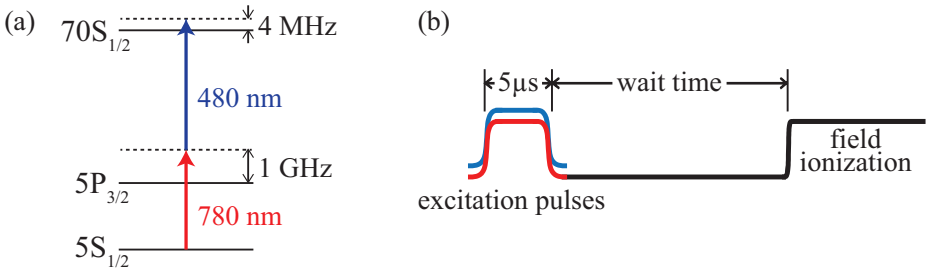

Figure 4.2: (a) Energy level diagram for an excitation of ^{85}Rb atom from a $5S_{1/2}$ state to a $70S_{1/2}$ state. (b) Experimental timing.

at an initial separation, R_0, repel each other due to the repulsive van der Waals force. The evolution of the interatomic separation can be observed by imaging the atom positions as a function of wait time. The final kinetic-energy release equals the initial van der Waals potential, W_0. In addition to observing the interatomic separation increase with time, one can also extract C_6 using this method.

For the described kinematic method to work, it is important to prepare the Rydberg-atom pairs at a well-defined initial separation. In this work, pairs of $70S_{1/2}$ rubidium Rydberg atoms are prepared at such a well-defined separation by detuning an excitation laser and utilizing the R^{-6} dependence of the van der Waals interaction [24, 100]. After preparation, the atoms are subject to van der Waals forces. The effect of the forces is observed by tracking the interatomic distance between the Rydberg atoms and probing them after they have been allowed to move for selected wait times. The experiment also shows that van-der-Waals-induced motion causes dephasing in coherently shared Rydberg excitations (superatoms) [67, 68].

4.1 Experimental method

The energy level diagram for the Rydberg atom excitation is shown in Figure 4.2(a). ^{85}Rb atoms in $5S_{1/2}$ states are excited to the $70S_{1/2}$ state using 780 nm and 480 nm laser pulses with 5 μs durations and $\approx$1 GHz red-detuning from the

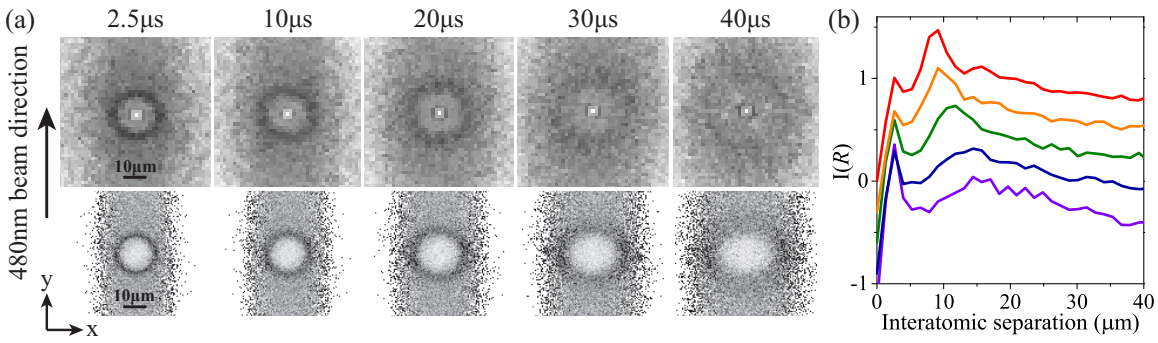

Figure 4.3: (a) Experimental (top row) and simulated (bottom row) pair correlation images for the selected wait times. The linear grayscale ranges from 0 (white) to 2 (black). Values of 1, <1, and >1 indicate no correlation, anticorrelation, and positive correlation, respectively. (b) Angular integrals $I(R)$ of (a) at wait times (from top to bottom): 2.5, 10, 20, 30, and 40 μs. The y axis is for the top curve; for clarity, the other curves are shifted down in equidistant intervals of 0.3.

$5P_{3/2}$ intermediate state. The excitation of the $70S_{1/2}$ Rydberg level is detuned by $\Delta = 4 \pm 2$ MHz with respect to the two-photon resonance. After excitation, the Rydberg atoms are allowed to move for selected wait times before their positions are measured by applying a field ionization pulse, as shown in Figure 4.2(b). The excitation volume is 470 μm above the TIP, which results in a measured magnification of ≈ 155. I select the 5,000 images with the highest number of detections out of 10,000 images taken in each dataset. The atom positions, the pair correlation images, and the $I(R)$ curves are extracted from these 5,000 images using the procedure explained in Chapter III.

4.2 Pair correlation images and angular integral

The pair correlation images for various wait times are presented in Figure 4.3(a). The average interaction time of the Rydberg atoms is the wait time plus half the excitation pulse length (*i.e.* wait time + 2.5 μs). The pair correlation image for a wait time of 2.5 μs exhibits strong correlation enhancement at a fairly well-defined radius. The initial correlation is critical for the trajectory experiment as it must be sufficient to track Rydberg-pair trajectories out to long wait time ($\approx$40 μs in this experiment).

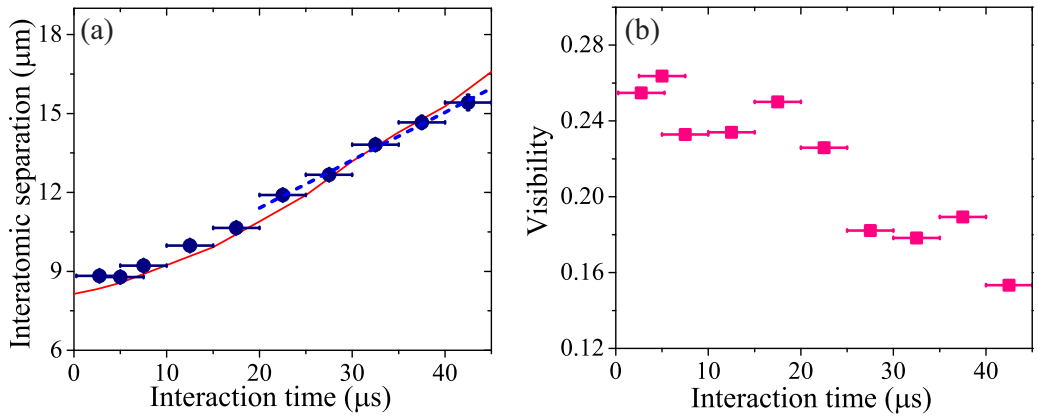

Figure 4.4: (a) Interatomic separations between Rydberg-atom pairs as a function of interaction time, obtained from the peak positions in the $I(R)$ curves. The blue dashed line represents a linear fit at wait times 20-40 μs. The red solid line shows simulation results obtained for $\Delta = 3$ MHz. (b) The visibility of the experimental pair correlation enhancement as defined in Equation (5.4.1).

With increased wait time, the radius of enhanced pair correlation increases, reflecting an increase of interatomic separation due to the repulsive van der Waals interaction. At long wait times, the enhancement ring is blurred out mostly due to initial thermal atom velocities in the MOT (temperature ~ 100 μK).

Figure 4.3(b) shows the angular integral, $I(R)$, of the experimental pair correlation image in Figure 4.3(a). The most probable separation, $R_{\mathrm{p}}(t)$, between Rydberg-atom pairs at wait time t is extracted (see Section 3.6.1) from the corresponding $I(R)$. The resulting $R_{\mathrm{p}}(t)$ are presented in Figure 4.4(a). A cursory inspection of this figure already shows that the trajectory of the Rydberg-atom pairs is characterized by an initial acceleration phase, during which the initial van der Waals potential energy, W_0, is converted into kinetic energy and a later phase during which the atoms separate at a fixed velocity.

The visibility of the pair correlation enhancement, also shown in Figure 4.4(b), is given by

$$\text{Visibility} = \frac{(I_{\max} - I_{\min})}{(I_{\max} + I_{\min})} \quad , \tag{4.1}$$

where $I_{\max}$ is the peak value of $I(R)$ in the range $\gtrsim 10$ μm and $I_{\min}$ is the minimal

value near 7 μm. The drop in visibility is due to the thermally-induced blurring of the correlation ring at late times.

4.3 Extraction of the van der Waals coefficient C_6

To extract the van der Waals C_6 coefficient, one may consider an isolated atom pair excited at an initial separation R_0. The initial van der Waals energy is

$$W_0 = \frac{C_6}{R_0^6} = 2\Delta \quad , \tag{4.2}$$

where Δ is the laser detuning from the $70S_{1/2}$ state.

Over the experimentally investigated wait times, the entire initial van der Waals energy, W_0, becomes converted into kinetic energy. With the reduced mass of the atom pair, μ, and the terminal relative velocity, V_t, then

$$W_0 = \frac{C_6}{R_0^6} = \frac{1}{2}\mu V_\mathrm{t}^2 \quad . \tag{4.3}$$

R_0 is obtained from the weighted average of the fit results $R_\mathrm{p}(t)$ at the earliest times used in the experiment [the first two points in Figure 4.4(a)]. The averaging is valid because during the first few microseconds after excitation the Rydberg atoms are frozen in place due to their inertia. The statistical weights are given by the inverse squares of the fitting uncertainties of R_p at 250 ns and at 2.5 μs (see Appendix A). Here, $R_0 = 8.78$ μm with a net fitting uncertainty of 0.02 μm. To determine V_t, I perform a linear fit at wait times 20-40 μs [blue dashed line in Figure 4.4(a)] and obtain $V_\mathrm{t} = 0.182$ m/s with a fitting uncertainty of 0.008 m/s. Including the 2% magnification uncertainty, it follows that $C_6 = \frac{1}{2}\mu V_\mathrm{t}^2 R_0^6 = (5.4 \pm 1.0) \times 10^{-58}$ Jm^6.

The final relative uncertainty of C_6 follows from three statistically independent contributions: the magnification uncertainty, the fit uncertainty for V_t, and the fit uncertainty for R_0. The respective powers at which these quantities enter into C_6

are 8, 2, and 6. Factoring in these powers, the three quantities contribute respective independent uncertainties of 16%, 8.9%, and 1.4% to the relative uncertainty of C_6, leading to the total relative uncertainty of 18%. In this method, achieving a small magnification uncertainty is particularly important. More details about the uncertainty calculation are provided in Appendix A.

Note that from Equation (4.2), C_6 can, in principle, be obtained from spectroscopic measurement, $C_6 = 2\Delta R_0^6$ [6]. This method requires a well-defined R_0, a narrow laser linewidth, and accurate knowledge of Δ. In this work, the relative uncertainty in R_0^6 is about 12% (because the relative magnification uncertainty is 2%). In comparison, the uncertainty arising from $\Delta = 4 \pm 2$ MHz is much larger. Taking all uncertainties into account, Equation (4.2) leads to values of C_6 ranging from $7{\times}10^{-58}$ Jm^6 to $40{\times}10^{-58}$ Jm^6. Therefore, Equation (4.2) only allows me to perform a crude order of magnitude prediction of C_6. The main weakness of Equation (4.2) is that the C_6-values derived from it directly reflect the large relative uncertainty in Δ. Here, it is therefore much better to base the determination of C_6 on a measurement of the initial R_0 rather than a measurement of the laser detuning Δ.

4.4 Trajectory Simulation

A classical 3D simulation of the dynamics of Rydberg atoms interacting due to an isotropic van der Waals force has been performed to confirm the interpretation of the experiment. The simulation volume of (140 μm)^3 exceeds the experimentally relevant volume by about a factor of two in each dimension. The 480 nm excitation beam propagates along the y direction. The excitation volume in the transverse directions (x and z) is limited by the size of the excitation beam ($w_0 = 8$ μm). The number of simulations is the same as the number of images analyzed in the experiment (5,000).

Rydberg-atom positions and velocities are initialized and then propagated using a Runge-Kutta integrator that includes all pair-wise interatomic forces. In the initialization and integration procedures, $C_6 = 5.7 \times 10^{-58}\mathrm{Jm}^6$ [90] is used. To avoid edge effects, the xy processing area in the images is cropped to $(70\ \mu\mathrm{m})^2$ before calculating the average pair-correlation images and the radial functions $I(R)$.

4.4.1 Rydberg-atom initialization

The number of excited Rydberg atoms n_{Ryd} in each simulation is randomly obtained from a Poissonian distribution with an average of 8 atoms and a maximum limit of 20 atoms to match the number of atoms detected in the experiment. An initial trial position of each particle is drawn from a Gaussian distribution in x and z with a $w_0 = 8\ \mu$m and a uniform distribution in y, in close analogy with the experiment. A Rydberg atom is created if the excitation probability is larger than a number randomly drawn between 0 and 1. The excitation probability is a Gaussian centered at Δ with a FWHM of 4 MHz given by the excitation bandwidth (note that FWHM$= 2\sqrt{2\ln 2}\sigma \approx 2.355\sigma$),

$$P_{\mathrm{ex}}(\Delta) = e^{-(W_{\mathrm{vdw}}-\Delta)^2/\left(2\sigma^2\right)} \quad , \tag{4.4}$$

where W_{vdw} is the van der Waals interactions between a trial atom and all other atoms j which are already excited into the Rydberg state,

$$W_{\mathrm{vdw}} = \sum_j \frac{C_6}{R_{\mathrm{j}}^6} \quad . \tag{4.5}$$

$\mathbf{R}_{\mathrm{j}} = \mathbf{r}_{\mathrm{trial}} - \mathbf{r}_{\mathrm{j}}$ is a separation vector between an atom located at a trial position $\mathbf{r}_{\mathrm{trial}}$ and all other atoms located at $\mathbf{r}_{\mathrm{j}}$. This procedure is repeated with new trial positions until the desired number of n_{Ryd} Rydberg atoms has been reached. The initial center-of-mass velocities of the atoms are assigned using a Maxwell distribution

at temperature 100 μK. At this temperature, the most probable speed of atoms is 0.14 m/s.

Since the detuning is substantial, the first pair of Rydberg atoms is simultaneously excited via off-resonant excitation [24] (because the state in which there is only one Rydberg atom present is off-resonant). Therefore the value of detuning in Equation (4.4) for the first Rydberg-atom pair is set to be twice the laser detuning 2Δ. For the excitation of additional atoms, I use Δ to simulate the facilitated excitation of those atoms, which can be a near-resonant process with other atoms already present [29]. Detunings due to the Doppler effect are about 300 kHz and are neglected.

The force on the excited atom is obtained from the gradient of the van der Waals potential in Equation (4.5), which leads to isotropic dynamics of atom trajectories. The van der Waals force has only a radial component given by

$$\mathbf{F} = -\nabla W_{\mathrm{vdw}} = \sum_j \frac{6C_6}{|R_j|^7}\hat{\mathbf{R}}_{\mathrm{j}} \quad . \tag{4.6}$$

The acceleration is $\mathbf{a} = \mathbf{F}/m$ where m is a mass of a ^{85}Rb atom.

4.4.2 Runge-Kutta integration

I use the Runge-Kutta integration to propagate the position and the velocity of atoms based on the initial parameters described in the previous section. The Runge-Kutta method is a numerical method for solving an ordinary differential equation,

$$\dot{y}(t) = f(t, y) \quad , \tag{4.7}$$

with known initial conditions,

$$y(t_0) = y_0 \quad , \quad \dot{y}(t_0) = f(t_0, y_0) \quad . \tag{4.8}$$

The approximation of y_{n+1} at time $t_{n+1} = t_n + \Delta t$ is

$$y_{n+1} = y_n + \frac{1}{6}\Delta t(k_1 + 2k_2 + 2k_3 + k_4) \quad , \tag{4.9}$$

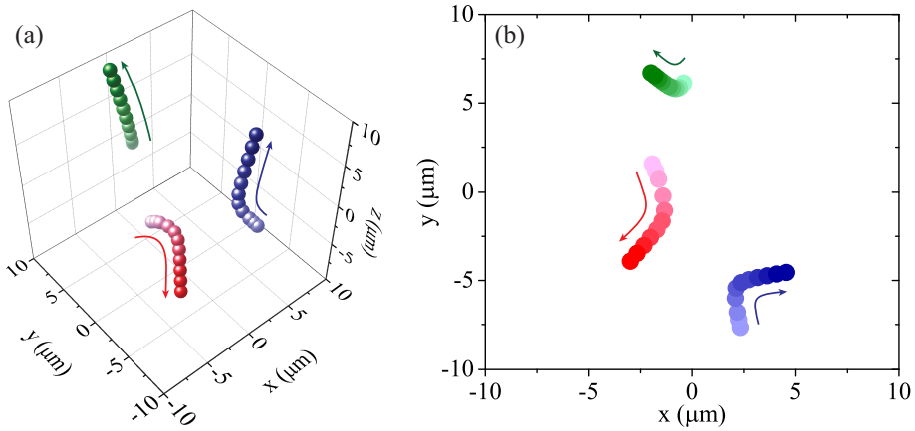

Figure 4.5: Trajectory simulation. The position of atoms are recorded at the wait times 0 (lightest circle) to 45 μs (darkest circle). (a) Position of atoms in 3 dimensions. (b) Projection of (a) onto the xy plane.

where the increments k_1, k_2, k_3, and k_4 are defined to be

$$\begin{aligned} k_1 &= f\left(t_n, y_n\right) \\ k_2 &= f\left(t_n + \frac{\Delta t}{2}, y_n + \frac{\Delta t}{2}\, k_1\right) \\ k_3 &= f\left(t_n + \frac{\Delta t}{2}, y_n + \frac{\Delta t}{2}\, k_2\right) \\ k_4 &= f\left(t_n + \Delta t, y_n + \Delta t\, k_3\right) \end{aligned} \tag{4.10}$$

In this trajectory calculation, the differential equations and initial conditions for position and velocity propagations are given by

$$\begin{aligned} &\text{position}: \quad \dot{\mathbf{r}}(t) = \mathbf{v}(t), \quad \mathbf{r}(t_0) = \mathbf{r}_0 \\ &\text{velocity}: \quad \dot{\mathbf{v}}(t) = \mathbf{a}(t), \quad \mathbf{v}(t_0) = \mathbf{v}_0 \end{aligned} \tag{4.11}$$

The time step used in this simulation is $\Delta t = 50$ ns. I record the atom positions at the wait times up to 45 μs (similar to the experiment). Figure 4.5 shows an example atom trajectories from the simulation. Atoms that are moving closer to each other due to their initial velocities change their directions over time due to the van der Waals force.

4.4.3 Simulated pair correlation images and angular integrals

The resulting pair correlation images are shown for the case $\Delta = 3$ MHz in the bottom row in Figure 4.3. This case is presented because it provides the best agreement with the experiment among all simulated detuning cases. Black pixels along the left and right edges of each pair correlation are an artifact due to the normalization used in the image processing.

From the simulated pair correlation images I calculate the $I(R)$ curves in order to obtain the most probable separations, $R_{\mathrm{p}}(t)$, between Rydberg-atom pairs at each interaction time [see solid curve in Figure 4.4(a), which is for $\Delta = 3$ MHz]. The simulated and experimental results for $R_{\mathrm{p}}(t)$ are in good agreement. In order to test how well the experimental procedure reproduces the C_6 coefficient that underlies the atomic interactions, I evaluate the simulated results for $R_{\mathrm{p}}(t)$ using the same method. The results for R, V_{t} and C_6 extracted from the simulated $R_{\mathrm{p}}(t)$ curves are shown in Table 4.1 for four choices of Δ. These C_6 values agree, within the uncertainties, with the value that has been entered as a fixed input into the simulation. This finding validates the experimentally used procedure; in particular, it is seen that the method is not very sensitive to Δ, and the fact that I analyze projected rather

Table 4.1: Comparison of calculated, experimental, and simulated results for C_6, R, and V_{t}.

	R (μm)	V_{t} (m/s)	C_6 ($\times 10^{-58}$Jm^6)
Calculation [90]			5.77±0.14
Experiment	8.8±0.2	0.182±0.009	5.4±1.0
Simulations			
$\Delta = 2$ MHz	8.85±0.06	0.17±0.02	4.9±1.0
$\Delta = 3$ MHz	8.14±0.03	0.233±0.005	5.5±0.3
$\Delta = 4$ MHz	7.76±0.05	0.278±0.003	6.0±0.3
$\Delta = 5$ MHz	7.51±0.04	0.28±0.01	4.9±0.5

than three-dimensional trajectories does not alter the extracted C_6. The experimental and calculated [90] C_6 values are also included in Table 4.1 for reference.

The experimental, simulated, and expected values for C_6 in Table 4.1 are in reasonable agreement. Moreover, I observe that the entire simulated curve of $R_p(t)$ with $\Delta = 3$ MHz matches the experimental result very well [see Figures. 4.3(a) and 4.4(a)]. Overall, the simulations lend credibility to the experimental method of extracting C_6-values from the measured data.

Note that higher-order quadrupole-dipole and quadrupole-quadrupole interaction potentials, which scale as R^{-7} and R^{-8}, are not important at the distances relevant in this work, at the current level of precision. This has been verified by a molecular-potential calculation.

4.4.4 Dimensional effect on pair correlation image and angular integrals

There has been question if the analysis of a 2-dimensional (2D) projection of the atom positions can be used to analyze the kinetic effects in a 3-dimensional (3D) experiment. To verify that this method works, I calculate the $I(R)$ curves from the same simulation but taking atom positions in 3D [use all x, y, and z components,

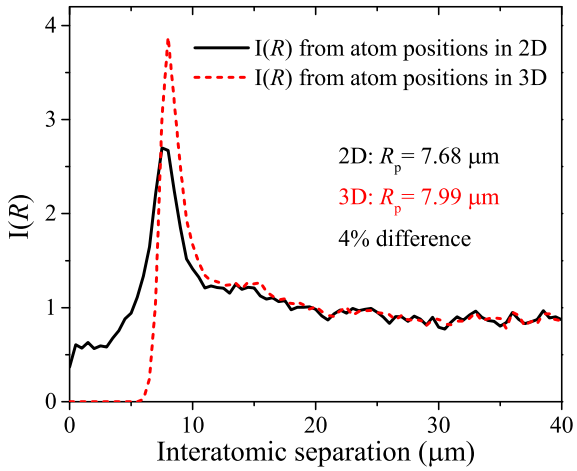

Figure 4.6: $I(R)$ curves obtained from a simulation using 5 μs excitation pulse with zero wait time at $\Delta = 4$ MHz.

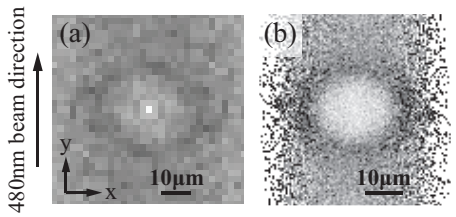

Figure 4.7: Pair correlation function at wait time 30 μs from (a) experiment and (b) simulation at $\Delta = 3$ MHz. The anisotropic expansion of the atom ensemble causes the radius of enhanced pair correlation along the transverse direction (x) to be larger than along the excitation beam direction (y).

see Figure 4.5(a)] and in 2D [use only x and y components, see Figure 4.5(b)]. The resulting $I(R)$ curves are presented in Figure 4.6. It can be seen that, at small R, the $I(R)$ curve from the 3D calculation becomes zero due to the blockade effect. The correlation at the same position from the 2D calculation is not zero due to the detection of smaller (apparent) separation distance between atoms on the projection plane. In addition, the position of the most probable separation, R_{p} (peak position of the pair correlation enhancement), of the 3D curve is about 4% larger than one of the 2D curve. This means that the dimensionality effect reduces the visibility of the enhancement peak [Equation (5.4.1)] but it does not significantly affect the position of the pair correlation enhancement peak.

4.5 Anisotropic expansion

Close inspection of the pair correlation functions from the simulation presented in Figure 4.3 reveals anisotropic expansion behavior: the radius of enhanced pair correlation is larger in the x than in the y direction. In several experimental data sets there is an evidence of anisotropic expansion, such as in the experimental result shown in Figure 4.7(a). The anisotropic expansion is due to the cylindrical shape of the excitation volume (not the interatomic interaction, which is isotropic). Since the blockade radius is close to the transverse size of the excitation region, at most

two atoms can be excited side-by-side in the x direction, leading to free, unimpeded expansion along that direction. In contrast, more than two Rydberg atoms can be created along the y direction. Therefore, along y the expansion is slowed down due to multiple-atom repulsion. In the experiment, the overall Rydberg-atom density is high enough to sometimes observe this effect.

4.6 Interaction between individual atoms (not superatoms)

A question of interest is whether the interatomic force is acting on superatoms (Rydberg excitations shared among a number of ground-state atoms) or on individual atoms. It can be seen that the simulation agrees well with the experiment when I assume that the effective mass of the interacting entities is half the rubidium atom mass. If the interacting entities were superatoms, the mass used to calculate C_6 in Equation (4.3) would have to equal the mass of several tens of atoms that are located within the blockade region. The obtained C_6 would also be about 10 times larger than the value obtained from the experiment. The C_6 coefficients in Table 4.1 demonstrate that the interacting entities are indeed individual atoms. This finding implies that, during the course of the van der Waals interaction, excitations within superatoms become projected onto individual atoms, which are then ejected from the initial superatom volumes. The phenomenon has been predicted in [67] for superatom clouds interacting via a dipole-dipole interaction. In this work, I arrive at a similar conclusion for van-der-Waals interacting Rydberg atoms in a 3D system.

4.7 Summary

In summary, I have studied the trajectory of Rydberg-atom pairs interacting by repulsive, isotropic van der Waals interactions. The interactions are observed through an expansion of the pair correlation enhancement and the most probable separation

between atoms. The C_6 coefficient is extracted from a kinematic analysis of the experimental data. The results agree well with simulations and molecular-potential calculations. I have noticed indications of an anisotropic effect in the expansion, caused by the excitation geometry.

The work presents the first measurement of a C_6-coefficient based on binary atom kinetics and not on spectroscopic or other data. The kinetic method is advantageous in cases where laser drifts and bandwidths are a concern, as has been the case in this work. This method will also be applicable in measurements in which the atom pairs are initialized via a non-optical process, such as adiabatic quantum-state transformation in Reference [101]. Also, I use a random ensemble of many ground-state atoms, in which I implant a number of Rydberg excitations that is generally larger than two (in most realizations). Hence, there is less control needed during the sample preparation than in Reference [6], which is based on deterministic preparation of isolated atom pairs. More importantly, this aspect of the measurement implies that, while the Rydberg excitations initially are superatoms, the kinetic interaction occurs between individual atoms, not superatoms. The question of how the interaction between superatoms can cause coherence loss and superatom breakup currently is of considerable interest.

For instance, in Reference [68] it was found that double-Rydberg excitations lead to significant interaction-induced dephasing of collective Rabi oscillations. Further, it was recently observed that the fidelity of pairs of ensemble q-bit states is limited by Rydberg-Rydberg superatom interactions [102]. In future work, a combination of shorter pulses and a more intense 480 nm laser might lead to better time resolution, while maintaining a high signal-to-noise ratio. Improved time resolution can provide insight into the early dynamics, during which superatoms are likely being projected

onto individual atoms. Other investigations may also be focused on Rydberg atoms interacting via different types of interactions, such as the dipole-dipole interactions, and measurements of their dispersion coefficients and anisotropy behaviors.

CHAPTER V

Atom-pair kinetics with strong electric-dipole interactions

The method used to measure van der Waals interactions in Chapter IV is extended to study electric-dipole interactions between atom pairs in this chapter. The distinctions between the van der Waals and the electric-dipole interactions are in the overall interaction strength, the scaling with the internuclear separation (R^{-6} for the van der Waals and R^{-3} for the electric-dipole interactions), and the (an)isotropic behavior. To study the kinetics due to the dipole-dipole interaction on the atomic scale, a combination of large interaction strength and high magnification of the atom-imaging system is required.

It is challenging to directly prepare Rydberg atoms in a highly dipolar state because the strong interaction leads to density limitation due to a strong excitation blockade. In this chapter, I describe an adiabatic state-preparation method, which I then utilize to prepare Rydberg atoms to overcome the density limitation. The measured pair correlation images demonstrate a first direct visualization of dipolar, anisotropic atom-pair kinetics, which is similar to the visualization of magnetic-dipole field lines with iron filings that is a common activity in science education.

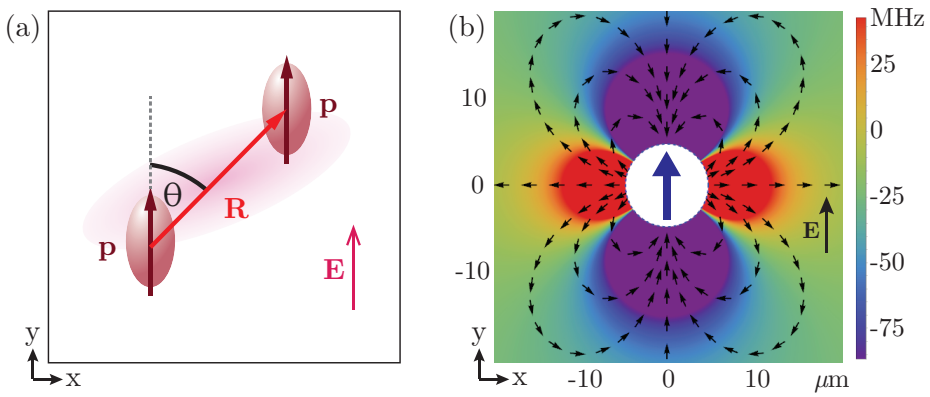

Figure 5.1: (a) Two identical dipoles $\mathbf{p}$ whose center-of-mass positions are separate by $\mathbf{R}$. Θ is the angle between $\mathbf{R}$ and the direction of the dipole vectors $\mathbf{p}$. (b) Color map of the dipolar potential in Equation (5.1) and corresponding force vectors in Equation (5.2) as a function of $\mathbf{R}$ for a pair of dipoles pointing along y.

5.1 Electric-dipole interaction

The interaction potential between two electric dipoles $\mathbf{p}_1$ and $\mathbf{p}_2$ located at center-of-mass positions $\mathbf{r}_1$ and $\mathbf{r}_2$ is described by [89] (in atomic units)

$$V_{\mathrm{dd}} = \frac{\mathbf{p}_1 \cdot \mathbf{p}_2 - 3(\hat{\mathbf{n}} \cdot \mathbf{p}_1)(\hat{\mathbf{n}} \cdot \mathbf{p}_2)}{|\mathbf{r}_1 - \mathbf{r}_2|^3} \quad , \tag{5.1}$$

where $\hat{\mathbf{n}}$ is the unit vector pointing along the internuclear coordinate, $\mathbf{R} = \mathbf{r}_1 - \mathbf{r}_2$. In this work, the dipole moment of the atoms is pinned to the direction of the external electric field $\mathbf{E}$. Hence $\mathbf{p}_1$ and $\mathbf{p}_2$ are identical and point along the same direction, so $\mathbf{p}_1 = \mathbf{p}_2 = \mathbf{p}$, as shown in Figure 5.1(a). The potential leads to anisotropic dynamics of atom-pair trajectories. For two identical dipoles pointing along the same direction, the dipolar force has radial and polar components given by

$$\begin{aligned} F_{\mathrm{R}} &= \frac{3p^2}{R^4}[1 - 3\cos^2(\Theta)] \quad , \\ F_{\Theta} &= \frac{-3p^2}{R^4}[2\cos(\Theta)\sin(\Theta)] \quad , \end{aligned} \tag{5.2}$$

where Θ is the angle between the internuclear separation vector $\mathbf{R}$ and the dipole vectors $\mathbf{p}$. The potential in Equation (5.1) and the force vector field in Equation (5.2) are shown in Figure 5.1(b).

A critical problem that first had to be solved is that the strong dipole-dipole interaction potential leads to a strong laser excitation blockade [7, 9], which prevents the direct laser excitation of pairs of dipolar Rydberg atoms at small initial separations. This amounts to a blockade-induced density limitation that is more severe in systems with stronger interactions, and that can prevent the study of strong dipolar forces between atom pairs.

5.2 Landau-Zener adiabatic passage

I overcome the density limit imposed by the excitation blockade by initially preparing Rydberg atoms under conditions where they are only subject to weak van der Waals interactions. Rydberg atom samples are prepared with relatively small interatomic separations. In order to switch on strong dipole-dipole interactions, the atoms are subsequently transferred into a highly dipolar state via a Landau-Zener adiabatic passage through an avoided crossing [101, 103].

The illustration of the adiabatic state transformation is presented in Figure 5.2(a). Here, the energy of the two-level system is a function of an external electric field. Initially, an atom pair is subject to weak van der Waals interaction (blue circles). When the external electric field is swept through the avoided crossing, the final state of

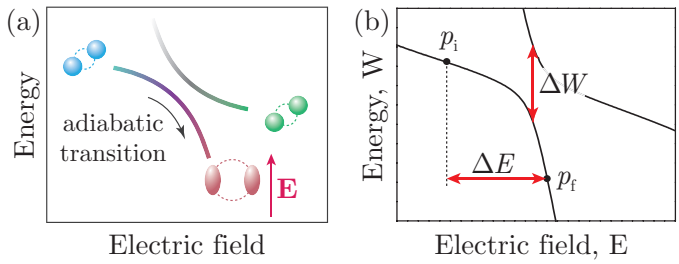

Figure 5.2: Landau-Zener state transformation. (a) Illustration of the adiabatic state transformation. (b) Parameters in the Stark map of the avoided crossing that are needed to calculate the probability of adiabatic state transformation [Equation (5.4)]. The electric dipole moments of the initial and final states, p_i and p_f, are given by $p_{i,f} = -dW_{i,f}/dE_{i,f}$.

the atoms can be either a low-dipolar state (green circles) through a diabatic state transformation or a highly-dipolar state (pink ovals) through an adiabatic state transformation. The permanent electric dipole moment of the highly-dipolar state is larger than that of the initial state. The probability of the adiabatic state transformation is obtained from the Landau-Zener formula, which leads to (in SI units)

$$P_{\text{adia}} = 1 - e^{(-\Delta t/\tau)} \quad , \tag{5.3}$$

with

$$\tau = \frac{\hbar \Delta E |p_{\text{f}} - p_{\text{i}}|}{2\pi(\Delta W/2)^2} \quad , \tag{5.4}$$

where $\Delta E = E_{\text{f}} - E_{\text{i}}$ is the range of the linear electric-field sweep, p_{i} and p_{f} are electric dipole moments of the initial and final state, ΔW is the minimal gap splitting at the center of the avoided crossing, and Δt is the electric field ramp duration. Note that the electric dipole moment of the atoms is calculated from the slopes of the Stark states (the potential energy $W = -\mathbf{p}\cdot\mathbf{E}$). In addition, if the gap size is small, the ramp duration needs to be long in order to make P_{adia} close to unity. These parameters are illustrated in Figure 5.2(b).

For rubidium Rydberg atoms, the avoided crossings between Rb $nS_{1/2}$ Stark states and the hydrogenic manifold appear at electric fields that are a fraction of the Inglis-Teller field, $1/(3n^{*5})$, where n^* is an effective principal quantum number [75]. A preferable state and avoided crossing for conducting the experiment have the following properties:

1. This state must have an avoided crossing where the gap size is large enough to be experimentally resolved in the Stark spectra.
2. The passage behavior through this crossing is almost entirely adiabatic for the utilized duration of the electric-field sweep.

3. The range of this avoided crossing as a function of applied electric field is small enough that after adiabatic passage the permanent electric-dipole moment of the atoms does not significantly depend on the exact value of the applied electric field.

4. The separations between atoms are resolvable using the ion imaging technique explained in Chapter III.

This work utilizes the crossing of rubidium $50S_{1/2}$ with the manifold of $n = 47$ hydrogen-like dipolar states in the applied electric field. The Stark map of the rubidium $50S_{1/2}$-like state (with the electric field pointing along the y direction) is shown in Figure 5.3. The 1^{st} to 4^{th} crossings have small energy gaps. The 5^{th} crossing is the first one that can be clearly resolved. The experiment is performed at the 6^{th} crossing, marked by a red square in Figure 5.3. This crossing is located at the electric field value 2.76 V/cm and has a gap size of 40 MHz.

The $50S_{1/2}$-like atoms prepared at 0.1 V/cm below the avoided crossing have a small electric dipole moment of 1.26×10^{-27} C m. This state has an oscillator strength that is sufficiently large for optical excitation. The number of excitations are presented using a grayscale in Figure 5.3. The S-like Rydberg state has stronger signal compared to the hydrogenic state. Also, since atoms in the S-like Rydberg state mostly interact via a weak isotropic van der Waals potential (see the calculated wavefunction for 2.66 V/cm in Figure 5.4), the Rydberg-atom density limit imposed by the excitation blockade is quite high ($\sim 10^9$ cm^{-3}). The S-like Rydberg atoms are adiabatically transferred into a highly-dipolar state by the means of an adiabatic passage through a level crossing. The dipolar state has a dipole moment of 20.3×10^{-27} C m, resulting in an enhancement of dipolar interaction between Rydberg atoms $V_{\text{dd,f}}/V_{\text{dd,i}} = (p_{\text{f}}/p_{\text{i}})^2$ by a factor of about 260. The estimate shows that the presented procedure is a highly

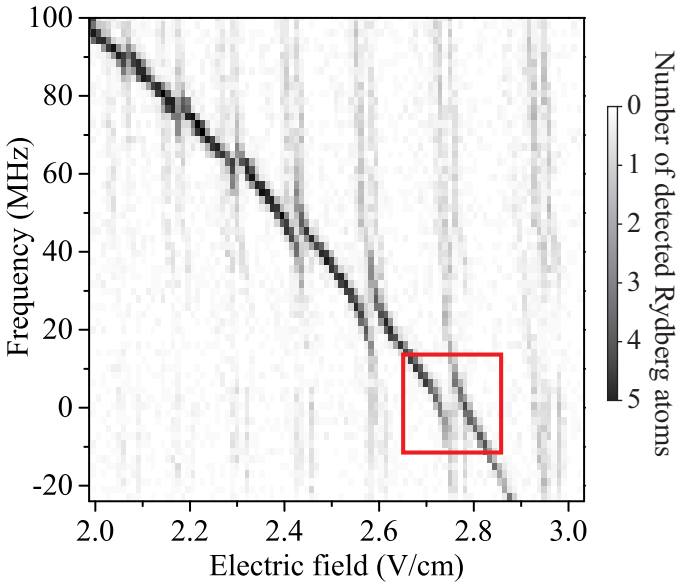

Figure 5.3: Stark map of the rubidium $50S_{1/2}$-like state showing the first six avoided crossings with the manifold of $n = 47$ hydrogen-like states. The experiment is performed at the sixth avoided crossing marked by the red square. The linear grayscale represents the number of detected Rydberg atoms, ranging from 0 (white) to 5 (black).

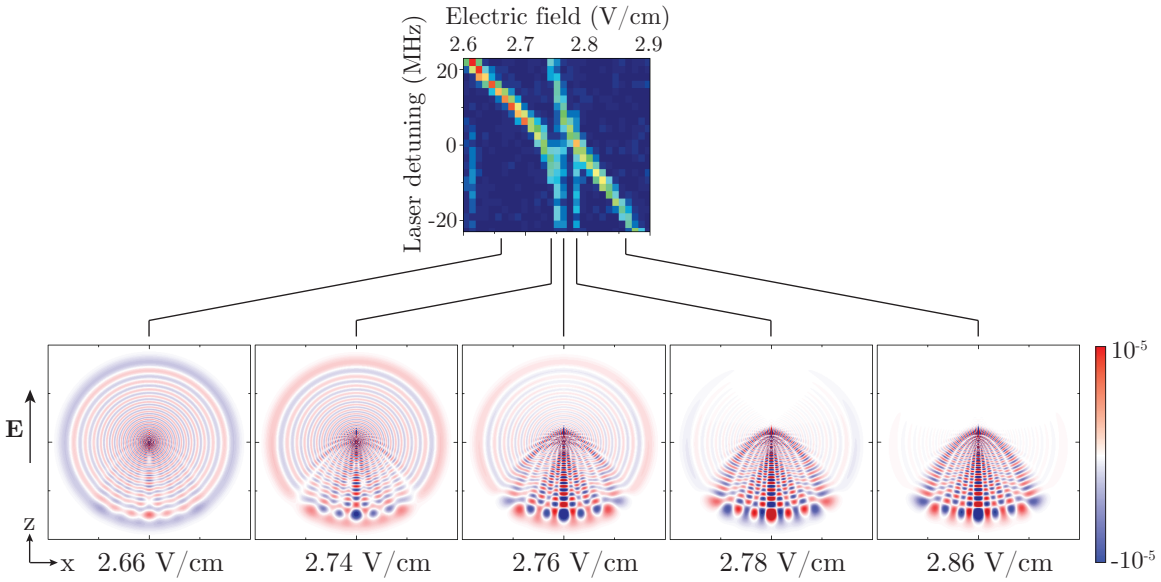

Figure 5.4: Adiabatic transformation of the wavefunction, starting at the $50S_{1/2}$-like state calculated at electric field 2.66 V/cm (0.1 V/cm before the 6^{th} crossing). During the electric field ramp along z, the wavefunction of the atom are transformed to a highly-dipolar state. The final state is calculated at the electric field 2.86 V/cm (0.1 V/cm after the 6^{th} crossing). All wavefunctions are plotted on the same scale, $-5000a_0 < x, z < 5000a_0$. The colorscale on the right represents the amplitudes of the wavefunctions.

effective method to increase the atomic interaction strength.

From Equation (5.4), it follows $\tau = 37$ ns for this avoided crossing. In this work, I use $\Delta t = 1$ μs, yielding $P_{\text{adia}} = 1 - 2.14 \times 10^{-12}$; the probability of adiabatic transfer is close to unity. In comparison, the first avoided crossing has an energy gap of 14 MHz. For the same electric field ramp of 0.2 V/cm, one finds a Landau-Zener time constant of $\tau = 4.1$ μs. To obtain $P_{\text{adia}} > 0.99$, $\Delta t > 20$ μs would be required. This is too long to neglect atomic motion during the electric field ramp.

The calculated wavefunctions of an atom undergoing the adiabatic state transformation are presented in Figure 5.4. For the S-like Stark state at 2.66 V/cm, the wavefunction closely resembles that of a spherically symmetric S state with a small admixture of parabolic (hydrogen-like) Stark states. The admixture causes the interference pattern at $z < 0$ that is clearly visible. After applying an electric field ramp to increase the field by 0.2 V/cm, the atom is transferred to the highly dipolar state at 2.86 V/cm. The final state is a superposition of different parabolic states, as oppose to a pure parabolic state. This is because for $|m_J| = 0.5$ the hydrogenic manifolds are missing the low angular momentum states, leading to modified spectra. The analysis shows that the final state carries the probabilities of (hydrogenic) parabolic states shown in Table 5.1. The final state at 2.86 V/cm has about 80% of $|n = 47, n_1 = 6, n_2 = 40, m = 0\rangle$ character.

The direction of the permanent atomic dipoles is fixed and identical with the direction of an externally applied electric field. From this fact, the anisotropic character of dipolar atom-pair kinetics can be demonstrated by choosing certain electric-field alignments relative to the experimental observation plane. Since the angular degrees of freedom of the atomic dipoles are fixed, the dynamics are restricted to the center-of-mass positions of the atoms. The fact that I have full control over the direction

Table 5.1: Parabolic states and corresponding probabilities contained in the target state.

$\|n, n_1, n_2, m\rangle$	Probability (%)
$\|47, 0, 46, 0\rangle$	0.874
$\|47, 1, 45, 0\rangle$	0.989
$\|47, 2, 44, 0\rangle$	1.188
$\|47, 3, 43, 0\rangle$	1.543
$\|47, 4, 42, 0\rangle$	2.414
$\|47, 5, 41, 0\rangle$	5.953
$\|47, 6, 40, 0\rangle$	79.656
$\|47, 7, 39, 0\rangle$	0.468
$\|47, 8, 38, 0\rangle$	0.004
$\|47, 9, 37, 0\rangle$	0.026
$\|47, 10, 36, 0\rangle$	0.077

of the atomic dipoles is critical in the measurement of the anisotropy of the dipolar atom-pair kinetics.

To estimate the density advantage afforded by the adiabatic state-switching method, I calculate the blockade radii for atoms in the selected dipolar state and for van der Waals-interacting $50S_{1/2}$ atoms, for a laser excitation bandwidth of 1 MHz. The density advantage is then given by the third power of the ratio of these blockade radii. For this experiment the adiabatic state transformation allows for a density increase of up to a factor of 40 over the case of direct laser excitation of the dipolar atoms. Incidentally, the dipolar state also lacks oscillator strength with low-lying atomic levels; this would make the direct laser excitation of a dense dipolar atom sample even more difficult. Therefore, the adiabatic preparation method is critical for the measurement of dipolar atom-pair kinetics.

5.3 Experimental setup

The experimental setup and the timing sequence of the experiment are shown in Figure 5.5. Cold ^{85}Rb atoms in the $5S_{1/2}$ state undergo two-photon Rydberg exci-

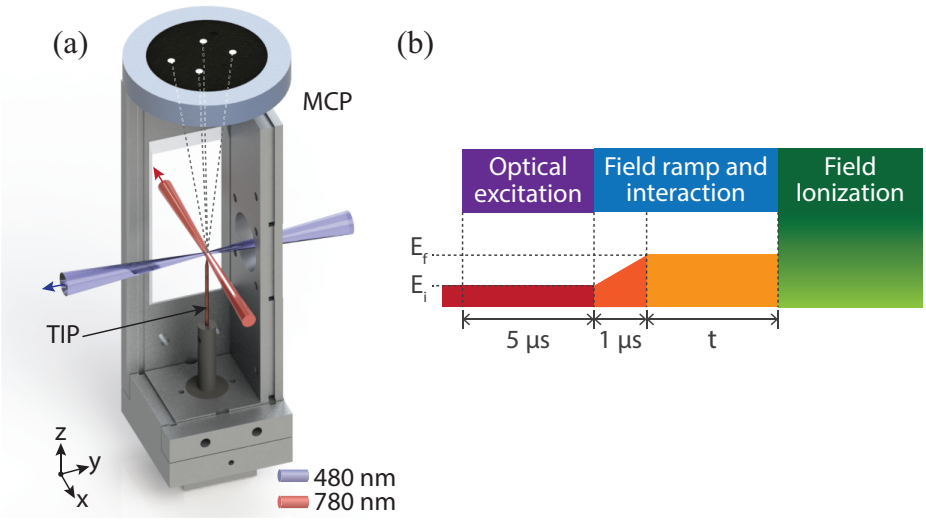

Figure 5.5: Experimental set-up and timing sequence. (a) Experimental set-up. (b) Timing sequence.

tation into the $50S_{1/2}$-like state by simultaneously applying 780- and 480-nm laser pulses, each with a duration of 5 μs. The lasers are $\approx$1 GHz red-detuned from the $5P_{3/2}$ intermediate state. The 780-nm beam propagates along the x-direction [see Figure 5.5(a)] and has a Gaussian beam parameter of $w_0 \approx 70$ μm. The 780-nm beam is focused to have a smaller size than that is used in Chapter IV in order to reduce the effect of electric field inhomogeneity. The 480-nm beam propagates in the xy plane, forms an angle of approximately 70° with the 780-nm beam, and has $w_0 \approx 8$ μm. The excitation region is about 300 μm above the TIP. For this distance, the magnification is measured to be $200 \pm 10\%$. The number of Rydberg excitations is on the order of ten per sample.

As mentioned in Section 5.2, after the initial excitation into the $50S_{1/2}$-like state at $E_\mathrm{i} = 2.66$ V/cm, the atoms are adiabatically transferred into the dipolar target state by linearly increasing the electric field by 0.2 V/cm within 1 μs. The electric field sweep is controlled using an arbitrary waveform generator (Agilent 33521A) which outputs a linear ramp voltage.

The sweep duration is slow enough that the adiabatic transfer from the $50S_{1/2}$-like

into the dipolar state has an efficiency very close to unity. The sweep duration is also short enough that during the adiabatic transfer the atoms do not move significantly. Hence, the state switching is practically instantaneous with respect to the center-of-mass motion of the atoms. After the switch, the electric field is kept constant at $E_{\mathrm{f}} = 2.86$ V/cm for the duration of the interaction time, t. I study the atom kinetics that follow from the dipolar force in Equation (5.2) as a function of t.

I perform atom imaging and measure the spatial correlation between Rydberg atoms under two configurations. In the first case, the direction of the atomic dipoles is transverse to the plane within which the atoms are mainly prepared, showing the kinetics of dipoles that are initialized side-by-side. In this case, the interactions are repulsive and azimuthally symmetric about the axis of the ion imaging system. The pair-correlation functions reveal rapid atom-pair repulsion with an apparent transient shock front developing during the expansion and disorder-induced heating. In the second case, the atomic dipoles are prepared parallel to the observation plane in order to capture the kinetics of atomic dipoles that are aligned anywhere between side-by-side and in-line with each other. For this case, the dipolar interatomic force varies between repulsive and attractive as a function of angle. This leads to dramatic changes of the measured Rydberg-atom pair-correlation images. The images develop a characteristic dumbbell-shaped form, which visually demonstrates the angular dependence of the microscopic dipolar force.

5.4 Electric field perpendicular to the detection plane

When the applied electric field is perpendicular to the detection (xy) plane, the atomic dipoles point in the z-direction, as shown in Figure 5.6(b). Since the excitation blockade radius is on the order of the diameter of the 480-nm excitation beam, most

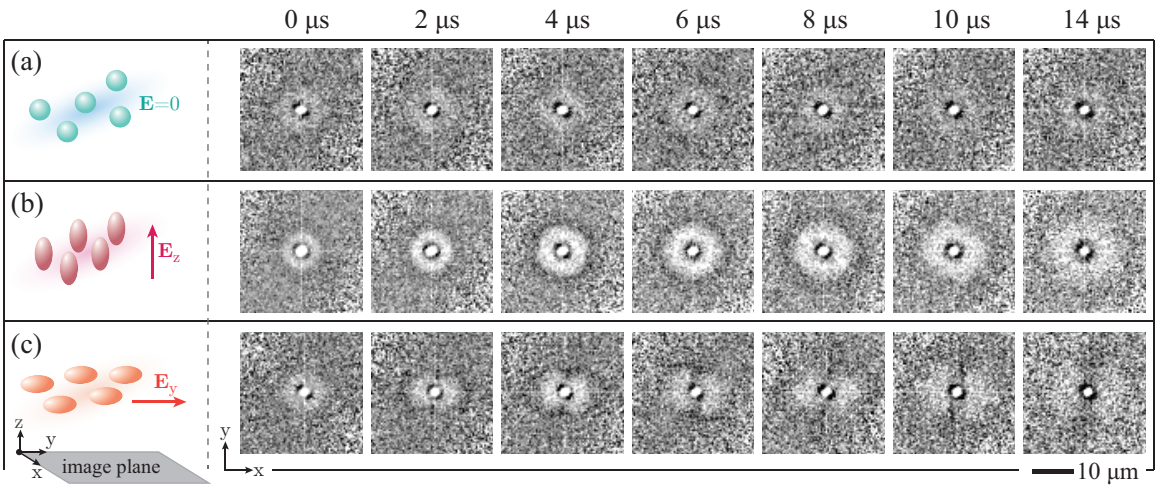

Figure 5.6: The illustrations on the left show the electric-field and dipolar alignments relative to the object/image planes for the experimental pair-correlation images on the right for the indicated selected wait times. The linear gray scale ranges from 0.4 (white) to 1.5 (black), where values of 1, <1, and >1 indicate no correlation, anticorrelation, and positive correlation, respectively. (a) Zero field where atoms undergo weak van der Waals interaction. (b) Applied electric field in z direction where the atomic dipoles are aligned along z, perpendicular to the image (xy) plane. Binary interactions are azimuthally symmetric about z and primarily repulsive, leading to images that are without angular structure and indicative of strong repulsion. (c) Applied electric field in y direction where the atomic dipoles are aligned along y, in plane with the image plane. Binary interactions are not azimuthally symmetric about z and are mixed attractive / repulsive, leading to anisotropic images indicative of repulsion along x and strong attraction along y.

dipole-dipole-interacting atom pairs are at $\Theta \approx \pi/2$ [see Equation (5.2)]. Hence, for the vast majority of atom pairs the dipole force is repulsive, with $F_{\mathrm{R}} \approx 3p^2/R^4$, and azimuthally symmetric about the line of sight.

The pair correlation images presented in Figure 5.6(b) are azimuthally symmetric at all times. With increasing interaction time, the (projected) radius of the region that is largely devoid of pair-correlation events increases, reflecting an increase of the interatomic separation due to repulsive dipole-dipole interactions. The expansion due to dipole-dipole interaction is considerably faster than that due to repulsive van der Waals interactions between $50S_{1/2}$ atoms at zero electric field, shown in Figure 5.6(a). The van der Waals interaction does not cause any significant expansion over timescale of Figure 5.6. In Chapter IV, it was found that even atoms in the $70S_{1/2}$ state,

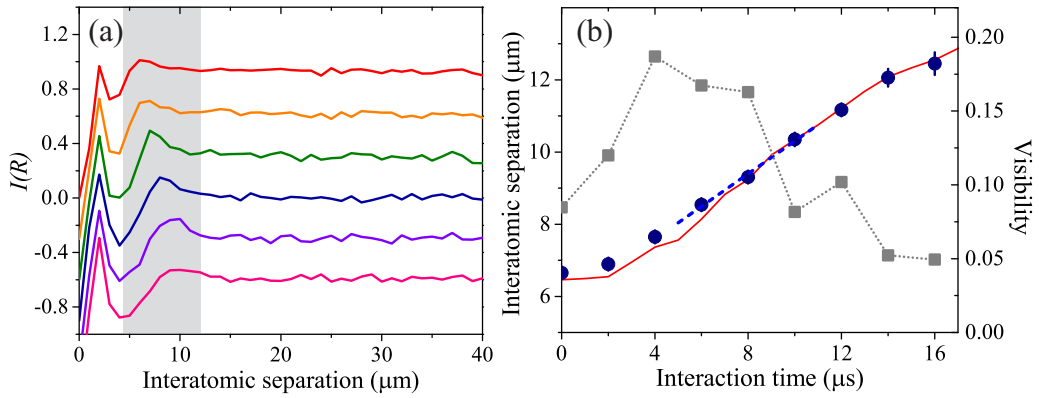

Figure 5.7: I(R) curves and trajectory measurement. (a) Angular integrals $I(R)$ of the pair correlation images in Figure 5.6(b) at wait times (from top to bottom): 0 μs, 2 μs, 4 μs, 6 μs, 8 μs, and 10 μs. The y axis is for the 0 μs curve; for clarity, the other curves are shifted down in equidistant steps of 0.3. The most probable separation $R_{\rm p}(t)$ is obtained from local parabolic fits to the maxima observed within the shaded region. (b) Interatomic separations $R_{\rm p}(t)$ between Rydberg-atom pairs as a function of interaction time (left axis), obtained from the peak positions in the $I(R)$ curves, from experiment (blue circles) and simulation (red line). The blue dashed line shows a linear fit to the experimental data between 6 μs to 10 μs. The gray squares show the visibility of the experimental pair correlation enhancement (right axis).

which interact about 50 times more strongly than atoms in the $50S_{1/2}$ state (present case), exhibit significant repulsion effects only after about 30 μs. Hence, a cursory comparison of the pair correlation data in Figure 5.6(a) and (b) already shows that the interaction between the dipolar atoms must be 1 to 2 orders of magnitude stronger than the interaction between the non-polar, van der Waals-interacting atoms.

The angular integrals $I(R)$ of the pair correlation images from Figure 5.6(b) are shown in Figure 5.7(a). The most probable separation between Rydberg-atom pairs, $R_{\rm p}(t)$, is determined by local parabolic fits to $I(R)$ in the vicinity of the peaks found within the shaded region in Figure 5.7(a). The blue circles in Figure 5.7(b) show the resulting $R_{\rm p}(t)$ values that represent the most probable radial atom-pair trajectory projected into the xy plane. The atom pairs are initially prepared at a preferential separation $R_{\rm p}(0) = 6.7 \pm 0.7$ μm, controlled by the excitation-laser detuning and the atomic interaction strength before the adiabatic state transformation. The large positive acceleration observed subsequent to the state transformation is due to the strong

repulsive dipole-dipole interaction that occurs for angles $\Theta \approx \pi/2$. The acceleration diminishes and changes sign from positive to negative at an interaction time near 8 μs, where $d^2R_\mathrm{p}(t)/dt^2 \sim 0$.

To verify that the observed rapid expansion in the xy plane is consistent with the known permanent electric dipole moment of the atoms after adiabatic transformation, the interaction coefficient C_3 is extracted using conservation of energy between interaction times of 0 and t:

$$\frac{C_3}{R_\mathrm{p}(0)^3} = \frac{C_3}{R_\mathrm{p}(t)^3} + \frac{1}{2}\mu V(t)^2 \quad , \tag{5.5}$$

where μ and $V(t)$ are the reduced mass of a pair of ^{85}Rb atoms and the relative pair velocity, respectively. Here, $t = 8$ μs is chosen because the atom pairs have an approximately constant velocity at that time, which can be extracted well from a local linear fit within the range $6 \leqslant t \leqslant 10$ μs, indicated by the blue dashed line in Figure 5.7(b). At this interaction time, $V(8\ \mu\mathrm{s}) = 0.45 \pm 0.06$ m/s and $R_\mathrm{p}(8\ \mu\mathrm{s}) = 9.3 \pm 0.9$ μm, where the uncertainties include the statistical fit and the magnification uncertainties. With $R_\mathrm{p}(0) = 6.7 \pm 0.7$ μm from above, the resulting C_3 value becomes $(3.3 \pm 1.8) \times 10^{-42}$ J m^3. This value agrees with the calculated C_3 value, $p^2/(4\pi\epsilon_0) = 3.72 \times 10^{-42}$ J m^3, implying that the interacting entities are individual atoms and not superatoms, as has been predicted in Reference [67] and experimentally observed for van-der-Waals-interacting Rydberg excitations in Chapter IV.

5.4.1 Disorder-induced heating

In Figure 5.7(b) it is evident from the experimental data (circles) and the result of a semi-classical simulation (red line) that the acceleration is negative for $t \gtrsim 10$ μs. The late-time deceleration appears to be due to repulsion from initially farther-away atoms, indicating many-body dynamics that involve more than two atoms. A

related conclusion can be drawn from considering the visibility of the pair-correlation enhancement as a function of time, calculated from the $I(R)$ curves in Figure 5.7(a) as

$$\text{Visibility} = \frac{I(R_\text{p}(t)) - \langle I \rangle}{\langle I \rangle} \quad , \tag{5.6}$$

where the asymptotic values $\langle I \rangle$ are obtained by averaging $I(R)$ curves over the range $R > 15$ μm. The visibility values are shown as gray squares in Figure 5.7(b). The visibility rapidly increases at early times, $t \lesssim 4$ μs, and passes through a broad maximum between 4 and 8 μs. Hence, the significance of the pair correlation enhancement at R_p, equivalent to the degree of short-range order, and the kinetic energy of the sample, equivalent to the slope in $R_\text{p}(t)$, both become maximal approximately at the same time. These evidences are reminiscent of disorder-induced heating, which has been observed in the strongly-coupled ion component of an ultracold plasma [104, 105]. In both cases, particles initially repel each other due to dominant nearest-neighbor forces before encountering repulsive forces from initially more distant particles. At $t \gtrsim 10$ μs the correlation enhancement disappears, which is in part due to the initial thermal atom velocity.

5.4.2 Coupling parameter

In an ultracold plasma system, the Coulomb coupling parameter defined as the ratio between the Coulomb potential energy and the thermal energy is used to determine the coupling condition of the system. The spatial correlation characteristic starts to appear at $\Gamma > 1$ [105]. In this work, the interaction strength is comparable to a strong Coulomb interaction. By replacing the Coulomb potential energy with the initial dipole-dipole potential energy in Equation (5.1), the coupling parameter of the

dipolar system is given by

$$\Gamma = \frac{p^2/\left(4\pi\epsilon_0 R^3\right)}{\left(k_{\mathrm{B}}T\right)} \quad , \tag{5.7}$$

and is equal to 9 in this case at the MOT temperature 100 μK, which is sufficiently large that the system may indeed develop (transient) short-range order.

Note that apparent analogies between dense dipolar Rydberg-atom ensembles and strongly-coupled plasmas are limited due to the different nature of the forces involved (dipole-dipole versus Coulomb), the different radial and angular characteristics of the forces, and the different system sizes (only about ten particles in this work versus $10^5 - 10^7$ ions in an ultracold plasma system).

5.5 Electric field parallel to the detection plane

To exhibit the anisotropic atom-pair kinetics that follow from Equation (5.2), the experimental setup must be modified such that the shared azimuthal symmetry between the microscopic force law and the imaging system is removed. In the setup this is easily possible by application of an external electric field in the xy plane [Figure 5.5(a)]. The adiabatic passage of the atoms through the avoided crossing is performed as before. The measured pair correlation images shown in the following amount to a first direct observation of dipolar, anisotropic atom-pair kinetics.

When the electric field is applied along the y axis, the atomic permanent electric dipole moments are oriented along y. The angular dependence of the dipole force can be observed within the xy plane, encompassing maximally-repulsive interactions ($\Theta = \pi/2$) and maximally-attractive interactions ($\Theta = 0$), as well as all intermediate cases. The interaction then leads to the characteristic anisotropic patterns in the pair correlation images shown in Figure 5.6(c).

The angular force in Equation (5.2) is maximal with $F_\Theta = 3p^2/R^4$ at $\Theta = \pi/4$

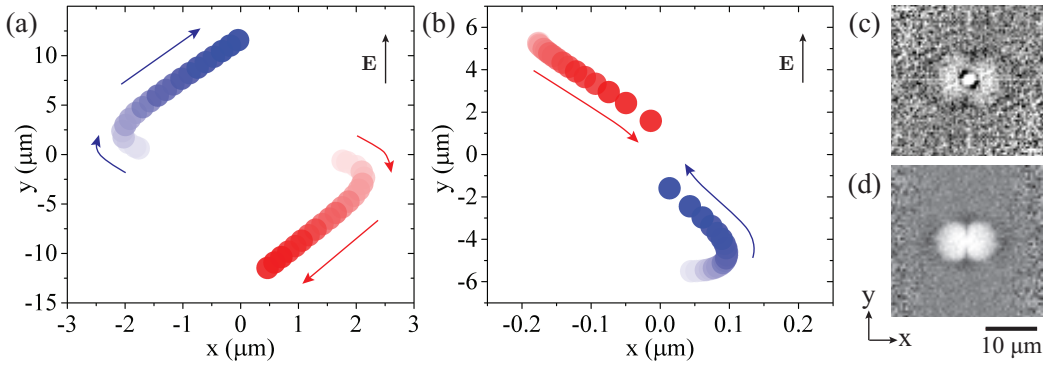

Figure 5.8: Positions of two interacting dipoles from the interaction time $t = 0$ (lightest circle) to $t = 20$ μs (darkest circle). The arrows show the trajectory of the dipoles obtained from a simulation. (a) Two dipoles initially aligned almost perpendicular to the electric field direction. The repulsive force dominates. The dipoles repel each other and turn around due to the angular dependence of the force. (b) Two dipoles initially aligned almost parallel to the electric field direction. The attractive force dominates and the dipoles come closer to each other. Due to the combination of radial and angular forces, the atom pairs become funneled into narrow conical sections at the poles. This leads to characteristic pair correlation images as shown in (c) (from the experiment) and (d) (from the simulation). The images in (c) and (d) are obtained for an interaction time $t = 4$ μs.

and $3\pi/4$, and zero at $\Theta = 0$, $\pi/2$ and π. Atom pairs initially positioned at $\Theta \approx \pi/2$ will keep repelling each other, while being diverted towards the poles by the angular force [Figure 5.8(a)]. Within the experimental uncertainty, the most probable pair separations $R_{\mathrm{p}}(t)$ in Figure 5.6(b) along any direction in the xy plane and in Figure 5.6(c) along the x direction are the same. This is expected because all these cases correspond to $\Theta = \pi/2$ in Equation (5.2).

The angular force always points towards the "poles" [$\Theta = 0$ or π, see Figure 5.1(b)], leading to an accumulation of atom pairs lined approximately along the electric-field direction (the same direction as $\mathbf{p}$). These atom pairs are then pulled close to each other due to the radial component of the force which is attractive for $\Theta \leqslant 55^\circ$ and $\Theta \geqslant 125^\circ$ [Figure 5.8(b)]. These atom pairs form the prominent vertical dark strip across the center of the pair correlation images at interaction times $\gtrsim 4$ μs in Figure 5.6(c). The "funneling effect" pointing towards the poles eventually leads to dumbbell-shaped pair-correlation images that are void of signal in a volume extending along x and that possesses an enhanced signal along y. These characteristics are

seen the experiment [Figure 5.8(c)] and in the simulations [Figure 5.8(d)]. The small deviation of the enhancement cones in Figure 5.6(c) from the y direction is attributed to a slight deviation of the electrode arrangement from perfect symmetry.

Atoms pulled close to each other along the polar direction (y) will likely undergo Penning-ionizing collisions [100], when the interatomic separation R drops below about 0.5 μm ($2.1 \times 2\ n_{\rm eff}^2\ a_0$). This distance is below the image resolution and is not directly observed in the experiment. It is, however, noticed that the amount of signal within the enhancement cones near $\Theta = 0$ and $\Theta = \pi$ in Figure 5.6(c) plateaus at $t \gtrsim 4$ μs and eventually drops. This observation is consistent with atom-pair loss within the polar cones due to Penning ionization.

5.6 Summary

In summary, an adiabatic state transformation method has been employed to prepare samples of Rydberg atoms with large permanent electric dipole moments. This preparation method circumvents density limitations set by the Rydberg excitation blockade mechanism, which is frequently encountered in such systems. I have been able to study the strength and angular properties of the dipole force between pairs of individual atoms. The results have included a determination of the dipolar dispersion coefficient, C_3. The measured pair correlation images portray the anisotropic character of dipolar atom-pair kinetics in a forceful, intuitive manner. Quantitative results of a model agree well with the experimental observations. I also have observed dynamics reminiscent of disorder-induced heating, similar to what has been seen elsewhere in strongly-coupled plasmas.

CHAPTER VI

Control of spatial correlations between Rydberg excitations using rotary echo

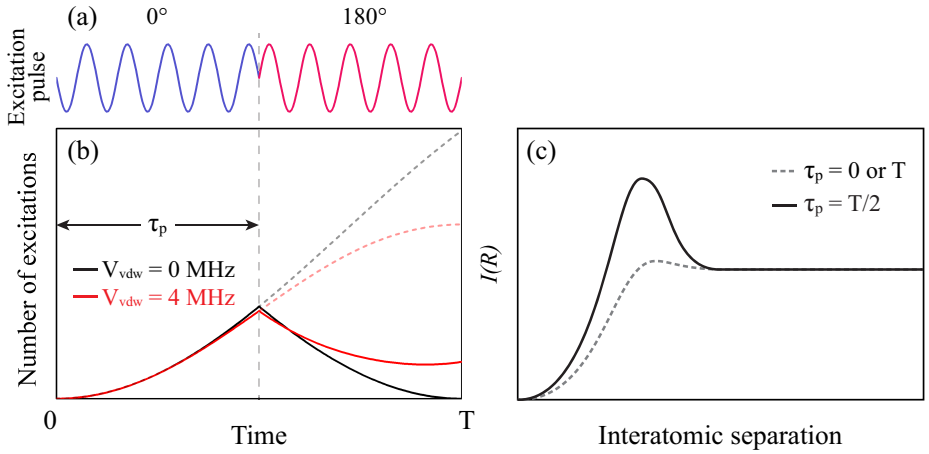

Figure 6.1: (a) An optical excitation pulse with a duration T for Rydberg-atom production. The phase of the pulse is changed by 180° at time $\tau_{\rm p} = T/2$. (b) Number of excitations (including individual and pair excitation) versus time before and after phase inversion of the optical pulse. At the end of the pulse, the on-resonant, uncorrelated atoms ($V_{\rm vdW} = 0$) return to the ground state, leaving the off-resonant atoms (in this plot I select $V_{\rm vdW} = 4$ MHz) in the Rydberg state. Dashed lines indicate the number of excitations when there is no phase inversion. (c) Sketch of the radial pair correlation function when $\tau_{\rm p} = 0$ or T (no echo) and $\tau_{\rm p} = T/2$ (echo). The correlation enhancement peak of the echo case is expected to be stronger than the no-echo case because in the former case the system contains fewer uncorrelated atoms than in the latter one.

In this chapter, I present a rotary echo technique to control Rydberg-atom correlations, as proposed by Wüster et. al. [36]. The rotary echo is performed by modulating the optical phase of the Rydberg excitation laser to eliminate the uncorrelated atoms after the excitation. As found previously in simulations [33] and in experiments [34, 35], a rotary Rydberg-atom excitation echo occurs when the sign of the

Rabi frequency Ω of a Rydberg transition is inverted at the middle of an on-resonant excitation pulse. This is accomplished by inverting the phase of the optical excitation pulse, as demonstrated in Figure 6.1(a). At the end of the excitation pulse, the uncorrelated atoms return to ground state while the spatially correlated atoms remain in the Rydberg state [Figure 6.1(b)]. It was predicted in Reference [36] that a rotary-echo excitation pulse would lead to an enhancement of the Rydberg pair correlation function at a separation near the blockade radius, as illustrated in Figure 6.1(c).

I employ a rotary-echo sequence to excite cold ^{85}Rb atoms into Rydberg states. I explore the effects of the echo on Rydberg-atom spatial correlations and the excitation-number statistics. This work demonstrates that a rotary-echo sequence substantially enhances spatial correlations between the Rydberg excitations. In addition, it is observed that the rotary-echo-induced features strongly depend on the laser detuning. Particularly, it is seen that the rotary echo gives rise to strong spatial correlations when the excitation lasers are on-resonant, while in certain off-resonant cases the echo causes a complementary effect, namely the destruction of spatial correlations that would otherwise be present.

6.1 Experimental Setup

The energy level diagram is presented in Figure 6.2(a). Cold ^{85}Rb atoms in the $5S_{1/2}$ state are excited to the $70S_{1/2}$ state via two-photon excitation using 780- and 480-nm laser pulses that overlap in time and have a duration $T = 250$ ns. The 780-nm laser has a Gaussian beam parameter $w_0 = 750$ μm and a power of 600 μW. The 480-nm laser has a $w_0 \approx 8$ μm and a power of 30 mW. The detuning from the intermediate state $5P_{3/2}$ is $\delta = 2\pi \times 131$ MHz. At the beam center, the Rabi frequencies of the lower and upper transitions are $\Omega_1 = 2\pi \times 20$ MHz and $\Omega_2 = 2\pi \times 21$ MHz, respectively.

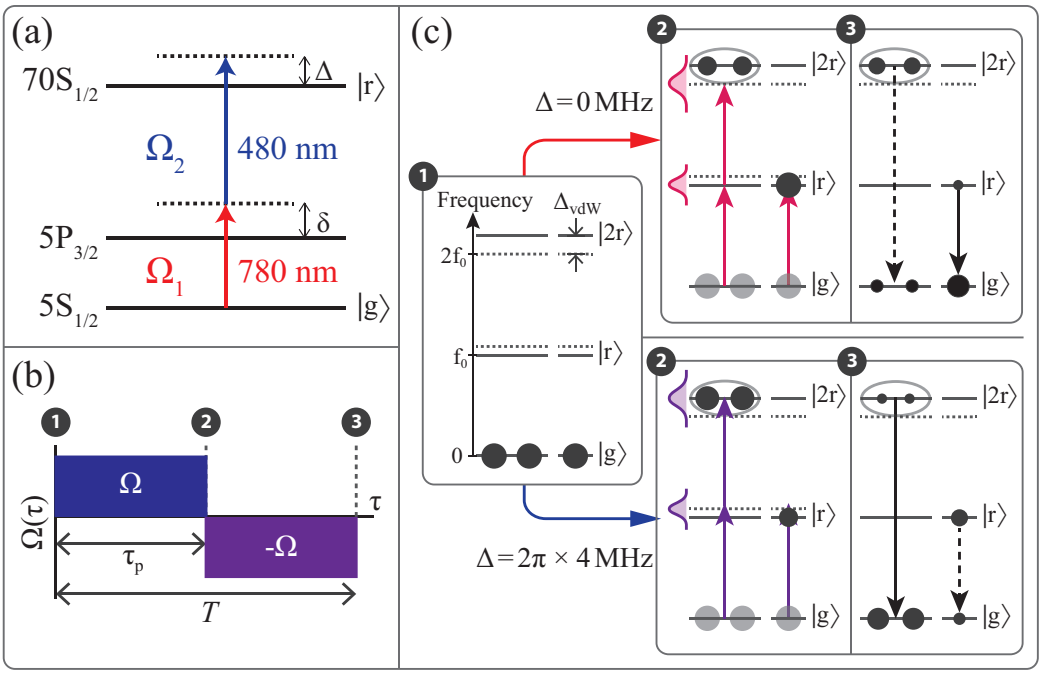

Figure 6.2: (a) Two-photon excitation of a single ^{85}Rb Rydberg atom (see text for more details). (b) Echo sequence during excitation. I apply an excitation pulse of duration $T = 250$ ns. The two-photon Rabi frequency is switched from Ω to $-\Omega$ (in the field picture) at time τ_p. The time labels 1, 2, and 3 above the timing sequence correspond with the diagrams in (c). (c) Internal dynamics of atoms during the echo sequence. The frequency to excite one Rydberg atom $|r\rangle$ without interactions is f_0 (red arrow). The frequency leading to direct excitation of two Rydberg atoms (state $|2r\rangle$) is $f_0 + \Delta_{vdW}/2$ (purple arrow). Because of the excitation bandwidth, in either case I excite a mix of isolated Rydberg atoms in state $|r\rangle$ and Rydberg-atom pairs in state $|2r\rangle$. The circle sizes in the level diagrams illustrate the populations of van-der-Waals-interacting atom pairs (left pair of circles) and of isolated atoms (right circle) at times 1, 2 and 3 for the cases $\Delta = 0$ and $\Delta = 2\pi \times 4$ MHz.

This leads to a two-photon (one 780 nm and one 480 nm photon) Rabi frequency for single-atom excitation at the two-photon resonance ($\Delta = 0$) of $\Omega = \Omega_1\Omega_2/(2\delta) = 2\pi \times 1.67$ MHz. In the case of substantial detuning $\Delta > 0$, Rydberg atoms can be directly excited in pairs or sequentially excited close to Rydberg atoms that are already present in the sample (so called facilitated excitation). In any case, the excess photon energy introduced by the laser detuning matches the van der Waals interaction potential. When $\Delta = 2\pi \times 4$ MHz, as used in Chapter IV, the Rabi frequency for the simultaneous pair excitation is $\Omega_{pair} = \Omega^2/(2\Delta) = 2\pi \times 0.35$ MHz. Note that, in order to avoid dephasing due to atomic motion, here I use an excitation pulse duration of only 250 ns. This is very short in comparison with the experiments mentioned in

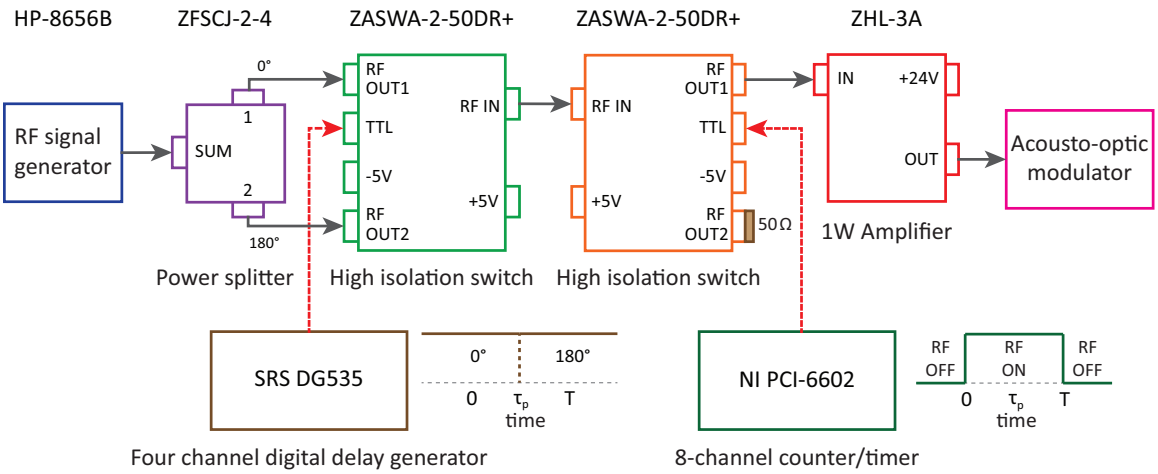

Figure 6.3: Diagram of RF phase and pulse controller for echo experiment. See text for details.

Chapters IV and V, where the excitation pulse duration is 5 μs.

To implement the rotary echo, I invert the optical phase of the 480-nm laser pulse at time τ_{p}, as shown in Figure 6.2(b). This can be performed by inverting the phase of the radio frequency (RF) signal that is applied to the acousto-optic modulator (AOM) that determines the optical phase of the 480-nm laser pulse. The diagram of RF phase and pulse controller is shown in Figure 6.3. The RF is generated from a RF synthesizer (HP-8656B). I use a power splitter (ZFSCJ-2-4+) to provide two RF signals with 180°phase difference. I control the time τ_{p} and the pulse duration of the excitation beam by using two high isolation switches (ZASWA-2-50DR+). The RF signal is then amplified by using a 1 W amplifier (ZHL-3A) before the AOM.

The resulting optical pulses obtained from a photodiode are presented in Figure. 6.4(a). A notch occurs at τ_{p} of each pulse due to an imperfection of RF phase inversion inside the AOM (at a switching time, rising and falling time of each RF pulse is not zero so they overlap and cause this interference).

After the excitation pulse, a high voltage is applied to the TIP to ionize the Rydberg atoms, allowing their positions to be detected using the MCP (as explained

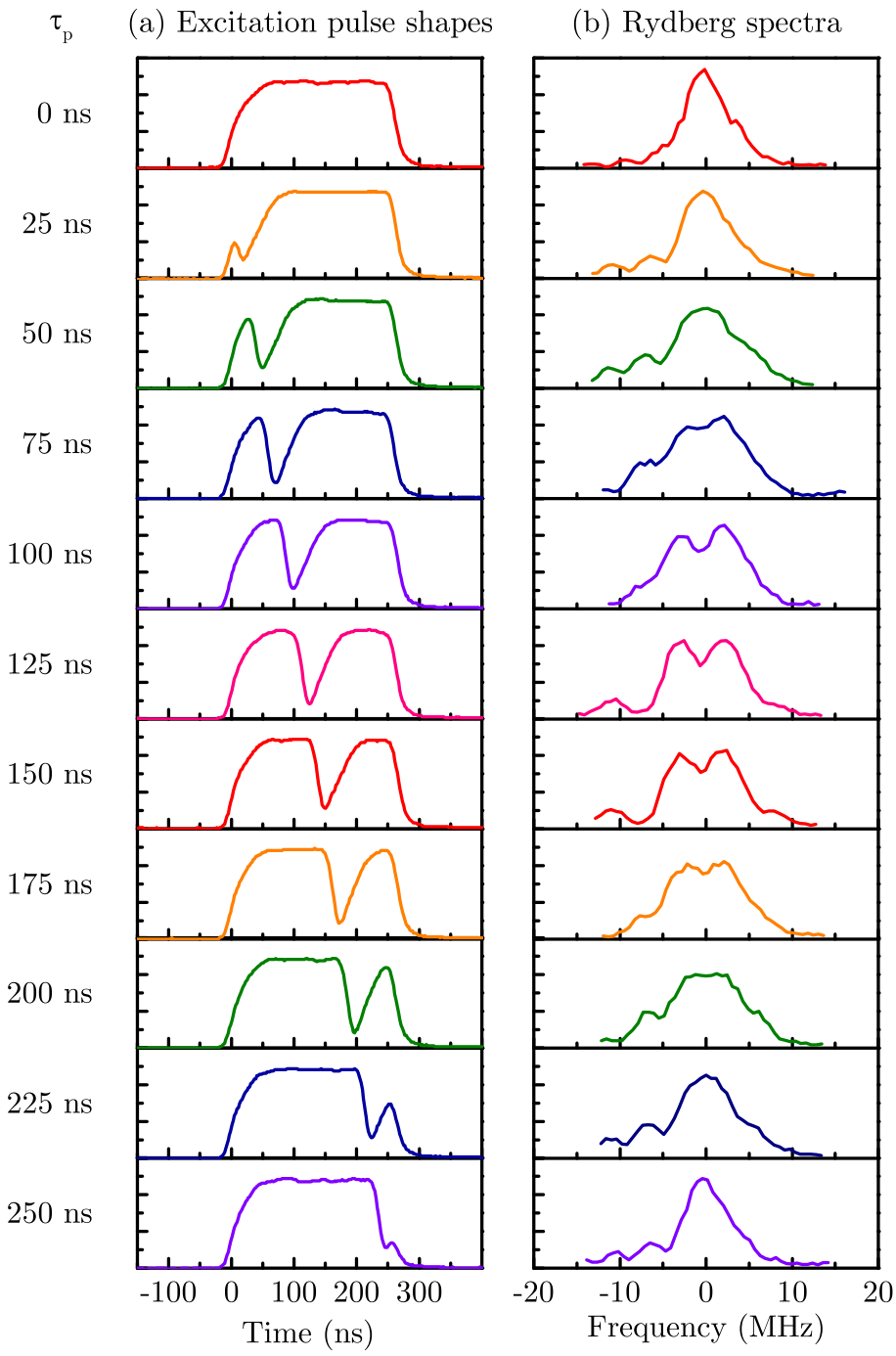

Figure 6.4: (a) Excitation pulse shapes for various τ_p where the y axis is intensity in arbitrary units. (b) Rydberg excitation spectra where the y axis is the number of Rydberg excitations, ranging between 0 and 6.

in Chapter III). The excitation region is 470 μm above the TIP, which provides a magnification of 150. For each detuning Δ and flip time τ_p I take 10,000 images and choose the 5,000 images with the highest numbers of excitations to calculate pair correlation images. Angular integrals of the pair correlation images yield the radial pair correlation functions $I(R)$. Quantitative information on the echo effect is then extracted from the $I(R)$.

6.2 Echo spectra

To verify the presence of a rotary echo in the experiment, I measure Rydberg excitation spectra when τ_{p} is ranging from 0 to 250 nm with a step size of 25 ns, as shown in Figure 6.4(b). The peak position in the echo-free spectrum ($\tau_{\mathrm{p}} = 0$) marks the on-resonant transition $\Delta = 0$. The echo is most effective when $\tau_{\mathrm{p}} \approx 125$ ns. In this case, the spectra are broader and have a depression of detected Rydberg counts at $\Delta = 0$.

In Figure 6.4(b), the signal when $\tau_{\mathrm{p}} = 125$ ns does not drop to zero at $\Delta = 0$, as would be the case for a perfect echo, due to the following reasons. First, slightly off-resonantly excited atom pairs whose pair energies are shifted due to the van der Waals interactions do not undergo a perfect echo. Second, the spectrum is convolved with the profile of the shot-to-shot laser-frequency jitter. I have simulated the excitation spectra of atom pairs in a disordered atomic sample and convolved the results with a Gaussian profile to represent frequency jitter. Assuming a full-width-at-half-maximum (FWHM) of 3 to 4 MHz for the Gaussian profile and using the measured pulse shape, I obtain simulated spectra that are consistent with the experimentally observed ones (see Section 6.7).

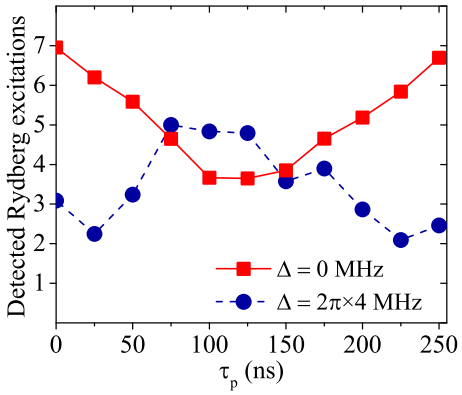

Figure 6.5: Number of detected Rydberg excitations as a function of phase flip time τ_{p} for $\Delta = 0$ (red squares) and $2\pi \times 4$ MHz (blue circles).

6.3 Echo visibility

The averaged number of detected Rydberg excitations obtained from 10,000 images is presented in Figure 6.5. The $\Delta = 0$ counts have a minimum when $\tau_{\mathrm{p}} = T/2 = 125$ ns, as expected for a rotary echo. The $\Delta = 2\pi \times 4$ MHz counts show a complementary effect with a maximum near $\tau_{\mathrm{p}} = T/2 = 125$ ns. I calculate the echo visibility [34, 35] given by

$$V_{\mathrm{echo}} = \frac{N(\tau_{\mathrm{p}} = 0) + N(\tau_{\mathrm{p}} = T) - 2N(\tau_{\mathrm{p}} = T/2)}{N(\tau_{\mathrm{p}} = 0) + N(\tau_{\mathrm{p}} = T) + 2N(\tau_{\mathrm{p}} = T/2)} \quad , \tag{6.1}$$

where $N(\tau_{\mathrm{p}})$ is the average number of Rydberg excitations detected using a phase-inversion time τ_{p}. The magnitude of the echo visibility $|V_{\mathrm{echo}}|$ ranges from 0 (no echo) to 1 (perfect echo) and represents a measure for the coherence of the excitation [34]. Here, $|V_{\mathrm{echo}}| = 0.303 \pm 0.004$ for $\Delta = 0$ MHz and $|V_{\mathrm{echo}}| = 0.267 \pm 0.005$ for $\Delta = 2\pi \times 4$ MHz. The value of $|V_{\mathrm{echo}}|$ is lowered by the aforementioned shot-to-shot laser frequency jitter and phase/shape imperfection of the excitation pulse. Atom-atom interactions can also lead to a reduction of $|V_{\mathrm{echo}}|$.

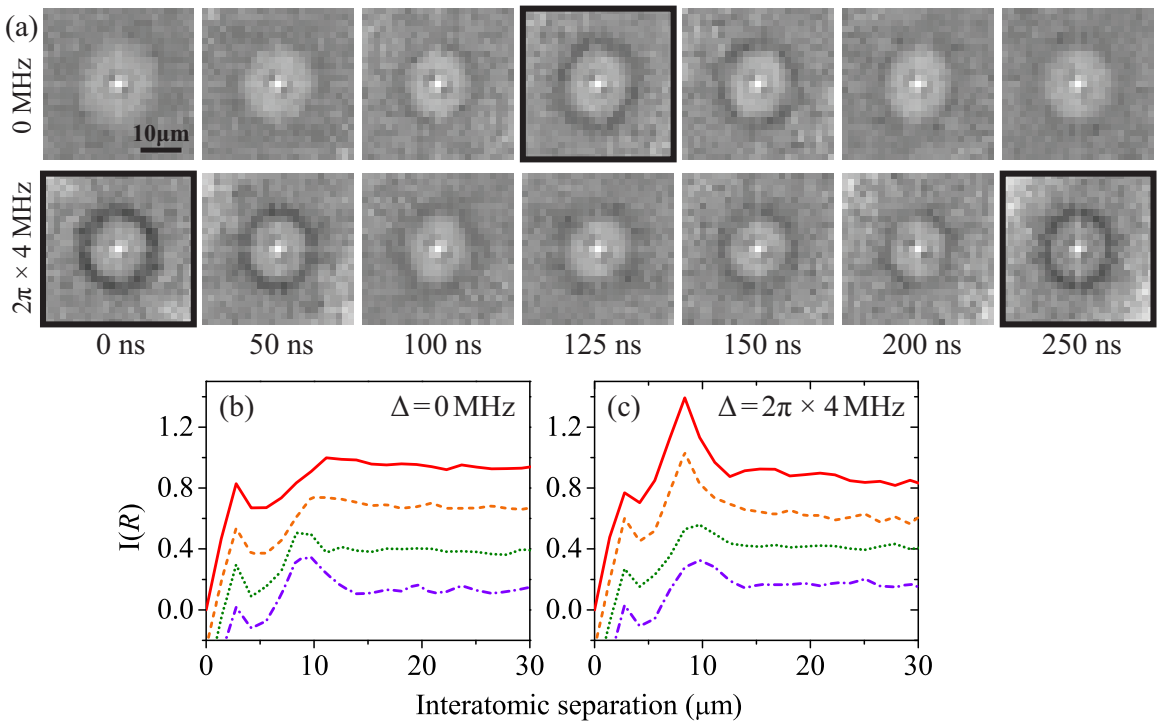

Figure 6.6: (a) Pair correlation images at selected τ_p for (top row) $\Delta = 0$ MHz and (bottom row) $\Delta = 2\pi \times 4$ MHz. The linear grayscale ranges from 0 (white) to 2 (black) where values of 1, <1, and >1 indicate no correlation, anticorrelation, and positive correlation, respectively. The bold borders indicate pair correlation images obtained from systems that contain many pair-excitations. The 3 to 4 μm pattern near the center of each image is an artifact (see text). (b) Angular integrals $I(R)$ of the pair correlation images in (a) for $\Delta = 0$ MHz for $\tau_p = 0$, 50, 100, and 125 ns (top to bottom). The vertical axis is for the 0 ns curve. The other curves are shifted down in equidistant intervals of 0.3 for clarity. (c) Same as (b), but for $\Delta = 2\pi \times 4$ MHz.

6.4 Echo pair correlation images

I now turn to describing the effect of the echo sequence on the spatial pair-correlation functions. Pair correlation images measured for $\Delta = 0$ MHz are shown in the top row of Figure 6.6(a). When τ_p is increased from 0 or decreased from T towards $T/2$, the pair correlation image clearly develops an enhancement ring with a radius of about 10 μm. The enhancement ring reaches maximal contrast for $\tau_p \approx T/2 = 125$ ns as can be seen by visual inspection of the images in Figure 6.6(a). A complementary effect occurs for the case $\Delta = 2\pi \times 4$ MHz [bottom row of Figure 6.6(a)]. The pair correlation is maximally enhanced at a radius near 10 μm when $\tau_p \approx 0$ or T,

while it becomes washed out when $\tau_p \approx T/2$. The pair-correlation signal at very short distances (about 3 μm) is an artifact caused by ion feedback from the TIP; field electrons hitting the TIP release a secondary ion that impinges on the MCP close to the primary (Rb^+) ion [106]. In the quantitative analysis below, I employ the angular integrals $I(R)$ of the pair correlation images. I show the $I(R)$ curves in Figure 6.6(b) for the case $\Delta = 0$, and in Figure 6.6(c) for the case $\Delta = 2\pi \times 4$ MHz.

In the explanation of the pair correlation data and the strength of the correlation enhancement, I concentrate on the "echo case" $\tau_p \approx T/2$ and refer to Fig. 6.2. The two-photon Rabi frequency ($\Omega = 2\pi \times 1.67$ MHz) is high enough that many excitation domains within the sample carry one Rydberg excitation (state $|r\rangle$) after the first phase of the excitation pulse [i.e., at time τ_p; isolated atom in Fig. 6.2(c)]. However, due to the bandwidth of the excitation pulse, some excitation domains become populated with a Rydberg-excitation pair (state $|2r\rangle$). The doubly-excited domains have an energy level shift Δ_{vdW} from the drive field due to the van der Waals interaction (atom pairs in Fig. 6.2(c)). The atom populations after flipping the phase and completing the excitation pulse are illustrated in Fig. 6.2(c), at time labels 3. For the case $\Delta = 0$, domains in the state $|r\rangle$ are de-excited back to the $|g\rangle$-state. However, the domains in excited state $|2r\rangle$ are off-resonant, leaving them with some probability in $|2r\rangle$ after completion of the echo sequence. In essence, after the sequence I expect to find a relative over-abundance of atoms separated by a distance near the blockade radius. The experimental data support this scenario. A complementary behavior occurs in the case $\Delta = 2\pi \times 4$ MHz, with the roles of singly- and doubly-excited domains reversed.

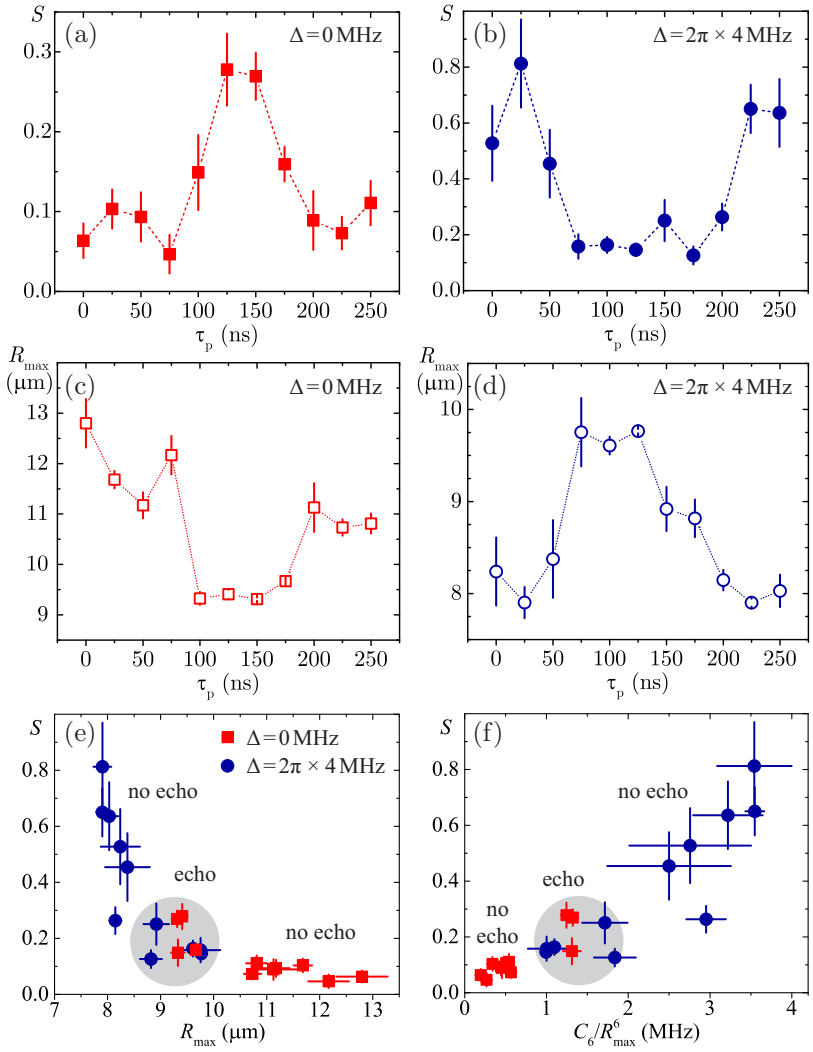

Figure 6.7: (a,b) Pair correlation enhancement, S and (c,d) $R_{\max}$. as a function of $\tau_{\rm p}$. (e) S versus $R_{\max}$. (f) S versus $C_6/R^6_{\max}$. In the plots (e) and (f), I identify the cases of excitation with and without echo for both $\Delta = 0$ and $2\pi \times 4$ MHz.

6.5 Strength of the correlation enhancement

For a more quantitative analysis, I extract from the $I(R)$ curves the enhanced peak values $I_{\max}$ and radii $R_{\max}$ of maximal correlation enhancement, determined by local parabolic fits to the maxima near $R = 10$ μm. Close inspection of the $I(R)$ curves in Figures 6.6(b,c) shows that the FWHM of the enhancement peak decreases when the $I_{\max}$ increases. I calculate S, the strength of the correlation enhancement of a pair

correlation function, as:

$$S = \frac{I_{\max} - \langle I \rangle}{\langle I \rangle} \quad . \tag{6.2}$$

I determine the asymptotic values $\langle I \rangle$ by taking the average of $I(R)$ over the range 20 μm $< R <$ 60 μm. Figure 6.7 shows the dependence of the pair enhancements S and the radii $R_{\max}$ on $\tau_{\rm p}$. As anticipated from Figure 6.6, the curves in Figure 6.7(a) and Figure 6.7(b) exhibit pronounced maxima at the "echo case" $\tau_{\rm p} \approx T/2$, when $\Delta = 0$, and at the "no-echo case" $\tau_{\rm p} \approx 0$ and T, when $\Delta = 2\pi \times 4$ MHz.

Figures 6.7(c) and (d) reveal a dependence of $R_{\max}$ on $\tau_{\rm p}$. In particular, it is seen in Figures 6.6(b) and 6.7(c) that $R_{\max}$ for $\tau_{\rm p} = T/2$ drops to near or slightly below the blockade radius seen for $\tau_{\rm p} \approx 0$. This is because the Fourier width of the excitation pulse at the time instant of the phase flip for the $\tau_{\rm p} \approx T/2$ case is twice as large as the Fourier width for the $\tau_{\rm p} \approx 0$ case at the end of the entire excitation pulse (8 MHz vs 4 MHz, respectively). Hence, the relevant blockade radius in the $\tau_{\rm p} \approx T/2$ case is smaller than that in the $\tau_{\rm p} \approx 0$ case. It is therefore plausible for $R_{\max}(T/2)$ to drop near or slightly below the blockade radius seen at $\tau_{\rm p} \approx 0$.

Figures 6.7(a-d) demonstrate that the values for $R_{\max}$ are smaller for larger values of S both for $\Delta = 0$ and $2\pi \times 4$ MHz. The relationship between $R_{\max}$ and S is shown in Figure 6.7(e). The value of S increases from near zero to ~ 0.8 as the radius of maximal correlation diminishes from ~ 13 μm to ~ 8 μm. The $S(R_{\max})$ dependencies extracted from the $\Delta = 0$ and $2\pi \times 4$ MHz measurements agree well within their overlap region, 9 μm $< R_{\max} <$ 10 μm. The rotary-echo sequence therefore provides an ability to control the most probable separation between atom pairs. It is noted that the value of S changes substantially over the range of accessible separation distances. Figure 6.7(f) shows that S is qualitatively proportional to the van der Waals interaction strength C_6/R^6 at $R_{\max}$. While this may seem reasonable, an explanation

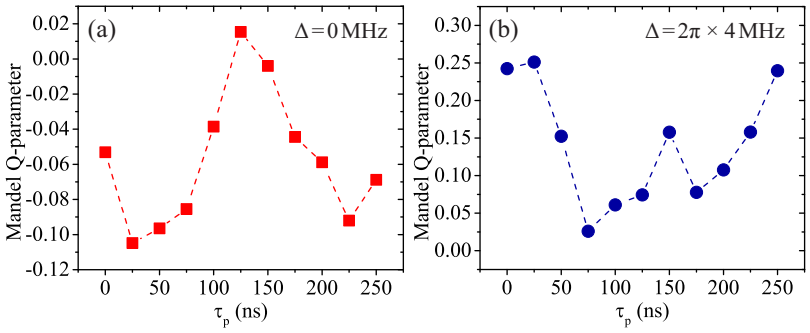

Figure 6.8: Q-parameter as a function of $\tau_{\rm p}$ for (a) $\Delta = 0$ MHz and (b) $\Delta = 2\pi \times 4$ MHz.

of this behavior will require more investigation.

6.6 Mandel Q-parameters

In addition to a profound effect of the echo excitation sequence on spatial correlations in cold Rydberg-atom samples, a related effect is expected in the Rydberg excitation counting statistics, which should also carry signatures of the correlations in the system. A measure to characterize counting statistics is the Mandel Q-parameter [18, 20–22] given by,

$$Q = \frac{\langle N(\tau_{\rm p})^2 \rangle - \langle N(\tau_{\rm p}) \rangle^2}{\langle N(\tau_{\rm p}) \rangle} - 1 \quad . \tag{6.3}$$

Figure 6.8 shows the Q-parameters versus $\tau_{\rm p}$. The plotted values do not take the detection efficiency η into account; the actual Q-parameters in the sample are given by Q/η. The Q-parameters observed for $\Delta = 0$ MHz [Figure 6.8(a)] are mostly negative, ranging from -0.10 to 0.02, while the ones for $\Delta = 2\pi \times 4$ MHz [Figure 6.8(b)] are positive, ranging from 0.03 to 0.25. This shows that for $\Delta = 0$ and $\tau_{\rm p} \sim 0$ and $\sim T$ the atoms largely follow sub-Poissonian statistics ($Q < 0$), while for $\Delta = 2\pi \times 4$ MHz and $\tau_{\rm p} \sim 0$ and T they follow super-Poissonian statistics ($Q > 0$).

The trends observed in the Q-parameter measurements can be explained as follows. For the case of on-resonant excitation without echo, the atom counting statistics are sub-Poissonian (Q<0) due to a blockade effect [18], as demonstrated in Figure 6.8(a)

at τ_{p} near 0 and 250 ns. In contrast, the Q-parameters for systems containing mostly pair-excitations are expected to trend toward positive values [36, 39], indicating super-Poissonian distributions. This effect is demonstrated in Figure 6.8, in which the Q-parameters reach high values when pair excitations are dominant. This is the case for $\tau_{\mathrm{p}} = 125$ ns at $\Delta = 0$ MHz [Figure 6.8(a)], and $\tau_{\mathrm{p}} = 0$ and 250 ns at $\Delta = 2\pi \times 4$ MHz [Figure 6.8(b)]. These cases correspond to the images with bold borders in Figure 6.6(a).

For a qualitative explanation of why ensembles of correlated Rydberg-atom pairs lead to super-Poissonian statistics, I consider a Poissonian distribution of atom pairs ($Q_{\mathrm{pair}} = 0$). Since every pair contains two atoms, I substitute $N = 2N_{\mathrm{pair}}$ into Equation (6.3). The relation between Q_{pair} and the Q-parameter for single-atom detections, Q_{single}, is seen to be

$$Q = Q_{\mathrm{single}} = 2Q_{\mathrm{pair}} + 1 \quad . \tag{6.4}$$

Hence, a Poissonian distribution of uncorrelated Rydberg-atom pairs ($Q_{\mathrm{pair}} = 0$) results in a super-Poissonian distribution of single-atom detections ($Q_{\mathrm{single}} = 1$). Considering that the detection efficiency is $\eta \sim 0.3$, I expect a measured $Q \sim 0.3$, which is close to the value shown in Figure 6.8(b) at $\tau_{\mathrm{p}} = 0$ and T.

6.7 Simulation

To understand the rotary echo effect, I solve a 2-body time-dependent Schrödinger equation using the same parameters used in the experiment. The Hamiltonian for the

echo sequence in the field-interaction picture is

$$H = \frac{\hbar}{2} \begin{array}{c} \begin{matrix} |gg\rangle & |gr\rangle & |rg\rangle & |rr\rangle \end{matrix} \\ \begin{pmatrix} 0 & \Omega(t) & \Omega(t) & 0 \\ \Omega(t) & -2\Delta_1 & 0 & \Omega(t) \\ \Omega(t) & 0 & -2\Delta_2 & \Omega(t) \\ 0 & \Omega(t) & \Omega(t) & -2(\Delta_1+\Delta_2)+2\Delta_{\mathrm{vdW}} \end{pmatrix} \end{array} . \tag{6.5}$$

where $\Omega(t)$ is the Rabi frequency for single-atom excitation, defined as

$$\Omega = \begin{cases} \Omega_0 & 0 \leqslant t < \tau_{\mathrm{p}} \quad , \\ -\Omega_0 & \tau_{\mathrm{p}} \leqslant t \leqslant T \quad , \end{cases} \tag{6.6}$$

$\Delta_{\mathrm{i}} = \Delta + \Delta_{\mathrm{Doppler,i}}$ is the detuning of an atom i, which consists of the excitation laser detuning Δ and an additional shift due to the Doppler effect $\Delta_{\mathrm{Doppler}}$ ($\approx$ 300 kHz). The van der Waals interaction is denoted Δ_{vdW}.

Starting with the ground state $|gg\rangle$, the final state after excitation is $\Psi = c_{\mathrm{gg}}|gg\rangle + c_{\mathrm{rg}}|rg\rangle + c_{\mathrm{gr}}|gr\rangle + c_{\mathrm{rr}}|rr\rangle$. The number of excitations is calculated from $|c_{\mathrm{rg}}|^2 + |c_{\mathrm{gr}}|^2 + 2|c_{\mathrm{rr}}|^2$ with a maximum excitation number of 2 for the pair excitation. The factor of two in front of $|c_{\mathrm{rr}}|^2$ is due to the fact that two Rydberg atoms are observed from the pair excitation.

6.7.1 Echo dynamics

In order to understand the population dynamics of atoms under the echo effect, I calculate the number of excitations by applying $\Omega_0 = 2\pi \times 1.67$ MHz, $T = 250$ ns, and neglect $\Delta_{\mathrm{Doppler}}$. The number of excitations at three selected values of Δ when $\Delta_{\mathrm{vdW}} = 2\pi \times 4$ MHz is shown in Figure 6.9. For the on-resonant case ($\Delta = 0$) shown

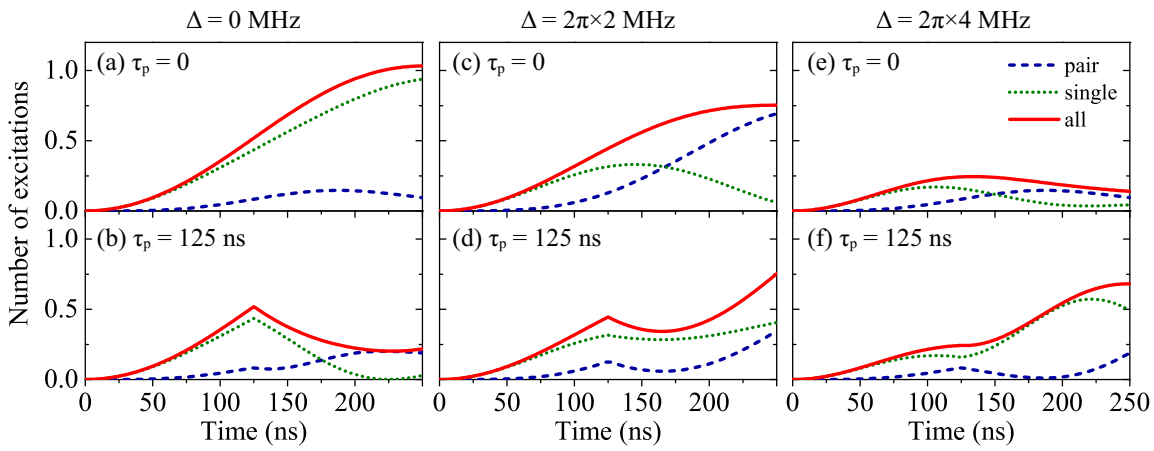

Figure 6.9: Number of excitations when $V_{\mathrm{vdW}} = 2\pi \times 4$ MHz for (a,b) $\Delta = 0$, (c,d) $\Delta = 2$ MHz, and (e,f) $\Delta = 4$ MHz obtained from pair (blue dashed lines), single (green dotted lines), and all (red solid lines) refer to $2|c_{\mathrm{rr}}|^2$, $|c_{\mathrm{rg}}|^2 + |c_{\mathrm{gr}}|^2$, and $|c_{\mathrm{rg}}|^2 + |c_{\mathrm{gr}}|^2 + 2|c_{\mathrm{rr}}|^2$, respectively.

in Figure 6.9(a), the excitation pulse approaches a π-pulse when there is no phase inversion, so the single-atom excitations almost reach the maximum value with only a small contribution from pair excitations. At the end of the pulse with phase inversion [Figure 6.9(b)], the contribution of the single-atom excitations become almost zero while the pair excitations become the main contribution to the total number of excitations. This calculation supports the pair correlation enhancement that is experimentally observed in Figure 6.6(a, top row) at 125 ns and the explanation in Figure 6.2(c).

For off-resonant excitation, the population of the $|rr\rangle$ state comes from pair excitations [$\Delta_1 = \Delta_2 = \Delta_{\mathrm{vdw}}/2 = 2$ MHz, see Figures 6.9(c,d)] or facilitated excitations [$\Delta_1 = \Delta_2 = \Delta_{\mathrm{vdw}} = 4$ MHz, see Figures 6.9(e,f)]. Without phase inversion [Figures 6.9(c,e)], the main contribution of the total excitations comes from pair excitation. However, with phase inversion as seen in Figures 6.9(d,f), the pair-excitation undergoes population inversion and the contribution of the single excitations is comparable to or larger than the contribution of the pair excitations. This leads to the pair correlation enhancement reduction, as observed in Figure 6.6(a, bottom row) at

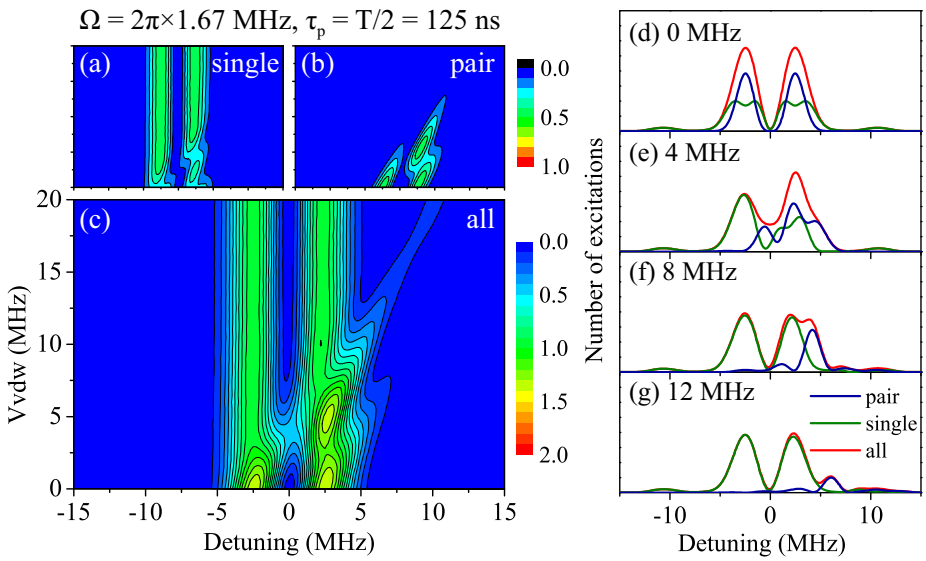

Figure 6.10: Number of Rydberg excitations as a function of Van der Waals interaction (C_6/R^6) and laser detuning when $\Omega = 2\pi \times 1.67$ MHz and $\tau_p = 125$ ns obtained from (a) single excitations $|c_{rg}|^2 + |c_{gr}|^2$ (b) pair excitations $|c_{rr}|^2$ and (c) all (single and pair) excitations $|c_{rg}|^2 + |c_{gr}|^2 + 2|c_{rr}|^2$. (d-g) Number of atoms versus laser detuning for various van der Waals interactions.

125 ns. This calculation also supports the interpretation presented in Figure 6.2(c).

6.7.2 Echo spectra

In Figure 6.4(b) at $\tau_p = 125$ ns, the experimentally obtained spectrum is not symmetric and the depression at the middle of the spectrum is not zero. To investigate the asymmetry of the spectral shape, I perform a calculation using the excitation pulse shape in Figure 6.4(a) at $\tau_p = 125$ ns. I take a square root to turn units of intensity to units of electric field. Then, the curve is normalized such that the plateau takes an average value of 1. This curve is then multiplied with the experimental Rabi frequency. Note that the excitation laser pulse deviates from the perfect shape with a distinct intensity notch at the time of the phase inversion. I assign a phase of 0° to the first part of the pulse (before the notch minimum) and of 180° to the second part of the pulse (after the notch minimum).

The resulting number of Rydberg excitations when $\tau_p = 125$ ns as a function of van der Waals interaction and laser detuning is shown in Figure 6.10. It can be

seen that single excitations [Figure 6.10(a)] have excitation peaks at ± 2.5 MHz while pair excitations [Figure 6.10(b)] have asymmetry excitations trending toward positive detuning. Inspection of Figures 6.10(a-c) reveals that the shoulder on the right in Figure 6.4(b) at $\tau_{\mathrm{p}} = 125$ ns, the asymmetry of the two main peaks, as well as the signal at zero detuning are in large part due to the atom-pair contribution (direct two-photon excitations). The plots of the number of excitations in Figures 6.10(d-g) show that the peak position of the pair excitations moves to the right (positive detuning) when the van der Waals interaction increases.

To calculate the excitation spectrum, I apply a weighted average over the nearest-neighbor distribution in a randomly distributed ground state atom sample. The distribution $P(r)$ in an ideal gas is given by

$$P(r) = \frac{3r^2}{a^3} \exp\left[-\left(\frac{r}{a}\right)^3\right] \tag{6.7}$$

where a is a Wigner-Seitz radius. By using $f = C_6/r^6$ and $P(r)dr = \tilde{P}(f)df$, the distribution in the frequency domain becomes

$$\tilde{P}(f) = \frac{C_6^{1/2}}{2a^3 f^{3/2}} \exp\left[-\frac{1}{a^3}\left(\frac{C_6}{f}\right)^{1/2}\right] \tag{6.8}$$

The resulting spectrum when the density of ground-state atom is about 10^{10} cm^{-3} is shown in Figure 6.11. Note that in this model the interactions between more than two atoms are neglected. The spectrum is influenced by the Fourier transform of the excitation pulse. The sideband at -10 MHz observed in the experimental spectrum coincides with the first negative side lobe of the Fourier transform of the excitation pulse.

There may be phase-drift (frequency chirp) effects in the vicinity of τ_{p} that cannot be measured. Such imperfections may come from the RF transmission line, the RF reception characteristics in the AOM electric circuit, and the transmission of the RF

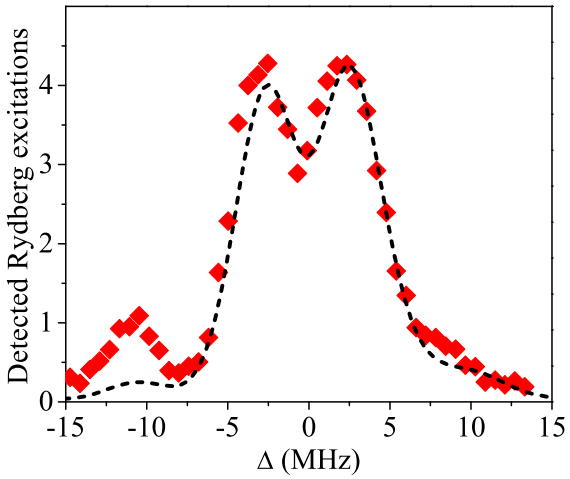

Figure 6.11: Experimental Rydberg excitation spectra for $\tau_p = 0125$ ns (red diamonds) and simulated spectrum for $\tau_p = 125$ ns (black dashed line). The simulation is scaled to match the experiment.

acoustic wave through the AOM crystal. These effects may explain why the simulated signal due to the Fourier sideband at -10 MHz in Figure 6.11 is not as strong as the experimentally observed signal. A full phase-sensitive characterization of the excitation electric-field pulse would require a time-dependent, interferometric analysis of the optical pulse.

6.8 Summary

In summary I have measured the effect of the rotary echo on spatial pair correlation functions and counting statistics of Rydberg atoms for on- and off-resonant excitations. The measurements show the connection between spatial correlations and counting statistics. The result also shows that it is possible to prepare correlated Rydberg atoms at a well-defined interatomic separation by using this method. This ability could be useful in atom kinetics experiments [25, 106]. To make the method attractive for such applications, it is desirable to find conditions in which the pair correlation enhancement obtained with the echo method exceeds that obtained with plain off-resonant excitation (see Figure 6.7). This may be achievable, in the future, by reducing the excitation bandwidth and possibly by elaborate shaping of the ampli-

tude and phase functions of the excitation pulse. Further, it would be interesting to explore the effect of the echo sequence in the case of anisotropic interaction potentials.

CHAPTER VII

Conclusion and Future Work

This chapter includes a summary of accomplishments and discoveries from the experiments. I have discussed in the preceding chapters that long-range interactions can be studied using the apparatus and the techniques available to this work. A possible future experiment that could be performed is to observe novel types of long-range molecular states in Rydberg atom systems. Preliminary results and calculations presented in this chapter show that this apparatus is well suited for Rydberg molecule experiments.

7.1 Conclusion

I have achieved submicron-resolution spatial images of Rydberg atom positions using a high-magnification ion imaging apparatus. I have demonstrated an ability to prepare Rydberg atoms with a well-defined interatomic separation in the imaging setup. In addition, I have extracted the C_3 and C_6 interaction coefficients through atom-pair kinetics. The experimental values agree well with calculated results, thereby validating the theoretical models presented in Chapter II. Further, I have used a rotary-echo technique to control pair correlation enhancements between Rydberg atoms. I have observed that the rotary echo can give rise to or destroy spatial correlations by tuning the excitation laser frequency.

The pair correlation functions demonstrate the first direct visualization of an isotropic repulsive van der Waals interaction and an anisotropic dipole-dipole interaction. The measurements also imply that the kinetic interaction occurs between individual atoms, not superatoms. This means that the many-body entanglement present in the initially prepared state becomes destroyed due to the action of interatomic forces. The observation of repulsive Rydberg-atom dynamics amounts to the experimental discovery of dissociating van der Waals Rydberg molecules. The agreement between experimental and theoretical C_3 and C_6 lends credibility to the developed method of computing Rydberg-Rydberg adiabatic potentials. This is a valuable discovery because the computational work is not trivial. For instance, the two-body product Hilbert space needs to be truncated in suitable ways to allow for a numerical treatment. The work further presents an initial step towards future kinematic studies of bound Rydberg-Rydberg molecules. It is expected that future work expanding on this thesis will directly reveal vibrational wave-packet dynamics.

7.2 Rydberg molecules

The long-range Rydberg molecules provide new tools to study ultracold chemistry. The molecules can be formed between a Rydberg atom and a ground-state atom (e.g., trilobites molecules [107, 108] and butterfly molecules [109, 110]), two Rydberg atoms [111–113], or polyatom [114]. Important requirements to observe molecular states include high enough ground-state atom density, narrow laser linewidth, appropriate photoassociation sequence, and good electric field control.

With the sub-micron resolution imaging in the TIP experiment, pair correlation enhancements that result from the atoms in the same molecule or between neighboring molecules can be observed. However, the atom density nearby the TIP is low due to

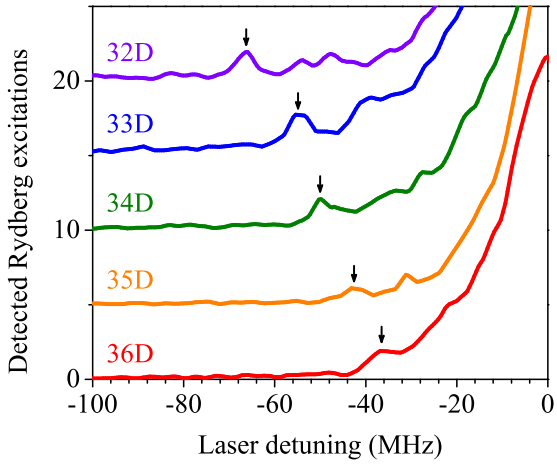

Figure 7.1: Experimentally obtained spectra centered on $nD_{5/2}$ Rydberg line. The arrows indicate the $(nD + 5S_{1/2})$ molecular lines.

the scattering of the MOT light out the TIP. To increase the density of the atom sample, I apply an an optical dipole trap (ODT) produced from a 1064-nm laser with a power of about 4 W. The ODT has the same timing sequence as the MOT light and it is off during Rydberg-atom excitation and electric field ionization.

7.2.1 Rydberg-ground molecule

A Rydberg-ground molecule is created from interactions between a Rydberg electron and a ground state atom [115] through several interaction channels (e.g., S- or P-wave scattering and finestructure coupling). In the recent work, I study the formation of D-type Rydberg molecules, which have been observed in a magnetic trap with a peak density $\sim 10^{11}$ cm^{-3} [116]. Preliminary observations of Rydberg-ground molecules in the TIP experiment is shown in Figure 7.1. I observe ^{85}Rb$(nD + 5S_{1/2})$ Rydberg molecules, as indicated by black arrows. The positions of the molecular lines agree well with Reference [116]. Because the nD Rydbeg molecules are formed in dense atom samples ($\sim 10^{11}$ cm^{-3}), the observation of molecular lines indicate that the low density limitation due to the light scattering from the TIP is overcome. Since the required atomic density is achieved, it is possible to perform a Rydberg-ground

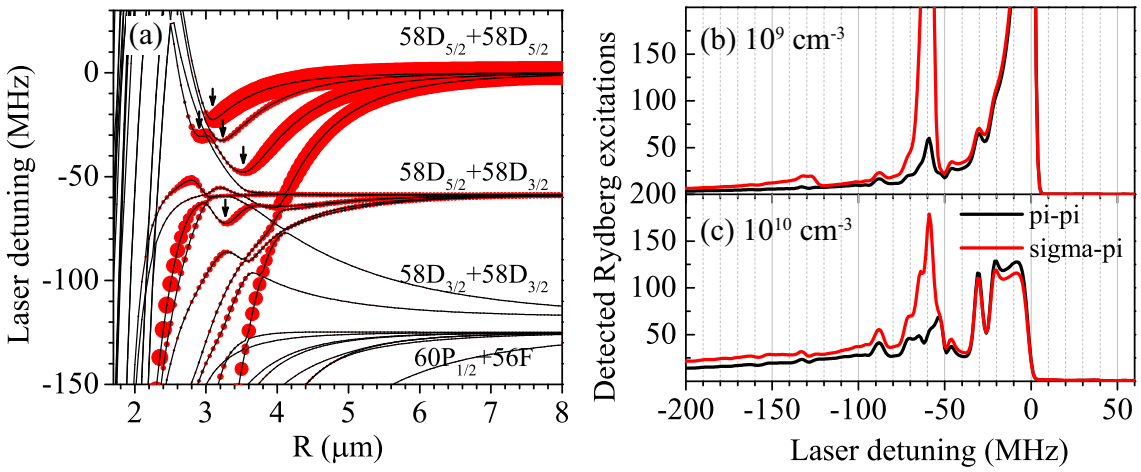

Figure 7.2: (a) Calculated energy levels including dipole-dipole, dipole-quadrupole and quadrupole-quadrupole interactions in the vicinity of $58D_{5/2}58D_{5/2}$ pair state. The area of the red circles is proportional to the excitation strength. The arrows indicate location of bound states. (b) Calculated spectra averaged over ground-state atom density of 10^9 cm^{-3}. (c) Same as (b) for 10^{10} cm^{-3}.

imaging experiment in the TIP setup.

7.2.2 Rydberg-Rydberg molecule

Rydberg-Rydberg molecules result from a binding potential that arises from an avoided crossing between two or more states that are close in energy. With an interatomic separation larger than 1 μm, they are also referred to as macrodimers.

In the Raithel lab, the availability of lasers allows for two configurations of Rydberg excitation. The first configuration uses 780- and 480-nm laser to perform a two-photon excitation. Atoms follow the $(5S_{1/2}, F = 3 \rightarrow 5P_{3/2}, F' = 4 \rightarrow nS$ or $nD)$ transition. The second configuration uses 780-, 776-, and 1260-nm lasers to perform a 3-photon excitation. Atoms follow the $(5S_{1/2}, F = 3 \rightarrow 5P_{3/2}, F' = 4 \rightarrow 5D_{5/2} \rightarrow nP$ or $nF)$ transition. These two configurations allow Rydberg-Rydberg molecule experiment to be performed with S, P, D or F states.

Recently, I have been trying to observe the $nD + nD$ macrodimers in the TIP experiment. Calculations following Section 2.2.2 have been performed to find pair states that have strong excitation strength and promising binding energies. Figure 7.2

shows the results of a calculation of Rydberg-Rydberg interactions in the vicinity of the $58D_{5/2} + 58D_{5/2}$ pair state. In Figure 7.2(a), the binding potentials are red detuned from the $58D_{5/2} + 58D_{5/2}$ asymptote. The expected Rydberg spectrum is calculated from averaging over the nearest-neighbor distribution in a randomly distributed ground state atom sample at different densities shown in Figure 7.2(b,c). It can be seen that the spectral shape strongly depends on the density of ground state atoms. It is experimentally challenging to observe the macrodimers because the broadening of $58D_{5/2} + 58D_{5/2}$ asymptote to the negative detuning obstructs the appearance of expected molecular lines. It is important to have a narrow laser linewidth and an ability to control the atom density, which could reduce the broadening of the $58D_{5/2} + 58D_{5/2}$ line and help to observe the molecular line. One might also consider applying a short pulse to make seed atoms before application of a long excitation pulse to form molecules, as explained in Reference [113].

APPENDIX

APPENDIX A

Uncertainty calculation

A.1 Magnification

Peak positions and local parabolic fit uncertainties obtained from the experiment in Chapter IV are shown in Table A.1. The total relative uncertainty of magnification are shown in Table A.2.

Table A.1: Values obtained from local parabolic fits of the interference peaks.

peak position (pixel)	uncertainty (pixel)	peak spacing (pixel)	uncertainty of peak spacing (pixel)
95.66	0.28		
155.06	0.21	(155.06-95.66)=59.40	$\sqrt{(0.28)^2 + (0.21)^2} = 0.35$
217.01	0.11	(217.01-155.06)=61.95	$\sqrt{(0.21)^2 + (0.11)^2} = 0.24$
Weighted average peak spacing		61.16	0.20

Table A.2: Statistical uncertainty for magnification calibration.

Statistical relative uncertainty	$(0.2/61.16) = 0.003$
Field distortion relative uncertainty	$(61.95 - 59.40)/(2 \times 61.16) = 0.02$
Total relative uncertainty	$\sqrt{(0.003)^2 + (0.02)^2} = 0.02$

A.2 R_0 calculation

R_0 is obtained from weighted averaging of interatomic separations at the two earliest wait times.

Table A.3: Interatomic separation at the two earliest wait times.

wait time (μs)	separation, R_i (μm)	uncertainty, σ_i (μm)
0.25	8.83	0.09
2.5	8.78	0.02
Weighted average	8.78	0.02

The weighted average is obtained from [117]

$$\bar{x} = \frac{\sum (x_i/\sigma_i^2)}{\sum (1/\sigma_i^2)} \implies R_0 = \frac{(\frac{R_1}{\sigma_1^2} + \frac{R_2}{\sigma_2^2})}{(\frac{1}{\sigma_1^2} + \frac{1}{\sigma_2^2})} = 8.78 \ \mu\text{m} \quad . \tag{A.1}$$

The weighted uncertainty is obtained from

$$\sigma = \sqrt{\frac{1}{\sum (1/\sigma_i^2)}} \implies \sigma_0 = \sqrt{\frac{1}{(\frac{1}{\sigma_1^2} + \frac{1}{\sigma_2^2})}} = 0.02 \ \mu\text{m} \quad . \tag{A.2}$$

A.3 C_6 calculation

C_6 is obtained from Equation (4.3) in Section 4.3,

$$C_6 = \frac{1}{2}\mu V_t^2 R_0^6 \quad . \tag{A.3}$$

Using $R_0 = 8.78 \pm 0.02$ μm (obtained from the local parabolic fit of the $I(R)$ curves) and $V_t = 0.182 \pm 0.008$ m/s (obtained from the linear fit of the most probable separations) leads to $C_6 = (5.4 \pm 0.5) \times 10^{-58}$ Jm^6, where the error propagation is given by

$$\begin{aligned} \sigma_{C_6} &= \sqrt{\sigma_{V_t}^2 (\frac{\partial C_6}{\partial V_t})^2 + \sigma_{R_0}^2 (\frac{\partial C_6}{\partial R_0})^2} \\ &= \sqrt{\sigma_{V_t}^2 (2\frac{C_6}{V_t})^2 + \sigma_{R_0}^2 (6\frac{C_6}{R_0})^2} \\ \frac{\sigma_{C_6}}{C_6} &= \sqrt{(2\frac{\sigma_{V_t}}{V_t})^2 + (6\frac{\sigma_{R_0}}{R_0})^2} \\ &= 0.09 \text{ (relative uncertainty)} \end{aligned} \tag{A.4}$$

A.4 Additional uncertainty from magnification

The values R_0 and V_t used in Section A.3 are obtained by multiplying the measured values ($R_{0,i}$ and $V_{t,i}$; in units of pixel and pixel/s, respectively) with the magnification calibration factor (M). Equation (A.3) can be written as

$$\begin{aligned} C_6 &= \frac{1}{2}\mu(V_{t,i} \times M)^2(R_{0,i} \times M)^6 \\ &= \frac{1}{2}\mu(V_{t,i})^2(R_{0,i})^6(M)^8 \end{aligned} \tag{A.5}$$

The relative uncertainty of C_6 including the magnification uncertainty becomes

$$\begin{aligned} \frac{\sigma_{C_6'}}{C_6'} &= \sqrt{(2\frac{\sigma_{V_{t,i}}}{V_{t,i}})^2 + (6\frac{\sigma_{R_{0,i}}}{R_{0,i}})^2 + (8\frac{\sigma_M}{M})^2} \\ &= \sqrt{(\frac{\sigma_{C_6}}{C_6})^2 + (8\frac{\sigma_M}{M})^2} \\ &= \sqrt{(0.09)^2 + (8 \times 0.02)^2} \text{ (Equation (A.4) and Table A.2)} \\ &= 0.18 \text{ (relative uncertainty)} \end{aligned} \tag{A.6}$$

The final relative uncertainty of C_6 follows from three statistically independent contributions: the fit uncertainty for V_t, the fit uncertainty for R_0, and the magnification uncertainty. The respective powers at which these quantities enter into C_6 are 2, 6, and 8. This leads to $C_6 = (5.4 \pm 1.0) \times 10^{-58}$ Jm^6, as presented in Chapter IV.

BIBLIOGRAPHY

BIBLIOGRAPHY

[1] C.S.E. van Ditzhuijzen, A.F. Koenderink, J.V. Hernández, F. Robicheaux, L.D. Noordam, and H.B. van den Heuvell. Spatially Resolved Observation of Dipole-Dipole Interaction between Rydberg Atoms. *Phys. Rev. Lett.*, 100(24):243201, June 2008. doi: 10.1103/PhysRevLett.100.243201. URL http://link.aps.org/doi/10.1103/PhysRevLett.100.243201.

[2] Emily Altiere, Donald P. Fahey, Michael W. Noel, Rachel J. Smith, and Thomas J. Carroll. Dipole-dipole interaction between rubidium Rydberg atoms. *Phys. Rev. A*, 84(5):053431, November 2011. doi: 10.1103/PhysRevA.84.053431. URL http://link.aps.org/doi/10.1103/PhysRevA.84.053431.

[3] Sylvain Ravets, Henning Labuhn, Daniel Barredo, Lucas Béguin, Thierry Lahaye, and Antoine Browaeys. Coherent dipole-dipole coupling between two single Rydberg atoms at an electrically-tuned Forster resonance. *Nat. Phys.*, 10(12):914–917, December 2014. ISSN 1745-2473. doi: 10.1038/nphys3119. URL http://www.nature.com.proxy.lib.umich.edu/nphys/journal/v10/n12/abs/nphys3119.html.

[4] Sylvain Ravets, Henning Labuhn, Daniel Barredo, Thierry Lahaye, and Antoine Browaeys. Measurement of the angular dependence of the dipole-dipole interaction between two individual Rydberg atoms at a Förster resonance. *Phys. Rev. A*, 92(2):020701, August 2015. doi: 10.1103/PhysRevA.92.020701. URL http://link.aps.org/doi/10.1103/PhysRevA.92.020701.

[5] A. Reinhard, K. C. Younge, T. Cubel Liebisch, B. Knuffman, P. R. Berman, and G. Raithel. Double-Resonance Spectroscopy of Interacting Rydberg-Atom Systems. *Phys. Rev. Lett.*, 100(23):233201, June 2008. doi: 10.1103/PhysRevLett.100.233201. URL http://link.aps.org/doi/10.1103/PhysRevLett.100.233201.

[6] L. Béguin, A. Vernier, R. Chicireanu, T. Lahaye, and A. Browaeys. Direct Measurement of the van der Waals Interaction between Two Rydberg Atoms. *Phys. Rev. Lett.*, 110(26):263201, June 2013. doi: 10.1103/PhysRevLett.110.263201. URL http://link.aps.org/doi/10.1103/PhysRevLett.110.263201.

[7] M. D. Lukin, M. Fleischhauer, R. Cote, L. M. Duan, D. Jaksch, J. I. Cirac, and P. Zoller. Dipole Blockade and Quantum Information Processing in Mesoscopic Atomic Ensembles. *Phys. Rev. Lett.*, 87(3):037901, June 2001. doi: 10.1103/PhysRevLett.87.037901. URL http://link.aps.org/doi/10.1103/PhysRevLett.87.037901.

[8] D. Tong, S. M. Farooqi, J. Stanojevic, S. Krishnan, Y. P. Zhang, R. Côté, E. E. Eyler, and P. L. Gould. Local Blockade of Rydberg Excitation in an Ultracold Gas. *Phys. Rev. Lett.*, 93(6):063001, August 2004. doi: 10.1103/PhysRevLett.93.063001. URL http://link.aps.org/doi/10.1103/PhysRevLett.93.063001.

[9] E. Urban, T. A. Johnson, T. Henage, L. Isenhower, D. D. Yavuz, T. G. Walker, and M. Saffman. Observation of Rydberg blockade between two atoms. *Nat. Phys.*, 5(2):110–114, February 2009. ISSN 1745-2473. doi: 10.1038/nphys1178. URL http://www.nature.com.proxy.lib.umich.edu/nphys/journal/v5/n2/full/nphys1178.html.

[10] T. M. Weber, M. Höning, T. Niederprüm, T. Manthey, O. Thomas, V. Guarrera, M. Fleischhauer, G. Barontini, and H. Ott. Mesoscopic Rydberg-blockaded ensembles in the superatom regime and beyond. *Nat. Phys.*, 11(2):157–161, February 2015. ISSN 1745-2473. doi: 10.1038/nphys3214. URL http://www.nature.com.proxy.lib.umich.edu/nphys/journal/v11/n2/full/nphys3214.html.

[11] X. Zhang, F. B. Dunning, S. Yoshida, and J. Burgdörfer. Rydberg blockade effects at $n \sim 300$ in strontium. *Phys. Rev. A*, 92(5):051402, November 2015. doi: 10.1103/PhysRevA.92.051402. URL http://link.aps.org/doi/10.1103/PhysRevA.92.051402.

[12] Rolf Heidemann, Ulrich Raitzsch, Vera Bendkowsky, Björn Butscher, Robert Löw, Luis Santos, and Tilman Pfau. Evidence for Coherent Collective Rydberg Excitation in the Strong Blockade Regime. *Phys. Rev. Lett.*, 99(16):163601, October 2007. doi: 10.1103/PhysRevLett.99.163601. URL http://link.aps.org/doi/10.1103/PhysRevLett.99.163601.

[13] Martin Gärttner, Shannon Whitlock, David W. Schönleber, and Jörg Evers. Collective Excitation of Rydberg-Atom Ensembles beyond the Superatom Model. *Phys. Rev. Lett.*, 113(23):233002, December 2014. doi: 10.1103/PhysRevLett.113.233002. URL http://link.aps.org/doi/10.1103/PhysRevLett.113.233002.

[14] F. Robicheaux and J. V. Hernández. Many-body wave function in a dipole blockade configuration. *Phys. Rev. A*, 72(6):063403, December 2005. doi: 10.1103/PhysRevA.72.063403. URL http://link.aps.org/doi/10.1103/PhysRevA.72.063403.

[15] A. Schwarzkopf, R. E. Sapiro, and G. Raithel. Imaging Spatial Correlations of Rydberg Excitations in Cold Atom Clouds. *Phys. Rev. Lett.*, 107(10):103001, August 2011. doi: 10.1103/PhysRevLett.107.103001. URL http://link.aps.org/doi/10.1103/PhysRevLett.107.103001.

[16] Peter Schauß, Marc Cheneau, Manuel Endres, Takeshi Fukuhara, Sebastian Hild, Ahmed Omran, Thomas Pohl, Christian Gross, Stefan Kuhr, and Immanuel Bloch. Observation of spatially ordered structures in a two-dimensional Rydberg gas. *Nature*, 491(7422):87–91, November 2012. ISSN 0028-0836. doi: 10.1038/nature11596. URL http://www.nature.com.proxy.lib.umich.edu/nature/journal/v491/n7422/full/nature11596.html.

[17] Henning Labuhn, Daniel Barredo, Sylvain Ravets, Sylvain de Léséleuc, Tommaso Macrì, Thierry Lahaye, and Antoine Browaeys. Tunable two-dimensional arrays of single Rydberg atoms for realizing quantum Ising models. *Nature*, 534(7609):667–670, June 2016. ISSN 0028-0836. doi: 10.1038/nature18274. URL http://www.nature.com/nature/journal/v534/n7609/full/nature18274.html.

[18] T. Cubel Liebisch, A. Reinhard, P. R. Berman, and G. Raithel. Atom Counting Statistics in Ensembles of Interacting Rydberg Atoms. *Phys. Rev. Lett.*, 95(25):253002, December 2005. doi: 10.1103/PhysRevLett.95.253002. URL http://link.aps.org/doi/10.1103/PhysRevLett.95.253002.

[19] T. Cubel Liebisch, A. Reinhard, P. R. Berman, and G. Raithel. Erratum: Atom Counting Statistics in Ensembles of Interacting Rydberg Atoms [Phys. Rev. Lett. 95, 253002 (2005)]. *Phys. Rev. Lett.*, 98(10):109903, March 2007. doi: 10.1103/PhysRevLett.98.109903. URL http://link.aps.org/doi/10.1103/PhysRevLett.98.109903.

[20] C. Ates, T. Pohl, T. Pattard, and J. M. Rost. Strong interaction effects on the atom counting statistics of ultracold Rydberg gases. *J. Phys. B: At. Mol. Opt. Phys.*, 39(11):L233, 2006. ISSN 0953-4075. doi: 10.1088/0953-4075/39/11/L02. URL http://stacks.iop.org/0953-4075/39/i=11/a=L02.

[21] N. Malossi, M. M. Valado, S. Scotto, P. Huillery, P. Pillet, D. Ciampini, E. Arimondo, and O. Morsch. Full Counting Statistics and Phase Diagram of a Dissipative Rydberg Gas. *Phys.*

Rev. Lett., 113(2):023006, July 2014. doi: 10.1103/PhysRevLett.113.023006. URL http://link.aps.org/doi/10.1103/PhysRevLett.113.023006.

[22] H. Schempp, G. Günter, M. Robert-de Saint-Vincent, C. S. Hofmann, D. Breyel, A. Komnik, D. W. Schönleber, M. Gärttner, J. Evers, S. Whitlock, and M. Weidemüller. Full Counting Statistics of Laser Excited Rydberg Aggregates in a One-Dimensional Geometry. *Phys. Rev. Lett.*, 112(1):013002, January 2014. doi: 10.1103/PhysRevLett.112.013002. URL http://link.aps.org/doi/10.1103/PhysRevLett.112.013002.

[23] Jaron Sanders, Matthieu Jonckheere, and Servaas Kokkelmans. Sub-Poissonian Statistics of Jamming Limits in Ultracold Rydberg Gases. *Phys. Rev. Lett.*, 115(4):043002, July 2015. doi: 10.1103/PhysRevLett.115.043002. URL http://link.aps.org/doi/10.1103/PhysRevLett.115.043002.

[24] A. Schwarzkopf, D. A. Anderson, N. Thaicharoen, and G. Raithel. Spatial correlations between Rydberg atoms in an optical dipole trap. *Phys. Rev. A*, 88(6):061406, December 2013. doi: 10.1103/PhysRevA.88.061406. URL http://link.aps.org/doi/10.1103/PhysRevA.88.061406.

[25] N. Thaicharoen, A. Schwarzkopf, and G. Raithel. Measurement of the van der Waals interaction by atom trajectory imaging. *Phys. Rev. A*, 92(4):040701, October 2015. doi: 10.1103/PhysRevA.92.040701. URL http://link.aps.org/doi/10.1103/PhysRevA.92.040701.

[26] Thomas Amthor, Christian Giese, Christoph S. Hofmann, and Matthias Weidemüller. Evidence of Antiblockade in an Ultracold Rydberg Gas. *Phys. Rev. Lett.*, 104(1):013001, January 2010. doi: 10.1103/PhysRevLett.104.013001. URL http://link.aps.org/doi/10.1103/PhysRevLett.104.013001.

[27] Martin Gärttner, Kilian P. Heeg, Thomas Gasenzer, and Jörg Evers. Dynamic formation of Rydberg aggregates at off-resonant excitation. *Phys. Rev. A*, 88(4):043410, October 2013. doi: 10.1103/PhysRevA.88.043410. URL http://link.aps.org/doi/10.1103/PhysRevA.88.043410.

[28] Igor Lesanovsky and Juan P. Garrahan. Out-of-equilibrium structures in strongly interacting Rydberg gases with dissipation. *Phys. Rev. A*, 90(1):011603, July 2014. doi: 10.1103/PhysRevA.90.011603. URL http://link.aps.org/doi/10.1103/PhysRevA.90.011603.

[29] A. Urvoy, F. Ripka, I. Lesanovsky, D. Booth, J. P. Shaffer, T. Pfau, and R. Löw. Strongly Correlated Growth of Rydberg Aggregates in a Vapor Cell. *Phys. Rev. Lett.*, 114(20):203002, May 2015. doi: 10.1103/PhysRevLett.114.203002. URL http://link.aps.org/doi/10.1103/PhysRevLett.114.203002.

[30] M. M. Valado, C. Simonelli, M. D. Hoogerland, I. Lesanovsky, J. P. Garrahan, E. Arimondo, D. Ciampini, and O. Morsch. Experimental observation of controllable kinetic constraints in a cold atomic gas. *Phys. Rev. A*, 93(4):040701, April 2016. doi: 10.1103/PhysRevA.93.040701. URL http://link.aps.org/doi/10.1103/PhysRevA.93.040701.

[31] Matthieu Viteau, Paul Huillery, Mark G. Bason, Nicola Malossi, Donatella Ciampini, Oliver Morsch, Ennio Arimondo, Daniel Comparat, and Pierre Pillet. Cooperative Excitation and Many-Body Interactions in a Cold Rydberg Gas. *Phys. Rev. Lett.*, 109(5):053002, July 2012. doi: 10.1103/PhysRevLett.109.053002. URL http://link.aps.org/doi/10.1103/PhysRevLett.109.053002.

[32] N. Thaicharoen, A. Schwarzkopf, and G. Raithel. Control of Spatial Correlations between Rydberg Excitations using Rotary Echo. *Phys. Rev. Lett.*, 118(13):133401, March 2017. doi: 10.1103/PhysRevLett.118.133401. URL https://link.aps.org/doi/10.1103/PhysRevLett.118.133401.

[33] J. V. Hernández and F. Robicheaux. Simulations using echo sequences to observe coherence in a cold Rydberg gas. *J. Phys. B: At. Mol. Opt. Phys.*, 41(19):195301, October 2008. ISSN 0953-4075. doi: 10.1088/0953-4075/41/19/195301. URL http://iopscience.iop.org/0953-4075/41/19/195301.

[34] Ulrich Raitzsch, Vera Bendkowsky, Rolf Heidemann, Björn Butscher, Robert Löw, and Tilman Pfau. Echo Experiments in a Strongly Interacting Rydberg Gas. *Phys. Rev. Lett.*, 100(1): 013002, January 2008. doi: 10.1103/PhysRevLett.100.013002. URL http://link.aps.org/doi/10.1103/PhysRevLett.100.013002.

[35] Kelly Cooper Younge and Georg Raithel. Rotary echo tests of coherence in Rydberg-atom excitation. *New J. Phys.*, 11(4):043006, April 2009. ISSN 1367-2630. doi: 10.1088/1367-2630/11/4/043006. URL http://iopscience.iop.org/1367-2630/11/4/043006.

[36] S. Wüster, J. Stanojevic, C. Ates, T. Pohl, P. Deuar, J. F. Corney, and J. M. Rost. Correlations of Rydberg excitations in an ultracold gas after an echo sequence. *Phys. Rev. A*, 81(2):023406, February 2010. doi: 10.1103/PhysRevA.81.023406. URL http://link.aps.org/doi/10.1103/PhysRevA.81.023406.

[37] Hendrik Weimer, Robert Löw, Tilman Pfau, and Hans Peter Büchler. Quantum Critical Behavior in Strongly Interacting Rydberg Gases. *Phys. Rev. Lett.*, 101(25):250601, December 2008. doi: 10.1103/PhysRevLett.101.250601. URL http://link.aps.org/doi/10.1103/PhysRevLett.101.250601.

[38] C. Ates, T. Pohl, T. Pattard, and J. M. Rost. Many-body theory of excitation dynamics in an ultracold Rydberg gas. *Phys. Rev. A*, 76(1):013413, July 2007. doi: 10.1103/PhysRevA.76.013413. URL http://link.aps.org/doi/10.1103/PhysRevA.76.013413.

[39] Kilian P. Heeg, Martin Gärttner, and Jörg Evers. Hybrid model for Rydberg gases including exact two-body correlations. *Phys. Rev. A*, 86(6):063421, December 2012. doi: 10.1103/PhysRevA.86.063421. URL http://link.aps.org/doi/10.1103/PhysRevA.86.063421.

[40] Martin Gärttner, Kilian P. Heeg, Thomas Gasenzer, and Jörg Evers. Finite-size effects in strongly interacting Rydberg gases. *Phys. Rev. A*, 86(3):033422, September 2012. doi: 10.1103/PhysRevA.86.033422. URL http://link.aps.org/doi/10.1103/PhysRevA.86.033422.

[41] T. Pohl, E. Demler, and M. D. Lukin. Dynamical Crystallization in the Dipole Blockade of Ultracold Atoms. *Phys. Rev. Lett.*, 104(4):043002, January 2010. doi: 10.1103/PhysRevLett.104.043002. URL http://link.aps.org/doi/10.1103/PhysRevLett.104.043002.

[42] R. M. W. van Bijnen, S. Smit, K. A. H. van Leeuwen, E. J. D. Vredenbregt, and S. J. J. M. F. Kokkelmans. Adiabatic formation of Rydberg crystals with chirped laser pulses. *J. Phys. B: At. Mol. Opt. Phys.*, 44(18):184008, 2011. ISSN 0953-4075. doi: 10.1088/0953-4075/44/18/184008. URL http://stacks.iop.org/0953-4075/44/i=18/a=184008.

[43] P. Schauß, J. Zeiher, T. Fukuhara, S. Hild, M. Cheneau, T. Macrì, T. Pohl, I. Bloch, and C. Gross. Crystallization in Ising quantum magnets. *Science*, 347(6229):1455–1458, March 2015. ISSN 0036-8075, 1095-9203. doi: 10.1126/science.1258351. URL http://www.sciencemag.org/content/347/6229/1455.

[44] David Petrosyan, Klaus Mølmer, and Michael Fleischhauer. On the adiabatic preparation of spatially-ordered Rydberg excitations of atoms in a one-dimensional optical lattice by laser frequency sweeps. *J. Phys. B: At. Mol. Opt. Phys.*, 49(8):084003, 2016. ISSN 0953-4075. doi: 10.1088/0953-4075/49/8/084003. URL http://stacks.iop.org/0953-4075/49/i=8/a=084003.

[45] C. Ates and I. Lesanovsky. Entropic enhancement of spatial correlations in a laser-driven Rydberg gas. *Phys. Rev. A*, 86(1):013408, July 2012. doi: 10.1103/PhysRevA.86.013408. URL http://link.aps.org/doi/10.1103/PhysRevA.86.013408.

[46] T. Wilk, A. Gaëtan, C. Evellin, J. Wolters, Y. Miroshnychenko, P. Grangier, and A. Browaeys. Entanglement of Two Individual Neutral Atoms Using Rydberg Blockade. *Phys. Rev. Lett.*, 104(1):010502, January 2010. doi: 10.1103/PhysRevLett.104.010502. URL http://link.aps.org/doi/10.1103/PhysRevLett.104.010502.

[47] L. Isenhower, E. Urban, X. L. Zhang, A. T. Gill, T. Henage, T. A. Johnson, T. G. Walker, and M. Saffman. Demonstration of a Neutral Atom Controlled-NOT Quantum Gate. *Phys. Rev. Lett.*, 104(1):010503, January 2010. doi: 10.1103/PhysRevLett.104.010503. URL http://link.aps.org/doi/10.1103/PhysRevLett.104.010503.

[48] Tyler Keating, Krittika Goyal, Yuan-Yu Jau, Grant W. Biedermann, Andrew J. Landahl, and Ivan H. Deutsch. Adiabatic quantum computation with Rydberg-dressed atoms. *Phys. Rev. A*, 87(5):052314, May 2013. doi: 10.1103/PhysRevA.87.052314. URL http://link.aps.org/doi/10.1103/PhysRevA.87.052314.

[49] David Petrosyan and Klaus Mølmer. Binding Potentials and Interaction Gates between Microwave-Dressed Rydberg Atoms. *Phys. Rev. Lett.*, 113(12):123003, September 2014. doi: 10.1103/PhysRevLett.113.123003. URL http://link.aps.org/doi/10.1103/PhysRevLett.113.123003.

[50] Lin Li and A. Kuzmich. Quantum memory with strong and controllable Rydberg-level interactions. *Nature Communications*, 7:13618, November 2016. ISSN 2041-1723. doi: 10.1038/ncomms13618. URL http://www.nature.com/ncomms/2016/161121/ncomms13618/full/ncomms13618.html.

[51] Y. O. Dudin and A. Kuzmich. Strongly Interacting Rydberg Excitations of a Cold Atomic Gas. *Science*, 336(6083):887–889, May 2012. ISSN 0036-8075, 1095-9203. doi: 10.1126/science.1217901. URL http://www.sciencemag.org/content/336/6083/887.

[52] J. Kitching, S. Knappe, and E. A. Donley. Atomic Sensors #x2013; A Review. *IEEE Sensors Journal*, 11(9):1749–1758, September 2011. ISSN 1530-437X. doi: 10.1109/JSEN.2011.2157679.

[53] Jonathon A. Sedlacek, Arne Schwettmann, Harald Kübler, Robert Löw, Tilman Pfau, and James P. Shaffer. Microwave electrometry with Rydberg atoms in a vapour cell using bright atomic resonances. *Nat. Phys.*, 8(11):819–824, November 2012. ISSN 1745-2473. doi: 10.1038/nphys2423. URL http://www.nature.com.proxy.lib.umich.edu/nphys/journal/v8/n11/full/nphys2423.html?WT.ec_id=NPHYS-201211.

[54] C.L. Holloway, J.A. Gordon, S. Jefferts, A. Schwarzkopf, D.A. Anderson, S.A. Miller, N. Thaicharoen, and G. Raithel. Broadband Rydberg Atom-Based Electric-Field Probe for SI-Traceable, Self-Calibrated Measurements. *IEEE Transactions on Antennas and Propagation*, 62(12):6169–6182, December 2014. ISSN 0018-926X. doi: 10.1109/TAP.2014.2360208.

[55] Haoquan Fan, Santosh Kumar, Jonathon Sedlacek, Harald Kübler, Shaya Karimkashi, and James P. Shaffer. Atom based RF electric field sensing. *J. Phys. B: At. Mol. Opt. Phys.*, 48(20):202001, 2015. ISSN 0953-4075. doi: 10.1088/0953-4075/48/20/202001. URL http://stacks.iop.org/0953-4075/48/i=20/a=202001.

[56] A. M. Hankin, Y.-Y. Jau, L. P. Parazzoli, C. W. Chou, D. J. Armstrong, A. J. Landahl, and G. W. Biedermann. Two-atom Rydberg blockade using direct $6S$ to nP excitation. *Phys. Rev. A*, 89(3):033416, March 2014. doi: 10.1103/PhysRevA.89.033416. URL https://link.aps.org/doi/10.1103/PhysRevA.89.033416.

[57] Y.-Y. Jau, A. M. Hankin, T. Keating, I. H. Deutsch, and G. W. Biedermann. Entangling atomic spins with a Rydberg-dressed spin-flip blockade. *Nat. Phys.*, 12(1):71–74, January 2016. ISSN 1745-2473. doi: 10.1038/nphys3487. URL http://www.nature.com/nphys/journal/v12/n1/full/nphys3487.html?message-global=remove.

[58] S. E. Anderson, K. C. Younge, and G. Raithel. Trapping Rydberg Atoms in an Optical Lattice. *Phys. Rev. Lett.*, 107(26):263001, December 2011. doi: 10.1103/PhysRevLett.107.263001. URL https://link.aps.org/doi/10.1103/PhysRevLett.107.263001.

[59] M. Viteau, M. G. Bason, J. Radogostowicz, N. Malossi, D. Ciampini, O. Morsch, and E. Arimondo. Rydberg Excitations in Bose-Einstein Condensates in Quasi-One-Dimensional Potentials and Optical Lattices. *Phys. Rev. Lett.*, 107(6):060402, August 2011. doi: 10.1103/PhysRevLett.107.060402. URL https://link.aps.org/doi/10.1103/PhysRevLett.107.060402.

[60] T. Macrì and T. Pohl. Rydberg dressing of atoms in optical lattices. *Phys. Rev. A*, 89(1):011402, January 2014. doi: 10.1103/PhysRevA.89.011402. URL https://link.aps.org/doi/10.1103/PhysRevA.89.011402.

[61] Tatjana Gericke, Peter Würtz, Daniel Reitz, Tim Langen, and Herwig Ott. High-resolution scanning electron microscopy of an ultracold quantum gas. *Nat. Phys.*, 4(12):949–953, December 2008. ISSN 1745-2473. doi: 10.1038/nphys1102. URL http://www.nature.com/nphys/journal/v4/n12/full/nphys1102.html.

[62] T. Manthey, T. M. Weber, T. Niederprüm, P. Langer, V. Guarrera, G. Barontini, and H. Ott. Scanning electron microscopy of Rydberg-excited Bose–Einstein condensates. *New J. Phys.*, 16(8):083034, 2014. ISSN 1367-2630. doi: 10.1088/1367-2630/16/8/083034. URL http://stacks.iop.org/1367-2630/16/i=8/a=083034.

[63] A. S. Stodolna, A. Rouzée, F. Lépine, S. Cohen, F. Robicheaux, A. Gijsbertsen, J. H. Jungmann, C. Bordas, and M. J. J. Vrakking. Hydrogen Atoms under Magnification: Direct Observation of the Nodal Structure of Stark States. *Phys. Rev. Lett.*, 110(21):213001, May 2013. doi: 10.1103/PhysRevLett.110.213001. URL http://link.aps.org/doi/10.1103/PhysRevLett.110.213001.

[64] Erwin W. Müller and Kanwar Bahadur. Field Ionization of Gases at a Metal Surface and the Resolution of the Field Ion Microscope. *Phys. Rev.*, 102(3):624–631, May 1956. doi: 10.1103/PhysRev.102.624. URL http://link.aps.org/doi/10.1103/PhysRev.102.624.

[65] Erwin W. Müller. Field Ion Microscopy. *Science*, 149(3684):591–601, August 1965. ISSN 0036-8075, 1095-9203. doi: 10.1126/science.149.3684.591. URL http://www.sciencemag.org.proxy.lib.umich.edu/content/149/3684/591.

[66] J. Ullrich, R. Moshammer, A. Dorn, R. Dörner, L. Ph H. Schmidt, and H. Schmidt-Böcking. Recoil-ion and electron momentum spectroscopy: reaction-microscopes. *Rep. Prog. Phys.*, 66(9):1463, August 2003. ISSN 0034-4885. doi: 10.1088/0034-4885/66/9/203. URL http://iopscience.iop.org/article/10.1088/0034-4885/66/9/203/meta.

[67] S. Möbius, M. Genkin, S. Wüster, A. Eisfeld, and J. M. Rost. Breakup of Rydberg-blockaded atom clouds via dipole-dipole interactions. *Phys. Rev. A*, 88(1):012716, July 2013. doi: 10.1103/PhysRevA.88.012716. URL http://link.aps.org/doi/10.1103/PhysRevA.88.012716.

[68] Johannes Zeiher, Peter Schauß, Sebastian Hild, Tommaso Macrì, Immanuel Bloch, and Christian Gross. Microscopic Characterization of Scalable Coherent Rydberg Superatoms. *Phys. Rev. X*, 5(3):031015, August 2015. doi: 10.1103/PhysRevX.5.031015. URL http://link.aps.org/doi/10.1103/PhysRevX.5.031015.

[69] Christopher L. Holloway, Joshua A. Gordon, Andrew Schwarzkopf, David A. Anderson, Stephanie A. Miller, Nithiwadee Thaicharoen, and Georg Raithel. Sub-wavelength imaging and field mapping via electromagnetically induced transparency and Autler-Townes splitting in Rydberg atoms. *Applied Physics Letters*, 104(24):244102, June 2014. ISSN 0003-6951, 1077-3118. doi: 10.1063/1.4883635. URL http://scitation.aip.org.proxy.lib.umich.edu/content/aip/journal/apl/104/24/10.1063/1.4883635.

[70] Joshua A. Gordon, Christopher L. Holloway, Andrew Schwarzkopf, Dave A. Anderson, Stephanie Miller, Nithiwadee Thaicharoen, and Georg Raithel. Millimeter wave detection via Autler-Townes splitting in rubidium Rydberg atomsa). *Applied Physics Letters*, 105(2):024104, July 2014. ISSN 0003-6951, 1077-3118. doi: 10.1063/1.4890094. URL http://scitation.aip.org.proxy.lib.umich.edu/content/aip/journal/apl/105/2/10.1063/1.4890094.

[71] D. A. Anderson, A. Schwarzkopf, S. A. Miller, N. Thaicharoen, G. Raithel, J. A. Gordon, and C. L. Holloway. Two-photon microwave transitions and strong-field effects in a room-temperature Rydberg-atom gas. *Phys. Rev. A*, 90(4):043419, October 2014. doi: 10.1103/PhysRevA.90.043419. URL http://link.aps.org/doi/10.1103/PhysRevA.90.043419.

[72] C. L. Holloway, J. A. Gordon, M. T. Simons, H. Fan, S. Kumar, J. P. Shaffer, D. A. Anderson, A. Schwarzkopf, S. A. Miller, N. Thaicharoen, and G. Raithel. Atom-based RF electric field measurements: An initial investigation of the measurement uncertainties. In *2015 IEEE International Symposium on Electromagnetic Compatibility (EMC)*, pages 467–472, August 2015. doi: 10.1109/ISEMC.2015.7256207.

[73] Richard R. Freeman and Daniel Kleppner. Core polarization and quantum defects in high-angular-momentum states of alkali atoms. *Phys. Rev. A*, 14(5):1614–1619, November 1976. doi: 10.1103/PhysRevA.14.1614. URL http://link.aps.org/doi/10.1103/PhysRevA.14.1614.

[74] F. T. Arecchi, R. Bonifacio, and M. O. Scully. *Coherence in Spectroscopy and Modern Physics*, volume 37 of *NATO Advanced Study Institutes Series*. 1978. ISBN 978-1-4613-2871-1. URL http://www.springer.com/us/book/9780306400506.

[75] Thomas F. Gallagher. *Rydberg Atoms*. Cambridge Monographs on Atomic, Molecular and Chemical Physics. Cambridge University Press, November 2005. ISBN 978-0-521-02166-1. URL http://www.cambridge.org/us/academic/subjects/physics/atomic-physics-molecular-physics-and-chemical-physics/rydberg-atoms.

[76] Robert Löw, Hendrik Weimer, Johannes Nipper, Jonathan B. Balewski, Björn Butscher, Hans Peter Büchler, and Tilman Pfau. An experimental and theoretical guide to strongly interacting Rydberg gases. *J. Phys. B: At. Mol. Opt. Phys.*, 45(11):113001, 2012. ISSN 0953-4075. doi: 10.1088/0953-4075/45/11/113001. URL http://stacks.iop.org/0953-4075/45/i=11/a=113001.

[77] Peter Schauss. *High-resolution imaging of ordering in Rydberg many-body systems*. PhD thesis, Ludwig-Maximilians-Universität München, February 2015. URL https://edoc.ub.uni-muenchen.de/18152/.

[78] F. Gounand. Calculation of radial matrix elements and radiative lifetimes for highly excited states of alkali atoms using the Coulomb approximation. *J. Phys. France*, 40(5):457–460, May 1979. ISSN 0302-0738. doi: 10.1051/jphys:01979004005045700. URL http://dx.doi.org/10.1051/jphys:01979004005045700.

[79] John W. Farley and William H. Wing. Accurate calculation of dynamic Stark shifts and depopulation rates of Rydberg energy levels induced by blackbody radiation. Hydrogen, helium, and alkali-metal atoms. *Phys. Rev. A*, 23(5):2397–2424, May 1981. doi: 10.1103/PhysRevA.23.2397. URL http://link.aps.org/doi/10.1103/PhysRevA.23.2397.

[80] I. I. Beterov, I. I. Ryabtsev, D. B. Tretyakov, and V. M. Entin. Quasiclassical calculations of blackbody-radiation-induced depopulation rates and effective lifetimes of Rydberg nS, nP, and nD alkali-metal atoms with $n \leqslant 80$. *Phys. Rev. A*, 79(5):052504, May 2009. doi: 10.1103/PhysRevA.79.052504. URL http://link.aps.org/doi/10.1103/PhysRevA.79.052504.

[81] Moody L. Coffman. Correction to the Rydberg Constant for Finite Nuclear Mass. *American Journal of Physics*, 33(10):820–823, October 1965. ISSN 0002-9505. doi: 10.1119/1.1970992. URL http://aapt.scitation.org/doi/10.1119/1.1970992.

[82] Peter J. Mohr, David B. Newell, and Barry N. Taylor. CODATA recommended values of the fundamental physical constants: 2014. *Rev. Mod. Phys.*, 88(3):035009, September 2016. doi: 10.1103/RevModPhys.88.035009. URL http://link.aps.org/doi/10.1103/RevModPhys.88.035009.

[83] Gordon W. F. Drake. *Springer Handbook of Atomic, Molecular, and Optical Physics*. 2006. ISBN 978-0-387-26308-3. URL http://www.springer.com/us/book/9780387208022.

[84] Wenhui Li, I. Mourachko, M. W. Noel, and T. F. Gallagher. Millimeter-wave spectroscopy of cold Rb Rydberg atoms in a magneto-optical trap: Quantum defects of the ns, np, and nd series. *Phys. Rev. A*, 67(5):052502, May 2003. doi: 10.1103/PhysRevA.67.052502. URL http://link.aps.org/doi/10.1103/PhysRevA.67.052502.

[85] Markus Mack, Florian Karlewski, Helge Hattermann, Simone Höckh, Florian Jessen, Daniel Cano, and József Fortágh. Measurement of absolute transition frequencies of ^{87}Rb to ns and nd Rydberg states by means of electromagnetically induced transparency. *Phys. Rev. A*, 83(5):052515, May 2011. doi: 10.1103/PhysRevA.83.052515. URL http://link.aps.org/doi/10.1103/PhysRevA.83.052515.

[86] Jianing Han, Yasir Jamil, D. V. L. Norum, Paul J. Tanner, and T. F. Gallagher. Rb nf quantum defects from millimeter-wave spectroscopy of cold ^{85}Rb Rydberg atoms. *Phys. Rev. A*, 74(5):054502, November 2006. doi: 10.1103/PhysRevA.74.054502. URL http://link.aps.org/doi/10.1103/PhysRevA.74.054502.

[87] Myron L. Zimmerman, Michael G. Littman, Michael M. Kash, and Daniel Kleppner. Stark structure of the Rydberg states of alkali-metal atoms. *Phys. Rev. A*, 20(6):2251–2275, December 1979. doi: 10.1103/PhysRevA.20.2251. URL http://link.aps.org/doi/10.1103/PhysRevA.20.2251.

[88] Robert J. Le Roy. Long-Range Potential Coefficients From RKR Turning Points: C_6 and C_8 for $B(^3\Pi_{ou}+)$-State Cl_2, Br_2, and I_2. *Can. J. Phys.*, 52(3):246–256, February 1974. ISSN 0008-4204. doi: 10.1139/p74-035. URL http://www.nrcresearchpress.com/doi/abs/10.1139/p74-035.

[89] John David Jackson. *Classical electrodynamics*. Wiley, 3rd edition, 1999. ISBN 978-0-471-30932-1. URL http://cdsweb.cern.ch/record/490457.

[90] A. Reinhard, T. Cubel Liebisch, B. Knuffman, and G. Raithel. Level shifts of rubidium Rydberg states due to binary interactions. *Phys. Rev. A*, 75(3):032712, March 2007. doi: 10.1103/PhysRevA.75.032712. URL http://link.aps.org/doi/10.1103/PhysRevA.75.032712.

[91] M. R. Flannery, D. Vrinceanu, and V. N. Ostrovsky. Long-range interaction between polar Rydberg atoms. *J. Phys. B: At. Mol. Opt. Phys.*, 38(2):S279, 2005. ISSN 0953-4075. doi: 10.1088/0953-4075/38/2/020. URL http://stacks.iop.org/0953-4075/38/i=2/a=020.

[92] Kilian Singer, Jovica Stanojevic, Matthias Weidemüller, and Robin Côté. Long-range interactions between alkali Rydberg atom pairs correlated to the ns–ns, np–np and nd–nd asymptotes. *J. Phys. B: At. Mol. Opt. Phys.*, 38(2):S295, 2005. ISSN 0953-4075. doi: 10.1088/0953-4075/38/2/021. URL http://stacks.iop.org/0953-4075/38/i=2/a=021.

[93] Johannes Deiglmayr, Heiner Saßmannshausen, Pierre Pillet, and Frédéric Merkt. Observation of Dipole-Quadrupole Interaction in an Ultracold Gas of Rydberg Atoms. *Phys. Rev. Lett.*, 113(19):193001, November 2014. doi: 10.1103/PhysRevLett.113.193001. URL http://link.aps.org/doi/10.1103/PhysRevLett.113.193001.

[94] Thomas J. Carroll, Shubha Sunder, and Michael W. Noel. Many-body interactions in a sample of ultracold Rydberg atoms with varying dimensions and densities. *Phys. Rev. A*, 73(3):032725, March 2006. doi: 10.1103/PhysRevA.73.032725. URL http://link.aps.org/doi/10.1103/PhysRevA.73.032725.

[95] Thibault Vogt, Matthieu Viteau, Amodsen Chotia, Jianming Zhao, Daniel Comparat, and Pierre Pillet. Electric-Field Induced Dipole Blockade with Rydberg Atoms. *Phys. Rev. Lett.*, 99(7):073002, August 2007. doi: 10.1103/PhysRevLett.99.073002. URL http://link.aps.org/doi/10.1103/PhysRevLett.99.073002.

[96] J. D. Pritchard, D. Maxwell, A. Gauguet, K. J. Weatherill, M. P. A. Jones, and C. S. Adams. Cooperative Atom-Light Interaction in a Blockaded Rydberg Ensemble. *Phys. Rev. Lett.*, 105(19):193603, November 2010. doi: 10.1103/PhysRevLett.105.193603. URL http://link.aps.org/doi/10.1103/PhysRevLett.105.193603.

[97] E. L. Raab, M. Prentiss, Alex Cable, Steven Chu, and D. E. Pritchard. Trapping of Neutral Sodium Atoms with Radiation Pressure. *Phys. Rev. Lett.*, 59(23):2631–2634, December 1987. doi: 10.1103/PhysRevLett.59.2631. URL http://link.aps.org/doi/10.1103/PhysRevLett.59.2631.

[98] Harold J. Metcalf and Peter van der Straten. *Laser Cooling and Trapping*. Graduate Texts in Contemporary Physics. Springer New York, New York, NY, 1999. ISBN 978-0-387-98728-6 978-1-4612-1470-0. URL http://link.springer.com/10.1007/978-1-4612-1470-0.

[99] Andrew D. Schwarzkopf. *Imaging Spatial Correlations of Rydberg Excitations in Cold Atom Clouds.* PhD thesis, University of Michigan, 2013. URL http://deepblue.lib.umich.edu/handle/2027.42/99943.

[100] F. Robicheaux. Ionization due to the interaction between two Rydberg atoms. *J. Phys. B: At. Mol. Opt. Phys.*, 38(2):S333, January 2005. ISSN 0953-4075. doi: 10.1088/0953-4075/38/2/024. URL http://iopscience.iop.org.proxy.lib.umich.edu/0953-4075/38/2/024.

[101] Limei Wang, Hao Zhang, Linjie Zhang, Changyong Li, Yonggang Yang, Jianming Zhao, Georg Raithel, and Suotang Jia. Dipolar Rydberg-atom gas prepared by adiabatic passage through an avoided crossing. *New J. Phys.*, 17(6):063011, June 2015. ISSN 1367-2630. doi: 10.1088/1367-2630/17/6/063011. URL http://iopscience.iop.org/article/10.1088/1367-2630/17/6/063011/meta.

[102] M. Ebert, M. Kwon, T. G. Walker, and M. Saffman. Coherence and Rydberg Blockade of Atomic Ensemble Qubits. *Phys. Rev. Lett.*, 115(9):093601, August 2015. doi: 10.1103/PhysRevLett.115.093601. URL http://link.aps.org/doi/10.1103/PhysRevLett.115.093601.

[103] Jan R. Rubbmark, Michael M. Kash, Michael G. Littman, and Daniel Kleppner. Dynamical effects at avoided level crossings: A study of the Landau-Zener effect using Rydberg atoms. *Phys. Rev. A*, 23(6):3107–3117, June 1981. doi: 10.1103/PhysRevA.23.3107. URL http://link.aps.org/doi/10.1103/PhysRevA.23.3107.

[104] T. C. Killian, T. Pattard, T. Pohl, and J. M. Rost. Ultracold neutral plasmas. *Physics Reports*, 449(4–5):77–130, September 2007. ISSN 0370-1573. doi: 10.1016/j.physrep.2007.04.007. URL http://www.sciencedirect.com/science/article/pii/S0370157307001937.

[105] M. Lyon and S. L. Rolston. Ultracold neutral plasmas. *Rep. Prog. Phys.*, 80(1):017001, 2017. ISSN 0034-4885. doi: 10.1088/0034-4885/80/1/017001. URL http://stacks.iop.org/0034-4885/80/i=1/a=017001.

[106] N. Thaicharoen, L. F. Gonçalves, and G. Raithel. Atom-Pair Kinetics with Strong Electric-Dipole Interactions. *Phys. Rev. Lett.*, 116(21):213002, May 2016. doi: 10.1103/PhysRevLett.116.213002. URL http://link.aps.org/doi/10.1103/PhysRevLett.116.213002.

[107] Chris H. Greene, A. S. Dickinson, and H. R. Sadeghpour. Creation of Polar and Nonpolar Ultra-Long-Range Rydberg Molecules. *Phys. Rev. Lett.*, 85(12):2458–2461, September 2000. doi: 10.1103/PhysRevLett.85.2458. URL http://link.aps.org/doi/10.1103/PhysRevLett.85.2458.

[108] D. Booth, S. T. Rittenhouse, J. Yang, H. R. Sadeghpour, and J. P. Shaffer. Production of trilobite Rydberg molecule dimers with kilo-Debye permanent electric dipole moments. *Science*, 348(6230):99–102, April 2015. ISSN 0036-8075, 1095-9203. doi: 10.1126/science.1260722. URL http://science.sciencemag.org/content/348/6230/99.

[109] Edward L. Hamilton, Chris H. Greene, and H. R. Sadeghpour. Shape-resonance-induced long-range molecular Rydberg states. *J. Phys. B: At. Mol. Opt. Phys.*, 35(10):L199, 2002. ISSN 0953-4075. doi: 10.1088/0953-4075/35/10/102. URL http://stacks.iop.org/0953-4075/35/i=10/a=102.

[110] Thomas Niederprüm, Oliver Thomas, Tanita Eichert, Carsten Lippe, Jesús Pérez-Ríos, Chris H. Greene, and Herwig Ott. Observation of pendular butterfly Rydberg molecules. *Nature Communications*, 7:12820, October 2016. ISSN 2041-1723. doi: 10.1038/ncomms12820. URL http://www.nature.com/ncomms/2016/161005/ncomms12820/full/ncomms12820.html.

[111] Christophe Boisseau, Ionel Simbotin, and Robin Côté. Macrodimers: Ultralong Range Rydberg Molecules. *Phys. Rev. Lett.*, 88(13):133004, March 2002. doi: 10.1103/PhysRevLett.88.133004. URL http://link.aps.org/doi/10.1103/PhysRevLett.88.133004.

[112] Martin Kiffner, Hyunwook Park, Wenhui Li, and T. F. Gallagher. Dipole-dipole-coupled double-Rydberg molecules. *Phys. Rev. A*, 86(3):031401, September 2012. doi: 10.1103/PhysRevA.86.031401. URL http://link.aps.org/doi/10.1103/PhysRevA.86.031401.

[113] Heiner Saßmannshausen and Johannes Deiglmayr. Observation of Rydberg-Atom Macrodimers: Micrometer-Sized Diatomic Molecules. *Phys. Rev. Lett.*, 117(8):083401, August 2016. doi: 10.1103/PhysRevLett.117.083401. URL http://link.aps.org/doi/10.1103/PhysRevLett.117.083401.

[114] Christian Fey, Markus Kurz, and Peter Schmelcher. Stretching and bending dynamics in triatomic ultralong-range Rydberg molecules. *Phys. Rev. A*, 94(1):012516, July 2016. doi: 10.1103/PhysRevA.94.012516. URL http://link.aps.org/doi/10.1103/PhysRevA.94.012516.

[115] Vera Bendkowsky, Björn Butscher, Johannes Nipper, James P. Shaffer, Robert Löw, and Tilman Pfau. Observation of ultralong-range Rydberg molecules. *Nature*, 458(7241):1005–1008, April 2009. ISSN 0028-0836. doi: 10.1038/nature07945. URL http://www.nature.com/nature/journal/v458/n7241/full/nature07945.html.

[116] D. A. Anderson, S. A. Miller, and G. Raithel. Photoassociation of Long-Range nD Rydberg Molecules. *Phys. Rev. Lett.*, 112(16):163201, April 2014. doi: 10.1103/PhysRevLett.112.163201. URL http://link.aps.org/doi/10.1103/PhysRevLett.112.163201.

[117] Philip R. Bevington and D. Keith Robinson. *Data reduction and error analysis for the physical sciences*. McGraw-Hill, 2003. ISBN 978-0-07-247227-1. Google-Books-ID: 0poQAQAAIAAJ.